MODELING AND EXPERIMENTAL VALIDATION OF A LOOP HEAT PIPE FOR TERRESTRIAL THERMAL MANAGEMENT APPLICATIONS

by

Matthew C. Page

In fulfillment of the degree of Master of Science in Mechanical Engineering, College of Agriculture, Engineering and Science, University of KwaZulu-Natal

Supervisor:
Mr. Michael J. Brooks
Co-Supervisors:
Prof. Lance W. Roberts
Mr. Clinton Bemont

7 January 2013

DECLARATION 1 - PLAGIARISM

I, …….……., declare that

1. The research reported in this dissertation, except where otherwise indicated, is my original research.

2. This dissertation has not been submitted for any degree or examination at any other university.

3. This dissertation does not contain other persons' data, pictures, graphs or other information, unless specifically acknowledged as being sourced from other persons.

4. This dissertation does not contain other persons' writing, unless specifically acknowledged as being sourced from other researchers. Where other written sources have been quoted, then:

a. Their words have been re-written but the general information attributed to them has been referenced

b. Where their exact words have been used, then their writing has been placed in italics and inside quotation marks, and referenced.

5. This dissertation does not contain text, graphics or tables copied and pasted from the Internet, unless specifically acknowledged, and the source being detailed in the dissertation and in the References sections.

Signed: ……

As the candidate's Supervisor I agree/do not agree to the submission of this dissertation.

Signed: ……

Name: Mr. Michael J. Brooks

Date: 7 January 2013

As the candidate's Supervisor I agree/do not agree to the submission of this dissertation.

Signed: ……

Name: Prof. Lance W. Roberts

Date: 7 January 2013

As the candidate's Supervisor I agree/do not agree to the submission of this dissertation.

Signed: ……

Name: Mr. Clinton Bemont

Date: 7 January 2013

DECLARATION 2 - PUBLICATION

PAGE, M.C., BROOKS, M.J., BEMONT, C., ROBERTS, L.W., 2012, Progress on performance validation of a steady-state loop heat pipe model, paper presented at AIAA *10th Annual International Energy Conversion Engineering Conference,* Atlanta, Georgia, USA, 29 July – 1 August 2012

Signed: ……

ACKNOWLEDGEMENTS

I would like to thank my supervisor, Mr. Michael J. Brooks, for his continuing assistance throughout this research and his patience with me. His encouragement and guidance have been fundamental in the completion of this work.

I would also like to thank Prof. Lance W. Roberts for his conversation and advice over the years, and for stimulating my interest in fluid mechanics and thermodynamics, as well as giving me the opportunity to be on the teaching and examining side of academics.

Mr. Clinton Bemont was of great help during the metallurgical portion of the research. Without the furnace, microscopes and other equipment he entrusted me use of, this research would not have been possible. He was always encouraging of the work I was doing and his faith in me has not been forgotten.

Thanks also need to go to the workshop technicians who helped machined and assemble the loop heat pipe, Strini Govender and Yushan Reddy in particular.

Sven du Clou, one of my colleagues in SERG, whose practical knowledge and experience in constructing heat and mass transfer devices was invaluable, was of tremendous assistance during the development of the loop heat pipe. His willingness to share equipment and knowledge with me hastened and improved the loop heat pipe.

I would also like to thank Michael Pillay, of the UKZN School of Chemistry, for his time and assistance in supplying the ammonia.

This research was supported and funded by the National Research Foundation of South Africa and ESKOM TESP.

Finally, my most heartfelt thanks go to my friends and family who continuously supported and encouraged me and my work over these years.

ABSTRACT

The Loop Heat Pipe (LHP) is a passive, two-phase heat transfer device used, most commonly, for thermal management of aerospace and aeronautical electronic equipment. A unique feature is a porous wick which generates the necessary capillary action required to maintain circulation between the heat source and the heat exchanger. What differentiates LHP devices from traditional heat pipes, which also work through the use of a wick structure, is the constrained locality of the wick, placed solely in the evaporator, which leaves the remainder of the piping throughout the device as hollow. This provides the LHP with a number of advantages, such as the ability to transport heat over long distances, operate in adverse gravitational positions and to tolerate numerous bends in the transport lines. It is also self-priming due to the use of a compensation chamber which passively provides the wick with constant liquid access. These advantages make LHPs popular in aerospace and aeronautical applications, but there is growing interest in their deployment for terrestrial thermal management systems.

This research had two aims. Firstly, to create and validate a robust mathematical model of the steady-state operation of an LHP for terrestrial high heat flux electronics. Secondly, to construct an experimental LHP, including a sintered porous wick, which could be used to validate the model and demonstrate the aforementioned heat exchange and gravity resistant characteristics.

The porous wick was sintered with properties of 60% porosity, 6.77×10^{-13} m^2 permeability and an average pore radius of 1μm. Ammonia was the chosen working fluid and the LHP functioned as expected during horizontal testing, albeit at higher temperatures than anticipated. For safety reasons the experimental LHP could not be operated past 18 bar, which translated into a maximum saturated vapour temperature of 45°C. The heat load range extended to 60 W, 50 W and 110 W for horizontal, gravity-adverse and gravity-assisted operation respectively.

Because of certain simplifying assumptions in the model, the experimental results deviated somewhat from predicted values at low heat loads. Model accuracy improved as the heat load increased. The experimental LHP behaved as expected for 5° and 10° gravity-assisted and gravity-adverse conditions, as well as for transport line variation, in which performance was assessed while the total tubing length was increased from 2.5 m to 4 m.

Overall, the construction of the LHP, particularly of the porous wick, its operation and the modeling of the constant conductance mode of operation proved to be successful. The variable conductance mode of operation was not accurately modeled, nor was expected behaviour in the elevation testing encountered, although the reasons for these results are suggested.

TABLE OF CONTENTS

LIST OF TABLES

LIST OF FIGURES

LIST OF SYMBOLS

A = area (m^2)

C_p = specific heat (J/kgK)

d = diameter (m)

dx = spatial increment (m)

f = frictional coefficient

G = thermal conductance (W/K)

h = coefficient of heat transfer (W/m^2K)

h_{fg} = latent heat of evaporation (J/kg)

k = thermal conductivity (W/mK)

K = permeability (m^2)

L = length (m)

$\dot{m}$ = mass flow rate (kg/s)

M = mass (kg)

n = number of vapour grooves

P = pressure (Pa)

Q = heat (W)

r = radius (m)

r_{pore} = pore radius (m)

R = radius of curvature (m)

$R_{heat\ sink}$ = thermal resistance of heat exchanger (mK/W)

t = height of vapour grooves (m)

T = temperature (K)

(UA/L) = thermal conductance per unit length (W/mK)

v = velocity (m/s)

V = volume (m^3)

w = width of vapour groove (m)

X = vapour quality

Xtt = Lockhart-Martinelli parameter

Greek Symbols

α = void fraction

β = void fraction

δ = film thickness (m)

Δ = incremental change

ε = porosity

θ = contact angle (degrees)

μ = viscosity (Pa.s)

ν = specific volume (m^3/kg)

ρ = density (kg/m^3)

ζ = surface tension (N/m)

η = shear stress (N/m^2)

θ = angle of elevation (degrees)

Subscripts

add = additional

amb = ambient

c = cold

cap = capillary

cc = compensation chamber

cc-if = interface in compensation chamber

cc-wall = compensation chamber wall

ch = mass charge

cond = condenser

dry = dry wick

eff = effective

ev = evaporator

ev-if = interface in evaporator

ev-wall = evaporator wall

f = fluid

fr = frictional

h = hot

HL1 = first heat leak

HL2 = second heat leak

i = inner

in = CC inlet

insulation = transport line insulation

l = liquid

ll = liquid line

loop = outer loop

mt = momentum transfer

o = outer

s = source

sad = saddle

sat = saturated wick

suspend = suspended wick

uw = serial

v = vapour

vg = vapour grooves

vl = vapour lines

wall = transport line wall

wi = wick

wick = wick material

xy = parallel

Abbreviations

CC = Compensation chamber

CPL = Capillary pumped loop

EDX = Energy-dispersive X-ray

FLHP = Flexible loop heat pipe

FY-IC = Fengyun

GLAS = Geoscience laser altimetry system

IC = Infrared camera

ICESar = Ice, cloud, and land elevation satellite

IGBT = Insulated-gate bipolar transistor

LHP = Loop heat pipe

mLHP = Miniature loop heat pipe

NCG = Non-condensable gases

STS = Space transport system

SEM = Scanning electron microscope

STS = Space transport system

TacSat = Tactical Satellite

TMG = Thermal model generator

1. INTRODUCTION AND LITERATURE REVIEW

1.1. Introduction to research

Loop heat pipes (LHPs) are passive, two-phase heat transfer devices which use the capillary action of a sintered wick in contact with a working fluid and a heat source to passively transport heat through evaporation and condensation mechanisms. Like other two-phase devices, they offer significantly improved thermal performance and reduced overall thermal resistance when compared to single-phase conduction and convection processes. They have been used in aerospace and aeronautical applications to fulfill the thermal management requirements which could not be solved by the employment of conventional heat pipes. This is due to a number of benefits they offer in addition to being as efficient a heat transfer device as conventional heat pipes. These include the ability to transport heat many metres away and under adverse gravitational conditions and to operate through narrow piping in a complex layout. There is now growing interest in developing terrestrial thermal management systems which exploit the advantages of LHPs. In the interests of furthering the use of LHP devices for terrestrial applications, the research conducted here focused on developing a theoretical model which can be used to model a terrestrial LHP, and secondly, to construct an experimental LHP to allow validation of the theoretical model and test the advantages which employing an LHP might bring.

The theoretical model takes the form of a steady-state, one-dimensional mathematical model of a terrestrial-based LHP. This approach was chosen above CFD analysis and transient models because it was considered more robust and informative. In addition to simulating the empirical data, there was an additional aim in constructing the model. Most of the modeling performed on LHPs in other studies requires empirical data before they can accurately predict the behaviour of the LHP in question. This means that while their models are accurate and informative, they are of little use in designing an LHP. Since this research is aimed towards the design and development of an LHP, the model created here contains certain assumptions which allow it to predict the performance of an LHP using only a single piece of empirical data, namely the thermal conductance between the evaporator wall and outer surface of the wick. The mathematical model is explained in Chapter 2.

The construction of the experimental LHP was necessary to validate the model. Since this was, to the author's knowledge, the first LHP developed in South Africa, considerable effort went into its construction. A study was performed into the sintering and machining of the porous wick as well as experimentation into determining its properties. This is presented in Chapter 3. The remainder of the construction, from the evaporator which housed the wick to the heat

exchanger, is discussed in Chapter 4, as well as the testing parameters and methodology for horizontal and inclined orientations as well as for variable line length. The model validation, as well as the investigation into the capabilities of the experimental LHP for gravity-assisted, gravity-adverse and transport line variation, are discussed in Chapter 5.

1.2. Introduction to literature review

LHP research can be divided into a number of categories. The most common research is application based, focusing on the use of an LHP to transport heat in a given system, such as a satellite environment, terrestrial server or personal computers. These illustrate the versatility of LHPs, indicating to some degree how they are constructed and what materials are commonly used for each application. Other research focuses on experimenting with LHP layouts by developing unique constructions of the sintered wick or other sections which may increase the utility of the LHP for a particular application. These give an indication of possible innovations in LHP design.

There has also been some theoretical work over the last decade which describes the mathematical or numerical simulations created to account for LHP behaviour. Some of these are analytical models of the LHP as a whole, while others focus on a single core aspect of LHP modeling. The latter studies attempt to produce a better understanding of how the region under investigation functions. Earlier research is general and illustrates the operation of the LHP while also providing steady-state, one-dimensional mathematical modeling suggestions. Contemporary mathematical models focus on improving preceding steady-state models or developing transient models for startup analysis. These all give a strong idea of how to create a steady-state, mathematical model and also what behaviour the experimental LHP would display and how to simulate it. These also provide information on LHP construction which is generally difficult to obtain. In particular there is little published research detailing the manufacture of the sintered wicks, although a few works give background on sintering materials and methods. Finally, a number of review articles provide a useful guide to LHP research as well as assisting in comparing different LHP configurations.

1.3. LHP theory

An LHP is composed of a number of sections thermally and hydraulically connected together to form a closed loop. These include an evaporator connected, with a saddle, to a heat source which requires thermal regulation. Inside the evaporator is a porous sintered wick, machined with channels known as vapour grooves and an inner cavity. Connected to the vapour side of the evaporator is the vapour line, which is smooth, small diameter, hollow tubing of varying length depending on the parameters of the application. The vapour line leads on to the condenser, also

a smooth hollow tube of various potential lengths, which is cooled through a heat sink which can take a variety of forms. The outlet of the condenser leads on to the liquid line which, like the vapour line and condenser, is hollow tubing. The liquid line leads back to the evaporator body and attaches and extends into the compensation chamber (CC), a hydroaccumulator integrated with the evaporator which allows fluid access to the evaporator and wick, completing the enclosed loop. The bayonet extends from the CC through to an inner cavity machined into the porous wick. A schematic of the LHP is shown in Figure 1-1.

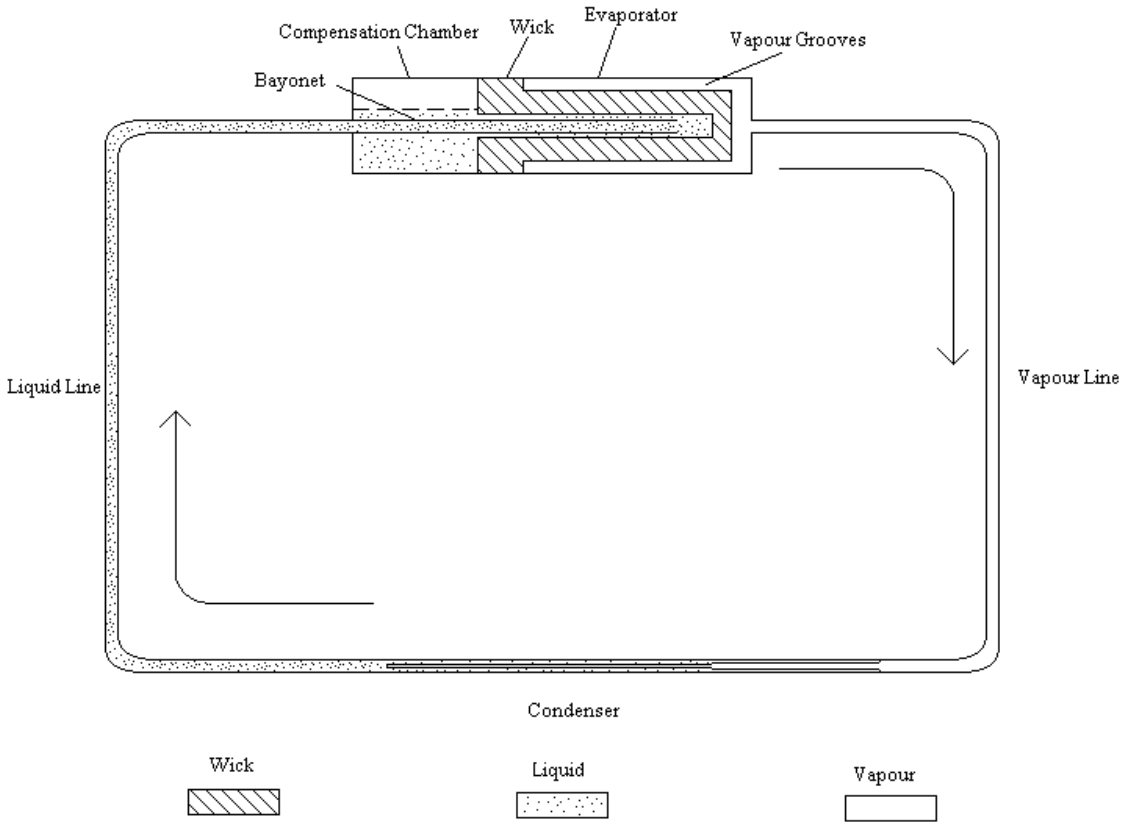

Fig.1-1. A schematic of an LHP

The basic operation of the LHP is well known and the authoritative text on the subject is by Ku [1]. The LHP operates by using incoming heat to evaporate liquid on the outer surface of the porous wick into vapour which expands to fill the vapour grooves. Because of the pressure drop the vapour experiences as it flows through the grooves and its contact with the hot evaporator wall, it becomes slightly superheated before it flows into the vapour line. It is propelled through the vapour line and enters the condenser which removes the sensible heat before condensing it back into the liquid phase.

The condenser subcools the condensed liquid, which is vital for the successful operation of the LHP. The subcooled liquid is driven into the liquid line which then returns the liquid, which has

lost some of its subcooling through thermal contact with the ambient environment, to the CC. The function of the CC is two-fold: 1) to store excess fluid and allow for the mass swing in the transport lines and the condenser as fluid density and the two-phase region of the condenser change and 2) to continuously provide the porous wick with liquid as mass is evaporated. The first function is fulfilled by the large volume of the CC compared to the rest of the LHP. The CC should be designed to cope with the mass distribution change in the outer loop. The second function is guaranteed by the use of a bayonet or secondary wick.

A bayonet transports incoming liquid directly to the inner cavity of the wick. A secondary wick is similar to the wick in the evaporator but has a much larger average pore radius. It extends into the CC and passively draws liquid from it through to the primary wick. The LHP can have either of these or both. Liquid is drawn through the primary wick to the outer surface where it is boiled off, completing the circuit.

The fluid within the CC is considered to be at saturation as long as it is not flooded since the large volume of the CC produces a void. The difference between the pressure in the vapour grooves and the saturation pressure of the fluid in the CC is the pressure required to drive the fluid around the outer loop and is compensated for through the capillary action of the primary wick.

Maydanik [2] identifies the porous wick as a thermal and hydraulic lock. The wick separates the superheated vapour from the saturated fluid and ensures that the fluid flows in the correct direction by using the viscous nature of the liquid and its resulting capillary action to prevent vapour from penetrating the wick. The vapour in contact with the evaporator wall receives most of the input heat and is at a higher temperature than the fluid in the CC. This generates the necessary pressure difference to produce flow in the outer loop. These features produce the diodic action which allows the LHP to operate passively.

Both Ku and Maydanik [1,2] complement their analysis of LHP operation by demonstrating the steady-state thermodynamic cycle of the LHP on Pressure-Temperature graphs, adaptations of which can be seen in Figure 1-2. These are not to scale and assume isothermal vapour and liquid in their respective transport lines. The graphs indicate the pressure drop and subsequent superheating of the vapour after it boils on the outer surface of the wick before encountering a pressure drop through the vapour lines. In the condenser, the vapour rejects its sensible heat, condenses and subcools. The subcooled liquid experiences a pressure drop through the liquid line and enters the CC. The liquid undergoes another pressure drop as it is drawn through the wick, before the capillary force of the wick raises its pressure as it evaporates. The liquid below the menisci undergoes a number of non-equilibrium states as it changes phase and increases its

static pressure and is simply represented by the dashed line [3]. The CC fluid is either at saturation, shown in the top graph, or flooded, shown in the bottom graph. In the latter, the CC fluid point translates left as the CC is flooded with liquid.

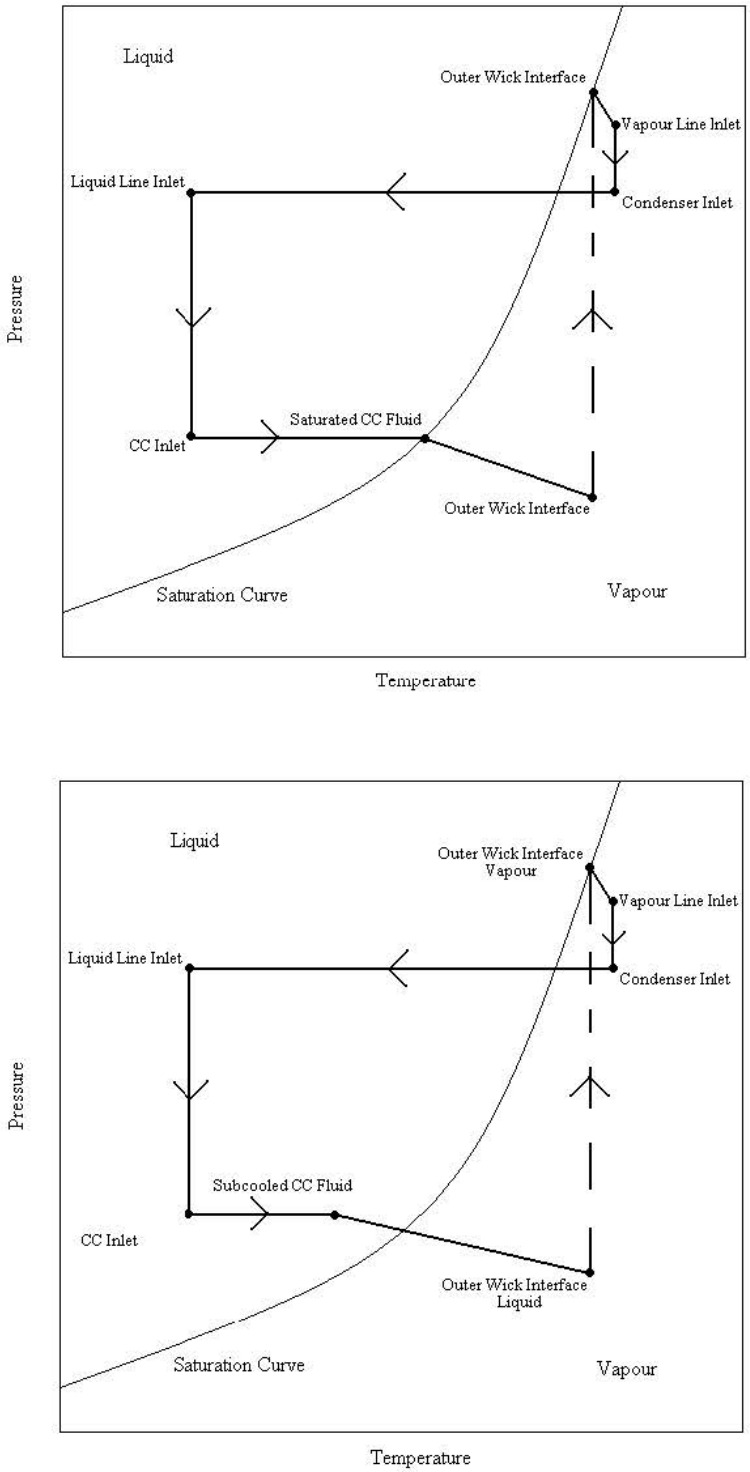

Fig.1-2. *P-T* graphs of LHP operation for saturated (top) and subcooled (bottom) CC fluid adapted from [1] and [2]

1.4. Advantages and disadvantages of thermal management using LHP

The LHP was invented in response to a need in aerospace applications for heat transfer devices with adequate thermal conductances and which could operate over long distances between the heat source and heat exchangers despite varying gravitational conditions. Conventional heat pipes are also passive, two-phase heat transfer devices with a porous wick, but their performance significantly decreases when subjected to these conditions. Attempts to increase their capillary head fail for the following reason: increasing the capillary head requires reducing the wick pore size which increases the pressure drop across the wick in proportion to the square of the pore size [2]. The increased capillary head does not compensate for the increased pressure drop because conventional heat pipe wicks are broad and long and the pressure drop increases significantly as the pore radius is decreased.

The LHP overcomes this with the employment of a suitable porous wick. The wick is sintered from powder to form a porous body with fine pores which significantly improve the capillary head. The pressure drop through the wick is decreased by reducing the distance the liquid has to travel. Instead of extending through the entirety of the volume, the wick of an LHP is located solely in the evaporator. The liquid is drawn through the wick radially and only suffers a marginal pressure drop which is amply compensated for by the large capillary head. A comparative approximation of the difference in fluid passage through the wicks in conventional heat pipes and LHPs is shown in Figure 1-3. This gives the LHP its most prominent feature: a capillary head many times greater than most heat pipes.

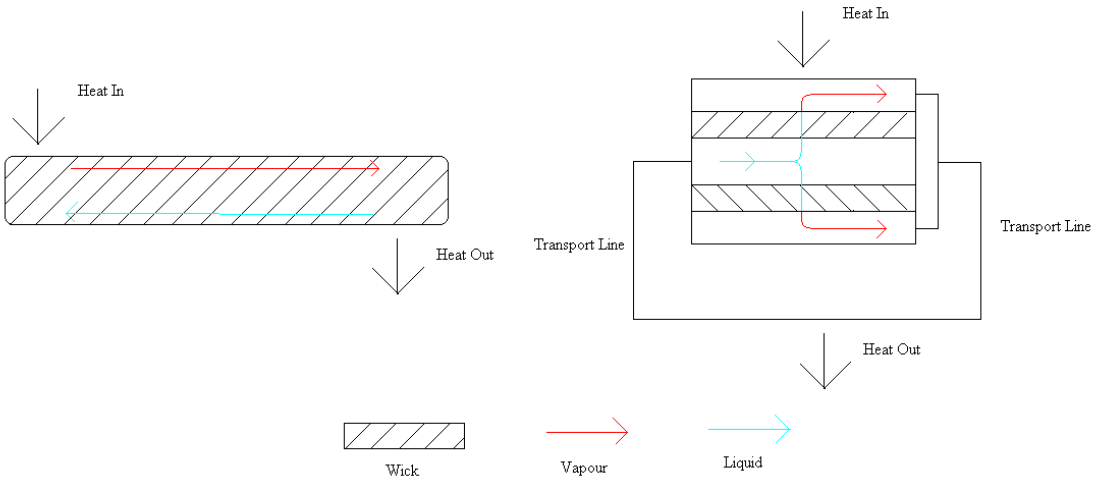

Fig.1-3. Visualisation of fluid passage through a conventional heat pipe (left) and an LHP (right)

In aerospace applications, the large capillary head allows the LHP to maintain fluid circulation when gravity is acting adversely. The same LHP can also operate in lower adverse gravitational positions, microgravity, assisting gravitational positions and on earth during ground tests. LHPs are able to do so because of the two-phase menisci which form in the pores of the wick. The radii of curvature of the menisci respond to the pressure difference between the high pressure vapour above the menisci and the low pressure liquid beneath them. The capillary pressure the wick produces is a function of this curvature. The menisci curvature increase to develop larger capillary forces in automatic response to larger pressure differences across their interfaces. This is the second advantage LHPs offer: they can self-start and auto-regulate passively [1]. A disadvantage of this passivity is that startup and auto-regulation may take many minutes and require large temperature overshoots before steady-state is reached.

A third advantage of LHPs is the use of smooth, hollow tubing for the transport lines and condenser. The tubing can have small diameters due to the pressure drop through them being amply accommodated by the capillary head. The large capillary head also allows the transport lines and condenser to be bent, elevated and extended many metres in length. This makes LHPs more configurable that other heat pipes and they offer a large degree of design flexibility. An illustration of a complex transport line and condenser configurations is supplied by Anderson *et al.* [4] and Dussinger *et al.* [5] as they discuss the development of an LHP for the TacSat-4 satellite. An image of the LHP developed is shown in Figure 1-4.

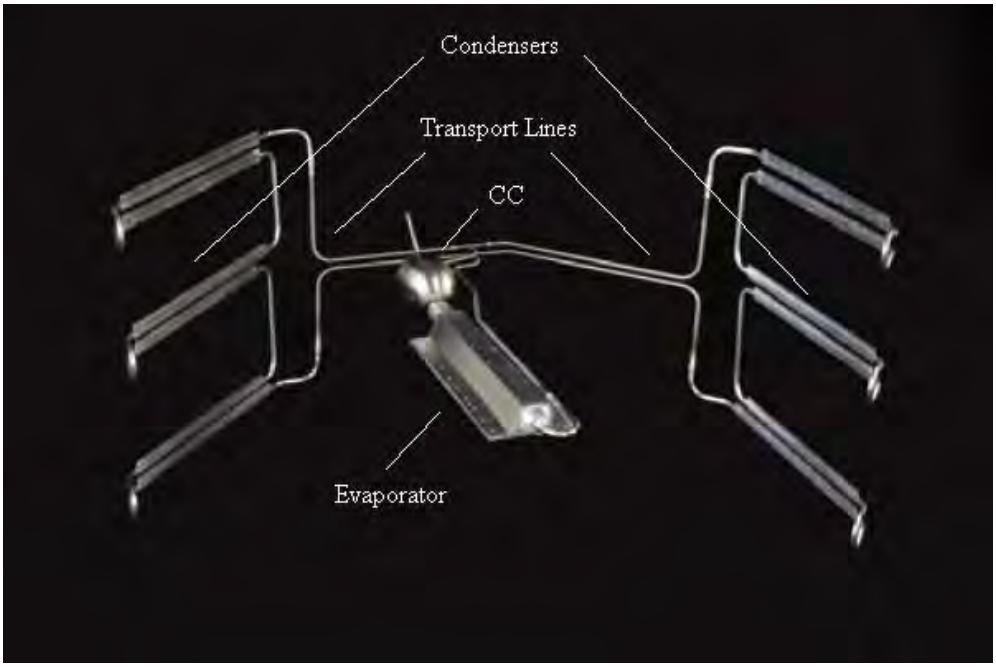

Fig.1-4. LHP developed for TacSat-4 [5]

This LHP was designed for satellite thermal management and required a complex piping network between the evaporator and two radiator heat sinks. The LHP also employed a parallel condenser flow balancer to handle fluid returning from two different condensers, one of which may be vapour filled during exposure to the sun. The flow balancer, connected to both liquid lines, has two porous membranes installed in the pipe cross-section. These behave like hydraulic diodes and prevent vapour from accessing the CC inlet line. The capillary head developed in the wick overcomes the pressure drop across the porous membranes and additional pressure drops in the complicated system.

Passive self-startup has certain limitations. The LHP can self-start as long as the primary wick has continuous access to the liquid in the CC. Without access to liquid, the wick will suffer dryout and the LHP will fail. This can readily occur when the evaporator is elevated above the CC, allowing liquid to collect away from the wick. The capillary pumped loop (CPL) is a heat transfer device similar to the LHP but invented six years earlier [6]. A schematic is shown in Figure 1-5. Both the LHP and the CPL employ localised wicks in the evaporator and hollow transport and condenser lines. A CPL, however, does not have an integrated CC and thus does not have constant liquid/wick contact. Startup consists of actively heating a separate reservoir which expands liquid into the wick core and allows the system to start.

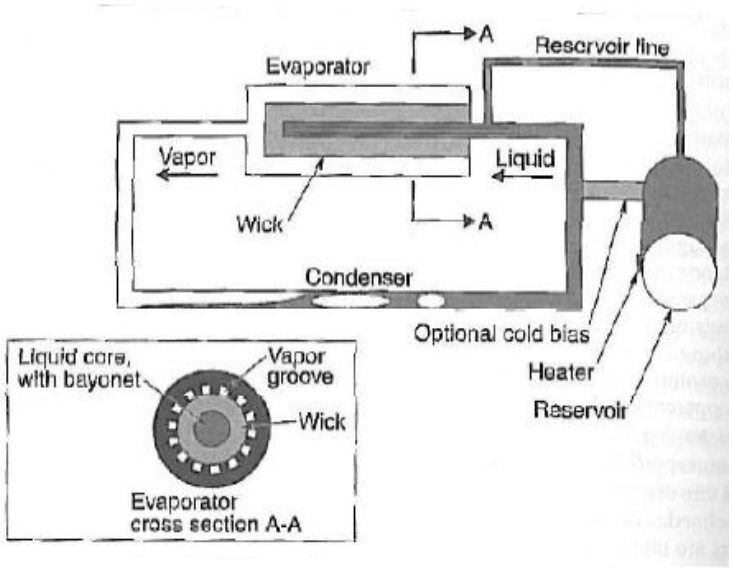

Fig.1-5. A capillary pumped loop [7]

Startup in a CPL is guaranteed for all orientations but requires an active thermal control to function, differentiating it from the completely passive LHP [8]. Because of this active control, a CPL reaches steady-state sooner than a comparable LHP and constant temperature control, performed through thermal control of the reservoir, is easier over large heat loads [1,3]. LHP

temperature control is performed through heating or cooling the CC but is difficult to achieve due to the thermal interconnectivity of the superheated vapour and CC fluid. As a result, the CC of an LHP requires more cooling during temperature control than a CPL reservoir.

These benefits do not, however, outweigh the attractiveness of pure passive operation and automatic startup which LHPs offer and focus has shifted towards LHP deployment over CPL [3,6]. Liquid contact can be assured without active thermal control in an LHP by the installation of a secondary wick. The secondary wick extends into the CC and is in constant contact with both the CC liquid and primary wick, providing the latter with a continuous supply of liquid and removing vapour which collects in the wick cavity [3]. Apart from guaranteeing startup, the secondary wick also decreases startup times, allows the system to be tolerant of vapour and non-condensable gases (NCG) in the wick core and allows the LHP to function in microgravity or with the CC below the evaporator [6].

LHP passivity also produces some disadvantageous behaviour during transient periods. Two such transient behaviours are temperature overshoot and temperature hysteresis. When a heat load is suddenly placed on the LHP, the temperature of the evaporator increases until a certain point, after which it rapidly drops to steady-state. Ku [1] found that temperature overshoot occurs due to the close thermal dependency of the evaporator vapour and the CC fluid. Even though the primary wick is a thermal lock, a portion of heat is transferred to the CC by conduction through the wick and liquid in the wick, raising the CC fluid temperature as the vapour temperature increases. However, as the mass flow rate increases, the liquid exiting the condenser remains subcooled for longer, and the CC fluid temperature decreases. In order to maintain the correct pressure difference across the wick, the vapour temperature begins to decrease until a stable temperature is reached. The rate at which this transition occurs and the degree of overshoot is dependent on the mass distribution in the CC and evaporator but can be many degrees over the steady-state and may even transgress the upper temperature limit of the device.

Temperature hysteresis is the difference between steady-state operational temperatures of an LHP for a given heat load, depending on the heating regime. For instance, an LHP under a power cycle from 10 W to 150 W was found to have lower operating temperatures below 100 W than the same LHP run from 150 W to 10 W at the same heat loads [1]. Temperature hysteresis is also dependent on the size of incremental heat load variation. A power cycle from 50 W to 400 W to 50 W demonstrated that the steady-state operational temperature of the system at the final 50 W heat load was 4°C larger than the first 50 W steady-state operational temperature [1]. This is caused by the different changes in mass distribution when the system is increasing or decreasing its heat load, specifically in the inner core of the wick [1]. Increasing heat load is

shown to increase the amount of liquid in the wick core while decreasing the heat load, especially in large increments, causes vapour to collect in the wick core. The vapour increases the heat leak through the wick, increasing the CC fluid temperature and consequently the operational temperature. Temperature hysteresis does not occur at high heat loads due to large mass flow rates collapsing the bubbles of vapour in the inner core, preventing the increased thermal resistance they produced.

Zhang *et al.* [9] investigated how different mass distributions in the CC would result in different temperature overshoots and startup times. The worst startup situation is when vapour is present in the wick core and the vapour grooves are filled with liquid. The startup at 5 W took 40 minutes to complete, compared to only 1.6 minutes when the system has an ideal mass distribution of vapour in the vapour grooves and liquid in the wick core [9]. The suggested reason for this poor performance is the boiling of the saturated fluid in the CC before the liquid in the vapour grooves can achieve nucleated boiling, due to the increased heat leak through the vapour present in the wick core. Boiling of the CC fluid also increases the pressure in the CC, stifling flow through the system and raising the temperature overshoot. When the LHP finally starts up from this situation, the steady-state operating temperatures are much higher due to the continued presence of vapour in the wick core.

Occasionally the pressure in the CC will build until the flow is no longer stifled but goes in the opposite direction, drawing liquid from the vapour grooves through to the wick core. This reverse flow was studied by Zhang *et al.* [9] and is identified by a high condenser outlet and a low condenser inlet temperature. This is also caused by vapour presence in the wick core. Reverse flow is confined to low heat loads as the high mass flow rate produced by large heat loads collapsing the bubbles. Zhang *et al.* [9] indicate that because the CC has a higher thermal capacity than the vapour grooves, the adverse mass distribution discussed can occur once the LHP has shut down as condensation in the vapour grooves occurs before condensation in the CC.

Zhang *et al.* [9] also describe temperature oscillation. This occurs at low heat loads when the two-phase interface in the vapour line oscillates about the condenser inlet as the pressure difference across the wick is insufficient to allow it to settle. This causes an increase in the overall operating temperature of the system. Another type of temperature oscillation occurs at the condenser outlet at high heat loads as the vapour has not yet completely condensed by the time it reaches the end of the condenser. These oscillations can be stopped by increasing and decreasing the heat load respectively.

Launay *et al.* [6] note that low heat loads or particularly cold pre-startup conditions may cause the LHP to fail as the large viscous forces in the lines stifle flow. Flow may also be impeded at high heat loads by vapour velocities which exceed sonic speeds. They also note that even if all the startup conditions are optimal, the system still may not reach steady state due to the close thermal interdependence of all the components.

1.5. Applications of thermal management using LHP

LHPs have been used in aerospace applications in the thermal management of electronics, batteries, structures and sensors of satellites and spacecraft [8]. They also have terrestrial uses, such as refrigeration and air-conditioning, avionics thermal management, computer cooling and water heating [8].

The first flight tests of an LHP began in 1989 onboard the Gorizont and Granat spacecraft [1,2,3]. The Gorizont LHP used a three evaporator/collector condenser system shown in Figure 1-6 and tested serviceability of the LHP in microgravity with heat loads of 40 W, 80 W and 120 W. This was successful but the Freon-11 used was found to freeze. Propylene was used aboard the Granat and over a number of years showed favourable results [2].

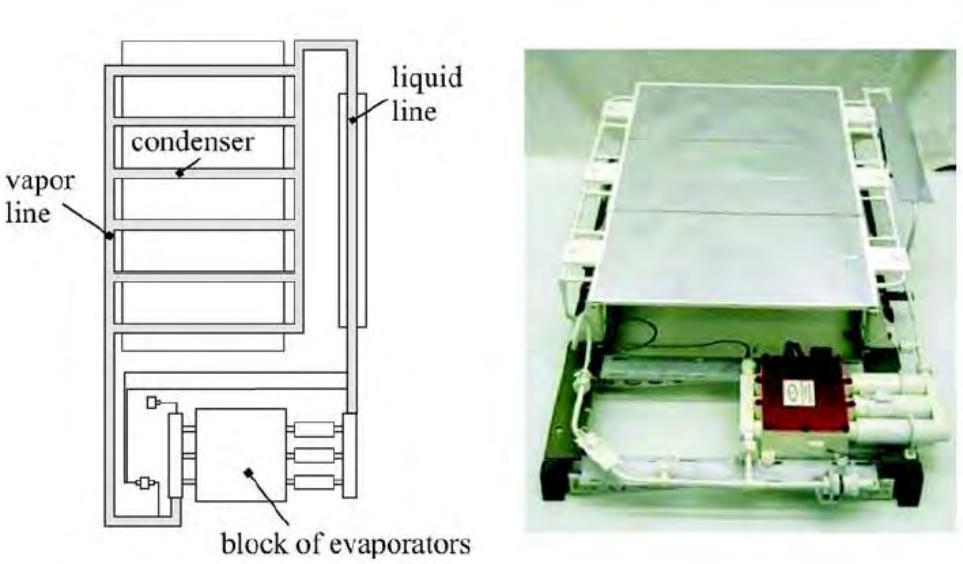

Fig.1-6. LHP used in first flight tests onboard Gorizont and Granat [2]

The first commercial use of an LHP was employed in the Russian satellite Obzor in 1994. Two ammonia LHPs and one propylene LHP were used to cool optical equipment. American aerospace scientists also began experimenting with LHPs and tested one on the Space Shuttle STS-83 and STS-97 in 1997 to determine its abilities in microgravity. Another LHP was installed in the Space Shuttle STS-87 to test American-made LHP performance against Russian-

made LHP performance. These details are summarised by Maydanik and Ku [1,2]. Six LHPs have been installed on the Russian spacecraft Mars-96 and the Chinese meteorological satellite FY-IC as well as on six American Hughes 702 satellites [2]. An LHP has also been used in the Geoscience Laser Altimetry System (GLAS) aboard the ICESar spacecraft [1] as well as the Netlander spacecraft and Mars Pathfinder [3].

Riehl [8] suggests that most spacecraft applications call for about 150 W of heat to be dissipated at temperatures below 100 °C and reports on the development of three LHP for satellite installation. One LHP has its CC detached from the evaporator body while another has an integrated CC. The comparison showed that the integrated CC has higher operating temperatures due to the close thermal coupling between the evaporator and CC. The final LHP incorporated circumferential grooves into the wick which bolsters performance. The LHPs were made of 316L stainless steel, with the transport lines and condenser having an inner and outer diameter of 2.85 mm and 4.85 mm, respectively. The vapour line was 550 mm, the liquid line was 850 mm and the condenser, cooled by an aluminum cold plate through a chilled ethylene glycol and water mixture, was 1000 mm. The evaporator was 100 mm long, with an inner and outer diameter of 16.5 mm and 19 mm and the CC had a 20 ml volume. The primary wick was made of polyethylene and, because these LHP were developed for satellites, had a secondary wick made of stainless steel mesh. The working fluid is acetone. Riehl [8] notes that ammonia is traditionally used as a working fluid but the hazards it presents make investigations into other refrigerants necessary. The LHPs were tested for the maximum heat load that they could transfer before the heat source reaches 100 °C for heat sink temperatures of 5, 0, -10 and -20°C. The highest safe heat load was 80 W and the data was used to produce a graph of LHP thermal resistance against heat load.

Anderson *et al*. [4] and Dussinger *et al* .[5] describe the construction and ground testing of an LHP, shown in Figure 1-4, which is the primary thermal transfer device onboard the tactical microsatellite TacSat-4. The LHP is made from 316 stainless steel, with the evaporator 305 mm in length with an inner diameter of 25.4 mm. The primary wick is made of nickel and the secondary wick made of a stainless steel mesh. The condensers are cooled with two aluminum cold plates to simulate the radiators on the TacSat-4. The working fluid is ammonia. The LHP ground tests show favourable operating temperatures and behaviour up to 700 W. The LHP was also tested in adverse tilt, where the evaporator is above the CC, and with condenser temperatures which vary from 50 to -20 °C. The transient response to heat load fluctuation and the low heat load startup limit were also tested. This LHP is an example of a ramified LHP, which is a LHP with multiple evaporators or condensers. Figure 1-6 shows a multiple evaporator ramified LHP.

Hartenstine *et al.* [10] describe a LHP for thermal management of nuclear power systems onboard satellites and spacecraft. Their LHP is required to dissipate at least 500 W while minimising the mass of the LHP. For this latter requirement, a titanium/water LHP has been constructed as these were found to have the greatest heat dissipation for their mass. The evaporator has an outer and inner diameter of 25.4 and 22.9 mm respectively and is 203 mm long with an aluminium saddle. The CC volume is 26.1 ml. The vapour line and condenser are both 6.35 mm in diameter while the liquid line is 3.18 mm. The vapour line and condenser diameters are larger to reduce the pressure drop. The transport lines are both 2 m long and the condenser is split into two parallel sections which reconnected with the liquid line using a parallel flow balancer. This reflected the typical arrangements for spacecraft radiators [10]. For ground tests, the heat exchanger was an aluminum cold plate cooled with water, over which the condenser lines were attached in serpentine shapes. The LHP can dissipate 550 W at an adverse elevation of 5 cm.

Although LHPs were developed for aerospace applications, their first real use was for terrestrial electronics cooling, dissipating 30 W [2]. They were then used to dissipate 10 W from quantum-electronics, an application where space around the heat source was limited and the LHP transport capabilities could be exploited [2]. The first use of an LHP for personal computing cooling was self-contained laptop CPU cooling LHPs in 2001 which could only dissipate about 30 W but only weighted 50 g [2]. These latter LHPs are shown in Figure 1-7.

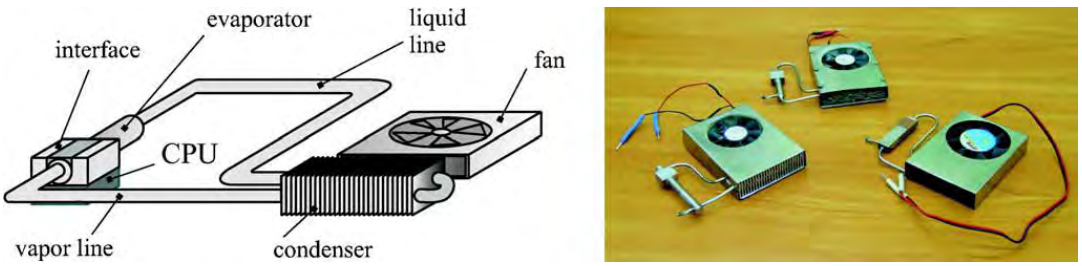

Fig.1-7. CPU cooling LHP for laptops [2]

Pastukhov and Maydanik [11] use LHPs as an innovate method of reducing fan noise in computer thermal management by dissipating the heat outside the casing. A few LHP configurations have been developed, using water as the working fluid and dissipating heat in a variety of wide, finned heat exchangers on the outside of the casing, one of which can be seen in Figure 1-8. Of these, the collector type heat exchanger is the most effective. These LHPs are able to dissipate 100 W to ambient temperatures of 22°C while still being below 70°C. The LHP performance is improved by using a thermosyphon, radiator and thermoelectric cooler attached to the CC. Their combination allows 180 W of heat to be dissipated while the operating temperature rose to 75°C.

Fig.1-8. Computer Cooling System [11]

With terrestrial electronics cooling, the research trend is to minimise the size and weight of the LHP by designing smaller evaporator bodies, or to develop new evaporator shapes which can be fitted directly onto the CPU, removing the thermal resistance and weight of a saddle. Maydanik [2] notes that the advantages of LHPs are more pronounced when the system is very large. Miniaturisation is still sought however.

Pastukhov *et al*. [12] tried to develop a miniature LHP (mLHP) for notebook computers with evaporator diameters of 6 mm and 5 mm. They note that while desktop processors require 50-100 W of heat to be dissipated, notebook processors require only 20-35 W to be dissipated but have spatial constraints which influence the LHP design. Two sets of mLHP have been developed with an operating temperature of 100°C. The first set has relatively long transport lines and a remote air-cooled or cold-plate heat exchanger which dissipate up to 40 W of power in any inclination and is intended to reflect an idealised electronics cooling system where the heat is dissipated far from the heat source. The second set focus on a setup in which the processor and condenser are on the same PC board. These have 5 mm diameter evaporators with a finned, forced convection heat exchanger 30 mm away. These operated in an ambient temperature of 50°C or more to reflect conditions within the computer case. The first set of LHP designs are able to transport 80 W at any orientation while the second set dissipated a maximum heat load of 30 W, largely influenced by the heat sink temperature.

Maydanik *et al*. [13] describe a number of mLHPs with cylindrical evaporators of 5 mm and 6 mm diameter with 20 mm wick active lengths, which better match the size of the surface being cooled. Due to their cylindrical shape, copper saddles are still needed, which increases the

overall thermal resistance of the LHP. The transport lines and condenser are 2 mm in diameter and the transport lines are about 200 mm long, while the condenser length is 63 mm. The heat exchanger which was developed is a tube-in-tube type with a device for increasing the swirl and turbulence of the incoming vapour. This allows full condensation to occur rapidly over the short condenser length. The heat exchanger is also finned and air or water cooled at 20°C, 30°C and 45°C to simulate the conditions in which electronics would be cooled. Testing found that they dissipate about 100 W while still within the 100°C evaporator wall temperature limit, demonstrating that an mLHP could still dissipate sufficient amounts of heat despite a reduction in size. The LHPs were not tested for the affects of gravity, which is a concern as Maydanik *et al*. [13] did not consider the layout in an actual application.

Chen *et al.* [14] discuss the performance testing and transient behaviour of the first mLHP to utilise a 5 mm diameter evaporator, which seems to be the limit in evaporator size reduction. The transport lines have inner and outer diameters of 1.5 and 2 mm respectively. The mLHP uses ammonia as its working fluid and the heat exchanger is a design similar to the tube-in-tube type with a solid core installed in the condenser and the outer casing finned. The condenser temperature was changed between 25°C, 15°C and 5°C as heat load tests proceeded. The mLHP is capable of transporting a maximum of 70 W with an evaporator wall temperature of 75°C. The only orientation it cannot successfully operate under was adverse tilt, with the mLHP only able to deliver 15 W at 70 °C. Temperature oscillations occur when the mLHP operates in any adverse elevation or tilt.

Maydanik *et al.* [15] describe the application of an mLHP in a server system. An 8 mm diameter evaporator with a 59 mm active length was attached to the CPU using a copper heat spreader. Ammonia is used as the working fluid. The lines are about 800 mm long with a diameter of 2.5 mm and run between the evaporator and condenser at a level height. The three heat exchangers tested were a finned cold plate cooled through forced convection using one to four fans, a cold plate, cooled by temperature controlled water, and a water jacket which fitted over the condenser. The quantity of heat dissipated was dependent on the heat exchanger and the best heat exchanger is either the water cooled cold-plate or water jacket, which allows up to 120 W of heat to be dissipated whilst remaining below 70°C. The use of a copper heat spreader demonstrates that evaporators may be bulkier than the application allows. Research into minimising the components should be pursued for these applications.

Not all mLHP have cylindrical evaporators. Some mLHP have flat evaporators with a disc-shaped wick which can be fitted directly onto the processor. Maydanik [2] discusses a few flat evaporators of varying size, which are still able to transport working fluid over a few metres and under heat loads ranging from 50 W to 160 W. Flat evaporators typically require thick walls and

experience higher operating temperatures than cylindrical wick LHPs due to the short distance between the heat source and CC [3]. Some flat, circular evaporators are shown in Figure 1-9, along with a schematic view.

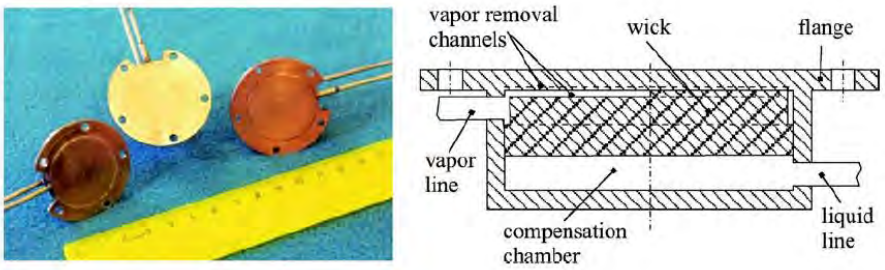

Fig.1-9. Flat evaporators [2]

Singh *et al.* [16] investigated the operational characteristics of a flat evaporator mLHP. The evaporator is 30 mm in diameter and 10 mm thick, with vapour grooves machined out of the evaporator body which pressed against a disc-shaped wick. To further reduce thermal resistance, the evaporator body is made of copper and water is used as the working fluid. The transport lines are 290 mm in total length with a 2 mm inner diameter and the condenser was an air-cooled, finned tube which dissipated heat to an ambient temperature of 22°C, typical of thermal management in PCs. The maximum heat load is 70 W while operating temperatures are below 100°C. The transient response of the mLHP was investigated during startup and it was found that temperature oscillations occur at low heat loads, with the frequency of the oscillations increasing and the amplitude decreasing with increasing heat loads until they subside.

Tang *et al*. [17] describe an mLHP with a novel rectangular evaporator. It has a complex and finely made wick which fitted into an 18 mm high evaporator with 50 mm sides. The outer loop length is 800 mm and the condenser, which was relatively novel and complicated, was finned and air-cooled. All testing was conducted in the gravity-assisted position, that is, the condenser was above the evaporator. The working fluids were ethanol and water. The testing showed that the LHP operated up to 150 W before it passed 100°C, making this mLHP one of the most successful in terms of size optimisation and performance. Despite this success, the nature of the evaporator, wick and condenser suggests that their construction may be more time consuming and expensive than with other LHPs. Expense and manufacture time are both strong arguments against LHP use, especially in terrestrial applications where traditional heat pipes are already successful, and thus these elements of this LHP count against it.

Not all terrestrial LHP research focuses on reducing the size of the system. Kobayashi *et al.* [18] developed an LHP with a 7500 mm total outer loop length, and inner and outer diameters of 2

and 3 mm respectively, which incorporates flexible tubing. This is known as a flexible LHP (FLHP). As the pressure drop through the lines is variable, a high capillary head is necessary which is accomplished by using wicks made from Teflon powder with a pore diameter of 1.2 μm. Kobayashi *et al.* [18] bypass the dangers of using ammonia by selecting R134a as the working fluid since it produces much lower pressures and is safer and easier to handle. The FLHP is only capable of dissipating up to 80 W in horizontal operation. This suggests that, unless the application requires flexible piping, it would be better to form a stationary transport line shape and use a superior refrigerant. Maydanik [2] describes two FLHP designs, in which the transport lines have numerous separate flexible portions while still remaining quite long. These were designed for high heat loads and employ ammonia, allowing heat loads of 1500 W and 1000 W.

LHP terrestrial electronics applications are not restricted to computer processor cooling. Vasiliev *et al.* [19] developed a LHP for high powered insulated-gate bipolar transistor (IGBT) elements and similar electronics which can dissipate large amounts of heat. The evaporator is 334 mm long and has an inner and outer diameter of 16 and 18 mm respectively while the CC has a volume of 31.8 ml. The total transport line length is 3500 mm and the vapour line and condenser have inner and outer diameters of 5 and 6 mm respectively while the liquid line has an inner and outer diameter of 3 and 4 mm respectively. The heat exchanger is a coaxial jacket through which 20°C water is pumped. In their testing, the maximum heat load which could be dissipated with an operating temperature below 100°C was 900 W using a titanium wick and water as the working fluid while only 300 W could be transferred using a nickel wick and acetone.

Lu *et al.* [20] developed an LHP for high powered LED units, which require 100 W of heat to be removed below 110°C. They created a novel LHP with a flat, rectangular evaporator with the CC attached on the side and the primary wick extending into the CC to ensure liquid contact. The working fluid is water and the casing and wick are copper. The transport lines are both 6 mm in diameter and the length of the vapour line is 140 mm while the liquid line is 1100 mm. The difference in line lengths is possibly to reduce the pressure drop. The condenser is cooled through natural convection by air with a temperature of 25°C and a velocity of 1 m/s. Startup transient performance was tested, as well as steady-state performance at an adverse elevation of 30°.

From the above, it can be concluded that LHPs in aerospace applications always employ a secondary wick to withstand unfavourable gravitational environments. These LHPs tend to have long, complex transport line configurations and are designed to operate under a wide condenser temperature range, usually between -20°C and 50°C. They are tasked with dissipating around

150 W from onboard electronics packages while other thermal management systems, such as a nuclear power system, require much greater heat dissipation. A temperature limitation of about 100°C appears to be universal for electronics, even in terrestrial applications. Terrestrial LHPs tend to lack a secondary wick and orientations in which the CC is below the evaporator are rarely tested. Terrestrial heat exchangers work by forced convection, either by air or other coolant, and the temperature of the heat exchanger influences the overall operating temperature. The temperature of the heat exchanger, i.e. the condenser, is usually 20°C but can increase to around 40°C if the heat exchanger is simulating air inside PC casings or decreases to 0°C with coolant to improve the LHP performance. The heat loads which terrestrial LHPs can dissipate vary, but for computer processor thermal management a heat load of between 80 and 120 W seems conventional. LHPs which can dissipate increasing amounts of heat are favoured as they can more readily accommodate CPU power increases. The size of the LHP, particularly the evaporator, is related to maximum heat load.

Some common design choices emerge from this literature review. Stainless steel is popular for the evaporator casing and transport lines, although other piping materials such as copper, aluminum and titanium are also in use. The choice of working fluid determines which material is used. Incompatibility with the working fluids, such as ammonia, water and acetone, leads to corrosion, leaking or the formation of NCG. For high heat load applications, a titanium LHP with water as the working fluid is best while for smaller applications, a stainless steel LHP with a nickel wick and ammonia as the working fluid is popular and efficient. For all LHP devices, transport lines with inner diameters ranging between 2 mm and 5 mm are common. Transport line length varies, but lengths of a few hundred millimetres for mLHP and small scale terrestrial LHP are usual while larger LHPs with greater heat loads have transport lines a few metres in length. A transport line design alternative is to reduce the pressure drop caused by the high velocity vapour by increasing the diameters of the vapour and condenser lines. Another method is to reduce the vapour line length. Most experimental LHP devices use around 20 thermocouples throughout the system, including up to 6 on the evaporator and CC. The mass charge of working fluid which the system receives must be sufficient to ensure that half of the CC volume be filled with liquid during a cold startup. Finally, there is little information as to how to hermetically seal the CC from the evaporator although it appears that an interference fit between the inner diameter of the evaporator casing and the outer diameter of the wick may be sufficient. Ambirajan *et al*. [3] mention a laser welded seal being used but state that little information is available in the literature due to the proprietary nature of sealing technology. Flat evaporators are sealed with an O-ring fitted around the circumference of the wick.

1.6. Modeling of LHP

LHP models attempt to explain and predict the behaviour of various sections of the device either under steady-state or transient conditions. These can take the form of mathematical models, in which thermodynamic and fluid mechanic equations of state are used to determine values such as the temperature, pressure and enthalpy at each point in the system, and numerical models, which, because of their greater complexity and the need for iterative solutions, require greater processing power and time. Numerical models are usually only used to solve the thermodynamic properties of a single component, such as the evaporator or condenser, due to the importance of these components in defining LHP operational characteristics. Comparisons between the temperature profiles of the simulated and experimental data are usually the metric by which the accuracy of the model is judged. A typical model validation is shown is Figure 1-10.

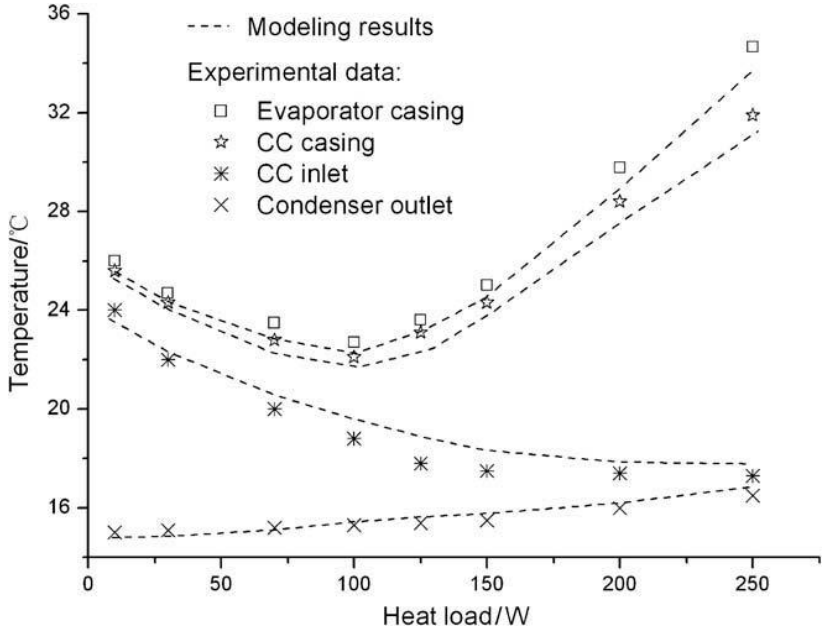

Fig.1-10. Model results compared to experimental data [23]

An early steady-state mathematical model of a terrestrial LHP was developed by Kaya *et al.* [21]. The model includes a number of assumptions and omissions but is noteworthy for a few key methods which ease the modeling process and permit a solution. The model assumes that the thermophysical values of an LHP under constant heat load, ambient and condenser temperature are those which allow a mass and energy balance across the system. Each component is analysed separately. The evaporator and CC are considered as a network of interconnected nodes and a heat leak between the two-phase interface in the wick and the CC fluid is included. This heat leak is a function of the thermal conductivity and geometry of the wick and equations for the thermal conductance of the wick are given.

A temperature change occurs in the transport lines due to the thermal contact between transport lines and the ambient environment. The two-phase region of the condenser has an annular flow regime and is modelled using single phase correlations. This is a weakness in the model as two-phase modeling is complex and single-phase analogs do not produce accurate results [22]. The thermal conductance values in the transport lines and condenser are not explicitly given.

The model treats the fluid on the outer surface of the wick and the fluid in the CC as being at saturation and connected by the Clausius-Clapeyron relation:

$$\Delta T = \left(\frac{\Delta T}{\Delta P}\right)_{sat} \Delta P_{system} = \frac{h_{fg}}{T(v_{vapour} - v_{liquid})} \Delta P_{system} \quad (1)$$

The temperature difference between the evaporator and CC can be calculated from their pressure difference, given by pressure drop through the outer loop, and the slope of the saturation curve given in Eq. (1). This assists in solving the model as unknown quantities such as the heat leak and energy balance can be calculated. These pressure drop equations, including the pressure drop through the wick, are not supplied. Kaya *et al.* [21] do not discuss the LHP modeling process when the CC floods and the Clausius-Clapeyron relation can no longer be used. Despite this, the model is reportedly accurate to 3%, possibly due to the use of empirical values to supplement their model.

Bai *et al.* [23] developed a relatively sophisticated steady-state mathematical model. The LHP is separated into sections and the model determines the thermophysical properties throughout them, the solution ultimately found through an energy balance across the CC. The analysis of the evaporator and CC was through a nodal network. There are two heat leaks between the evaporator and CC: a heat leak between the evaporator wall and CC wall, and a heat leak between the saturated vapour in the evaporator and the fluid in the CC. By analyzing the energy balance through the wick using Navier-Stokes equations, the wick thermal conductance is calculated, with the thermal conductivity bolstered by empirical data. These calculations are repeated to develop the thermal conductance for a two-layered wick and show the increased thermal resistance provided by the second layer. The second heat leak also contains a two-phase condensation and evaporation heat transfer between the surface of the wick core and the CC fluid. Bai *et al.* [23] do not provide any way of defining this two-phase heat transfer which is a significant omission.

The transport lines have a pressure drop and temperature change given by standard thermophysical equations. The condenser is broken into superheated, two-phase and subcooled regions, the first and last having the same equations as the transport lines. The two-phase region is considered to be annular and modelled numerically as the simultaneous equating of changes

in vapour quality, film thickness and liquid and vapour pressure. Bai *et al.* [23] added a momentum transfer term to the decrease in vapour pressure calculation. The model recognises that once the CC floods, the CC fluid becomes subcooled liquid with a temperature below the saturation temperature given by the Clausius-Clapeyron relation.

The model showed good agreement with their empirical data and could display pressure drops throughout the system, void fractions in the CC and superheated, two-phase and subcooled lengths within the condenser. Gravity was not taken into account which is a significant omission considering the tests performed for gravity-adverse and gravity-assisted operation and the commonality of elevation variation tests in LHP experimentation.

Bai *et al.* [24] describe a transient model for LHP startup analysis. The LHP is considered as a collection of nodes with a certain volume, connected by transient mass, momentum and energy equations. The transport line walls are included in this nodal network, allowing heat transfer between connected sections of wall and thermal creep to be modelled. The condenser model is the same one used by Bai *et al.* [23], but includes transient equations and wall conduction. The evaporator and CC are considered as a nodal network with transient terms. The model has excellent accuracy with startup data, with no more that 2°C difference between experimental and simulated results. Their model does not allow for startup under all initial conditions however. For startup when the vapour grooves are flooded, the model cannot calculate the necessary liquid superheat or predict the nucleated boiling process in the vapour grooves. This is a significant weakness as vapour groove flooding is not uncommon.

A transient mathematical model of LHP operation in aerospace applications was developed by Vlassov and Riehl [25]. It takes a nodular approach and simulates every aspect of the LHP, such as modeling CC fluid level fluctuations during startup. The condenser model is also transient and used to analyse the movement of the two-phase interface. Gravitational terms are included in the transport lines and condenser, which are uncommon in mathematical models, especially in the condenser. The mathematics model the entire two-phase region using the annular flow regime and prevent the gravitational component in the two-phase region from causing unsteady liquid/vapour interfaces and slug flow. The condenser model requires seven variables be solved.

The evaporator and CC model have nodal interpretations of the heat transfers and include transient equations. The heat leak through the wick incorporates the use of a secondary wick by breaking the heat leak into a heat transfer through the primary wick to the wick core and a heat transfer between the wick core and CC fluid through the secondary wick. The inlet liquid subcooling is broken up as well, with a portion reducing the temperature of the CC fluid while the rest goes to reducing the temperature of the wick core. A maximum difference of 5°C was

found between theoretical and experimental results for a heat load range between 2 and 60 W. The transient calculations and the numerical solutions in the condenser require a large amount of computer resources and processing time, making the model unattractive.

Chernyshev and Maydanik [26] produce a transient numerical model of the evaporator and CC which is able to simulate the startup of an LHP under any conditions, including when the vapour grooves are flooded and the wick core contains trapped vapour. The model separates the evaporator into a number of nodes, 8 nodes for the evaporator wall and 20 nodes for the wick, before applying temporal differential equations which describe the mass and energy between each node. The startup analysis suggests that the requisite superheating of the liquid in the vapour grooves, should they be flooded, enforces a lower boundary on the possible startup heat loads. Heat input to the evaporator below this minimum will prevent liquid superheat and nucleated boiling and prevent startup. Due to the large number of differential equations, this model requires substantial processing power and does not consider the LHP in its entirety, making it unattractive.

Kaya and Goldak [27] develop a numerical model of the steady-state conditions in the wick. A 2-D cross-section of the wick is considered and finite element analysis with mass continuity, pressure and energy governing equations are used solve the model. The model focuses on the area where the wick and evaporator wall meet, particularly the behaviour of the fluid in the wick at the interface. The wick is considered to be cylindrical and the evaporator wall has fins which protrude inwards and interface with the wick. The model found that the pores around the fin would be filled with superheated vapour, the menisci retreating some distance down the pores. The model attempted to analytically calculate the effective thermal conductivity of the wick but found that by varying superheated vapour volumes around the fins, including a completely liquid saturated wick, a variety of thermal conductivity values were produced.

LHP models can be implemented in a number of numerical software packages, although SINDA/Fluint is the most popular [21,25,28]. Vlassov and Riehl [25] describe the creation of EASY software which was developed for LHP modeling and design. In industry, modeling and design is usually performed using SINDA/Fluint directly or GUI front-end software based on SINDA/Fluint such as Thermal Desktop [3]. Thermal model generator (TMG) by MAYA Heat Transfer is also used [3]. To the author's knowledge, MATLAB software has never been used to model an LHP. The models discussed all relied on empirical data particular to the LHP they were modeling for accurate results, preventing them from being used as general LHP design software. LHP design is an area of potential innovation as a quick, simple but reasonably accurate analytical model could be used to experiment with various LHP configurations. The configuration which best suited the needs of the application could then be used.

1.7. Wick manufacture

Most LHP research articles give the physical properties of the wick or wicks used, such as the material they are made of, their porosity, permeability, pore radius and thermal conductance, which indicates the range of properties wicks can have. The few articles available on wick sintering detail the techniques commonly employed. They also detail analytical and experimental techniques to test the wick properties.

LHP wicks can be made of metals, plastics or ceramics [2]. Metallic powders are the most popular, with nickel, titanium, copper and stainless steel powders commonly used [30]. Nickel is very popular [5,8,9,13,15,16,19,23,24], predominately due to its corrosion resistance. Titanium is also common due to its low mass and relative corrosion resistance [10,12,13,14,19]. Plastic powders such as Teflon [18] or polyethylene [8,25] are also employed. Most wick fabrication studies use nickel powders [29-34], although there are variations in powder type. Reimbrecht *et al.* [31] used a mixture of powdered nickel carbonila and atomised nickel while Yeh *et al.* [32] uses filamentary nickel powder. The most common is Inco 255 nickel powder [29,33,34], which has a small particle size of 2.2-2.8μm and highly spherical particles. Some studies attempt to improve the properties of the wick by mixing the primary powder with additives. Xin *et al.* [29] sintered nickel/copper wicks, attempting to use the copper as a binder to improve strength and lower the melting temperature of the mixture. Yeh *et al.* [32] created a biporous wick, which is a single wick which has clusters of fine pored regions separated by larger pores. They used Na_2CO_3 as a pore former, which simply dissolved in water once the wick is sintered, leaving large pores within the wick structure. Samanta *et al.* [30] mix nickel and polypropylene and use paraffin wax and polyethylene as binders which are eventually removed in the debinding process and are expected to improve porosity. Since research on wick fabrication is so scarce, the effects of additives have yet to be definitively determined. More experimentation, as well as cost-benefit consideration, should to be conducted to determine if additives improve the quality of the wick.

There are four crucial properties of the sintered wicks. These are the porosity, which is the void volume of the wick over the total volume; the average pore radius, which indicates the capillary head the wick is able to exert; the permeability, which indicates the ease by which fluid passes through the wick; and the thermal conductivity of the wick. Porosity ranges from 50-80% [31,33], although most wicks have porosities closer to 55-60%. The average pore radius can be between 0.5-30 μm [29,32], but is usually 1μm in terrestrial LHPs. Permeability is normally between 0.2×10^{-13} m^2 and 20×10^{-13} m^2 [2]. The thermal conductivity of the wick is normally 5-10 W/mK for nickel wicks [2], although it is dependent on porosity.

Although literature on sintering wicks is scarce, Xin *et al*. [29] introduce the most popular methods. These are the loose powder sintering and cold-press sintering techniques. Loose powder sintering involves pouring the powder into a mould and then sintering the wick. Cold press sintering requires compressing the powder in the mould to form a compact wick which is then sintered. A simple schematic of cold-pressing technique is shown in Figure 1-11. Cold-press sintering allows for better control over the properties of the wick once it is sintered, as these are functions of the compressive force on the compact. Loose powder sintering produces better porosity and permeability than cold-press sintering but the properties are uncontrollable and non-uniform throughout the wick volume.

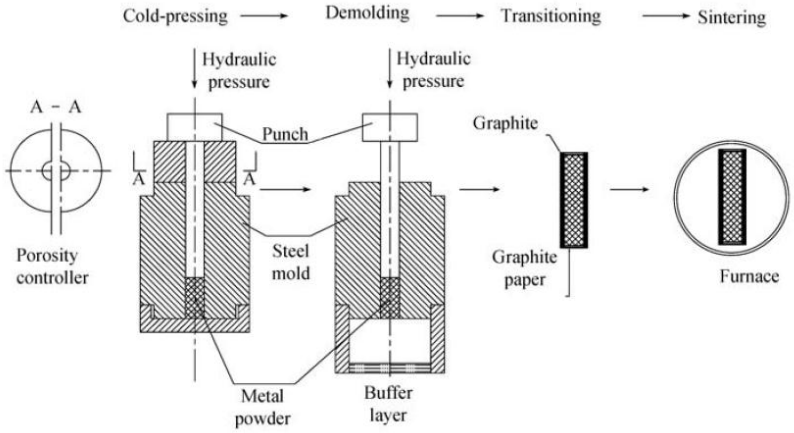

Fig.1-11. Schematic of cold-press sintering [29]

The heating regime, which is the temperature and period at which the wicks are sintered, is influential. Xin *et al*. [29] suggests a sintering temperature of 630°C for 30 minutes, Zan *et al*. and Chu *et al*. [33,34] suggest 630°C for 15 minutes and Wu *et al.* [35] suggest 600°C for 45 minutes. The rate of heating is also important and Wu *et al.* [35] suggest a rate of 10°C/min while Xin *et al*. [29] propose a heating rate of 20°C/min. Sintering temperatures, times and heating rates are evidently controversial and experimental.

With respect to machining the vapour grooves and wick inner cavity, Xin *et al*. [29] compared machining the wicks, using drills and milling machines, with electro-erosion. Electro-erosion completely fuses pores shut as the metal melts, while machining does little damage. Other studies [19,30,34] attempted to sinter the wicks with the required vapour grooves and wick core. Chu *et al*. [34] used sticks to produce the wick core during sintering, and Vasiliev *et al.* [19] developed an innovating method of forming a compact wick with vapour grooves.

There are a number of methods to measure each property. Porosity can be found geometrically [30,31], where the mass of a theoretical solid wick and the mass of the porous wick are

compared, or using Archimedes' principle [29,31,32], which uses the mass of the wick while it is suspended in water to calculate its volume. The porosity can also be calculated using a porosimeter [33]. To measure the average pore radius, a mercury porosimeter [30,32,33] or a bubble point test [4,5] can be used. The latter involves applying increasing gas pressure to one side of a saturated sample until a bubble appears on the other side and then using the Darcy equation to calculate the maximum pore radius. A schematic of the apparatus for the bubble point test is shown in Figure 1-12. Another method of measuring the average pore size is using a Scanning Electron Microscope (SEM) [29,31]. A cross section of the wick is scanned in a SEM, which shows the porous microstructure of the wick. A SEM image of the microstructure of a loose powder sintered nickel wick produced by Xin *et al*. [29] is shown in Figure 1-13.

Fig.1-12. Schematic of bubble point test [4]

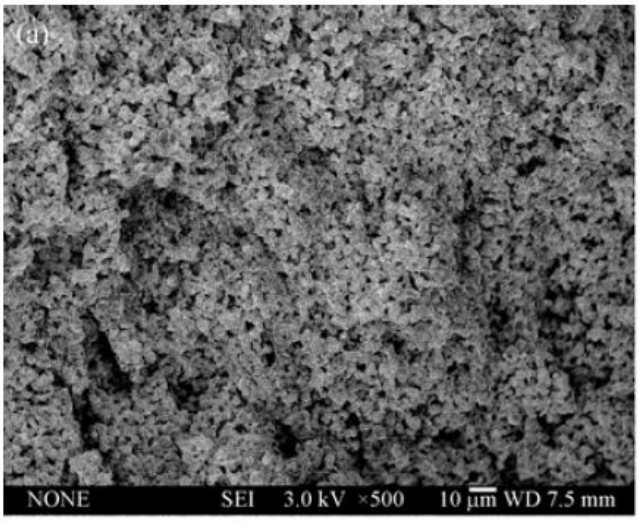

Fig.1-13. SEM image of loose powder sintered nickel wick [29]

By applying image processing and statistical analysis software, the average pore radius can be measured directly. Permeability can be determined experimentally by pumping fluid through a

sample, and using the mass flow rate and pressure difference between the inlet and outlet of the sample in the Darcy equation to calculate the permeabilty [4,5,32]. Empirical equations exist which allow the permeability to be calculated from porosity and pore diameter [23] or particle diameter [29]. Thermal conductivity can also be found empirically or analytically. The thermal conductivity of the wick can be measured by taking a sample and applying a known heat load on one face and measuring the temperatures difference across the sample [4,5]. The apparatus for this is shown in Figure 1-14.

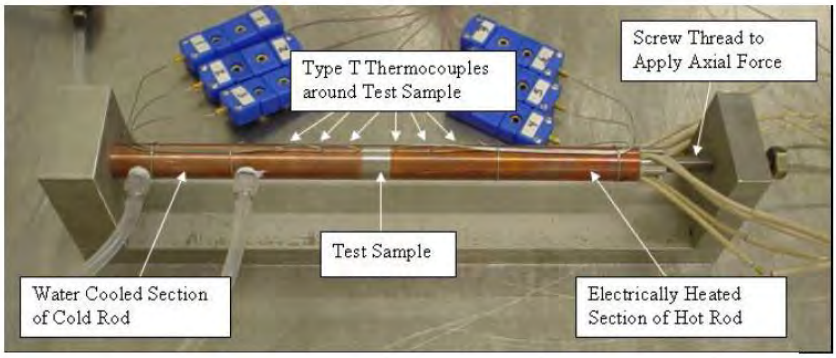

Fig.1-14. Thermal conductivity test apparatus [4]

Equations are also used to calculate the thermal conductivity of the wick using the thermal conductivity of the sintering material and working fluid [21,23].

1.8. Summary

This research aims to model a terrestrial LHP using a simple, one-dimensional mathematical model. Based on preceding literature, the model will analyse each component of the LHP separately, with special attention paid to the evaporator and condenser submodels as these evidently require attention. To validate the model, a LHP typically used in terrestrial applications requires construction. Due to their popularity, a cylindrical evaporator with a bayonet and integrated CC should be used. Due to the lack of information on secondary wick manufacture [3] and their uncommon use in terrestrial LHPs, only a primary wick should be employed which must be sintered using the available methods. A suitable working fluid should be selected for the temperature range, which will be between 20°C and 60°C. The condenser, in keeping with terrestrial applications but being aware of the experimental nature of the device, can be either air- or water-cooled to temperatures between 0°C and 40°C. Once the LHP is constructed and operational, further testing of the LHP in scenarios such as variation of elevation, tilt or heat sink temperature, is commonly performed. A series of experiments to test some of these scenarios should be performed.

2. MATHEMATICAL MODEL

2.1. Introduction

A theoretical heat transfer model was developed to aid in the design and performance assessment of the LHP conducted in this study. Due to the large amount of literature available [21,23,25,36,37], a steady-state mathematical model was pursued. Transient modeling, while a valuable and interesting focus of research, was beyond the scope of the current work which looked towards an introductory understanding of LHP operation. The model takes a one-dimensional approach which simplifies the mathematics and is sufficient to predict the performance of an LHP used in terrestrial electronics thermal management.

The LHP is divided into seven sections: 1) the evaporator and CC together, 2) the vapour grooves, 3) the vapour line, 4) the superheated portion of the condenser, 5) the two-phase portion of the condenser, 6) the subcooled portion of the condenser; and 7) the liquid line. The model deals with each section individually and sequentially, with the thermophysical properties of the fluid in transit at the exit of one section being used at the input values for the subsequent section. Most of the mathematics has been developed from the work of Bai *et al*. [23] as their model was recent enough to incorporate preceding innovations in LHP theory and promised accurate results. For sections of the LHP, such as the transport lines, the mathematics describing the changes the fluid undergoes is uncontroversial and agreed upon by Bai *et al.* and others [21,23,25]. The other sections of the LHP, notably the evaporator, CC and two-phase portion of the condenser, are not as well understood and potential models have been created to simulate them [23,25].

There are two primary differences between the model presented here and that proposed by Bai *et al*. [23]. Firstly, the evaporator and CC analysis require that experimental data be used to solve for certain thermal conductances. To reduce the dependency on experimental data whilst retaining the simplicity of the model, the evaporator and CC sections are altered to partially relieve the model of the need for this data. Secondly, the analysis of the condenser requires the simultaneous solution of four equations. To reduce the computational requirements of this numerical model, a void fraction correlation proposed by Wallis [38] is utilised. Gravitational components of the pressure drop through the liquid and vapour lines are also included, allowing the system to be analysed at gravity-assisted and gravity-adverse orientations. The mathematics for each section of the steady-state, one-dimensional LHP is given below.

2.2. Evaporator and compensation chamber

The evaporator consists of the heat source, saddle, evaporator envelope and the wick. The CC is a hollow section of tubing connected to the evaporator which stores excess fluid as the mass distribution in the LHP changes. The evaporator and CC are analysed together because of their highly interdependent thermal and hydraulic nature, particularly if the CC is integrated with the evaporator and they share a common envelope. Their analysis is performed by creating a nodal network analogous to the temperature and heat transfers present, illustrated in Figure 2-1.

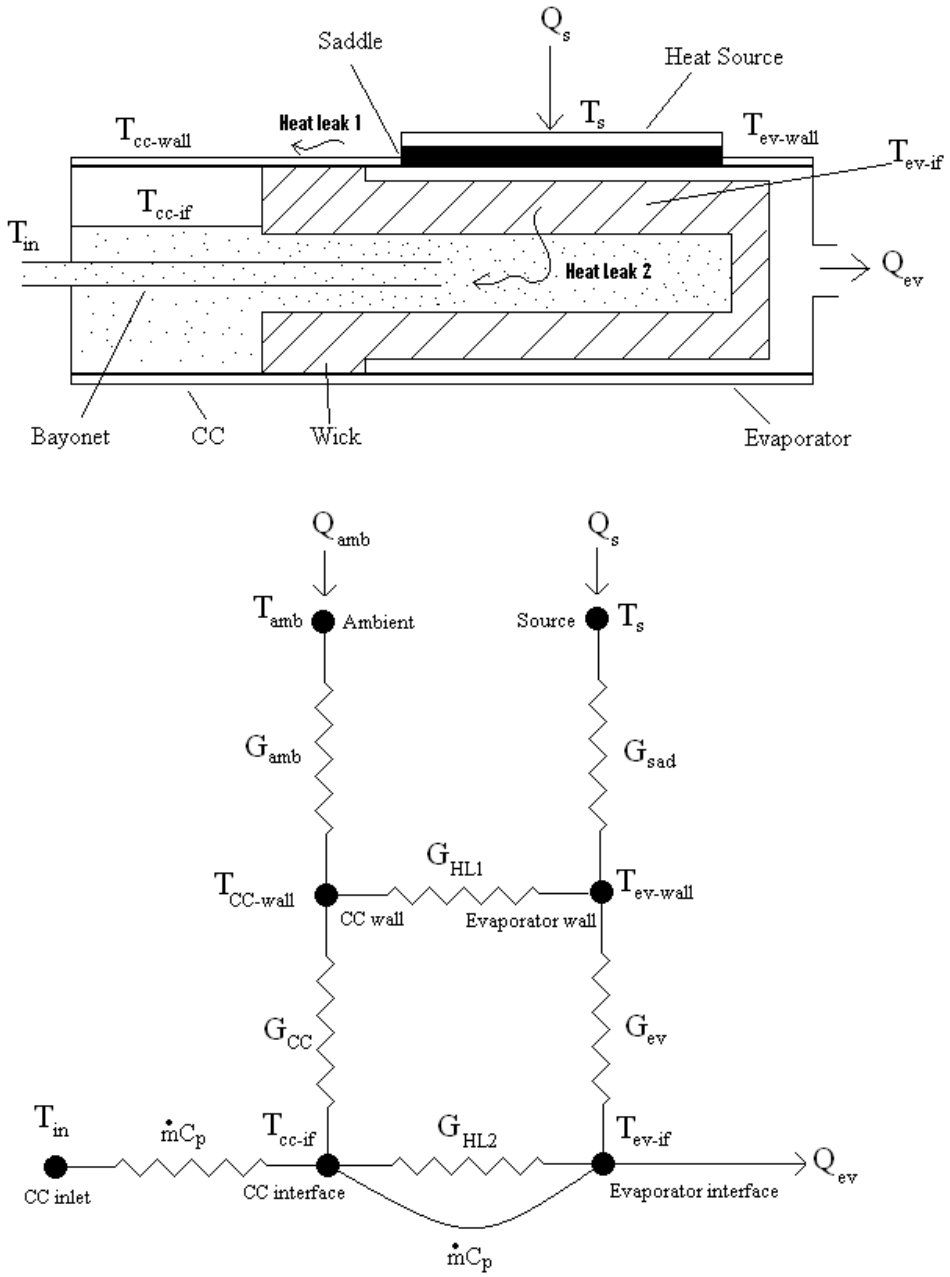

Fig.2-1. Evaporator and compensation chamber nodal network adapted from [23]

2.2.1. Evaporator

The analysis of the evaporator begins with a heat transfer from the heat source, which is at a steady-state temperature of T_S and produces heat Q_S, to the outer wall of the evaporator. Heat is conducted through the saddle connecting the source to the evaporator wall and Fourier's Law of Thermal Conduction is used to calculate its thermal conductance, G_{sad}.

$$Q_s = G_{sad}(T_s - T_{ev-wall}) \tag{2}$$

This is used to determine the value of $T_{ev\text{-}wall}$ from the input heat, the selected source temperature and calculated saddle conductance.

The heat entering the evaporator wall is split along two paths. The majority of the heat is transferred to the liquid/vapour interface of the pores in the outer surface of the wick whilst a portion is transferred as a heat leak between the evaporator wall and the CC wall. This energy balance is given as:

$$Q_s = Q_{ev-if} + Q_{HL1} \tag{3}$$

Due to the evaporator wall being in thermal contact with the CC wall, often by virtue of the fact that they are different portions of the same envelope, some of the input heat is transferred as a conductive heat leak. The thermal conductance along this path, G_{HL1}, can be found using Fourier's Law of Thermal Conductance through the tubing between them. Bai *et al.* [23] suggest using a path length equal to the wick length added to half the length of the CC. The general equation for the heat leak is then:

$$Q_{HL1} = G_{HL1}\left(T_{ev-if} - T_{cc-wall}\right) \tag{4}$$

where the temperature of the evaporator wall and the thermal conductance are determinable. To calculate the heat leak, the temperature of the CC wall must first be known. At this point in the analysis, the CC wall temperature cannot be determined and its value is assumed as an input. This assumption will be addressed in Section 2.7. The CC wall temperature will be assumed lower than that of the evaporator, and thus the evaporator wall temperature represents an upper limit as expressed as the following inequality, which must be upheld as the solution progresses:

$$T_{cc-wall} < T_{ev-wall} \tag{5}$$

The remaining heat, $Q_{ev\text{-}if}$, is transferred to the liquid-vapour interface on the outer surface of the wick through a fairly complex path. The general relation between the evaporator wall and the fluid interface in the wick is given as:

$$Q_{ev-if} = G_{ev}\left(T_{ev-wall} - T_{ev-if}\right) \tag{6}$$

The evaporator wall is thermally connected to the fluid interface on the surface of the wick by both the convective heat transfer of the vapour in the vapour grooves and by conductive heat transfer through the areas of the wick in contact with the evaporator wall. There are a number of factors which influence the thermal conductance G_{ev}, such as the nature of the thermal contact between the wick and evaporator wall and the geometry of the wick and vapour grooves. Experimental measurements of the evaporator wall and vapour line inlet temperatures are required to calculate this thermal conductance in lieu of an accurate analytical calculation.

This compromises the purely theoretical nature of the mathematical model but is permissible. Because heat is transferred in parallel between the wick and vapour, the convective resistance of the vapour can be ignored due to the much greater conductivity of the metallic wick. Since the dimensions of the wick and the thermal contact between the evaporator wall and wick are constant for all heat loads, the thermal conductance need only be found once experimentally and then applied for all subsequent modeling simulations. The value of $Q_{ev\text{-}if}$ is calculated by solving Eq. (3) after calculating the heat leak Q_{HL1} and the saturation temperature of the fluid interface, $T_{ev\text{-}if}$, can be determined from Eq. (6).

At the fluid interface on the outer surface of the wick, there is another division of heat. The interface on the outer surface of the wick and the fluid in the CC are thermally coupled through the liquid in the wick, the wick itself and the fluid in the CC. A portion of $Q_{ev\text{-}if}$ is transferred to the two-phase interface in the CC whilst the remainder of the heat is used to evaporate the liquid on the outer surface of the wick. This split is given as:

$$Q_{ev-if} = Q_{ev} + Q_{HL2} \tag{7}$$

where the heat leak is expressed as:

$$Q_{HL2} = G_{HL2}\left(T_{ev-if} - T_{cc-if}\right) \tag{8}$$

Concerning the heat leak, heat is transferred through the wick from the outer surface to the wick core through the metallic structure of the wick and liquid in the pores. Additional heat, transferring in parallel with that through the wick, is used to raise the temperature of the incoming fluid from the CC to that of the evaporating vapour. Finally, because of the saturated fluid in the CC, the heat leak is transmitted to the two-phase interface in the CC through an evaporation/condensation heat transfer, similar to a conventional heat pipe. The value of the conductance G_{HL2}, which is the summation of all these paths, is the subject of some debate.

Kaya *et al.* [21] suggests that the thermal conductance of the wick is found by considering the wick as a normal cylinder with a thermal conductivity calculated separately. These equations are:

$$G_{wi} = \frac{2\pi k_{eff} L_{wi}}{\ln \frac{d_o}{d_i}} \tag{9}$$

where d_o and d_i are the outer and inner diameters of the wick respectively and the effective thermal conductivity of the wick, k_{eff}, is given by Dunn and Reay and reported by Kaya *et al.* [21] as:

$$k_{eff} = k_{wick}\left(\frac{2 + \left(\frac{k_l}{k_{wick}}\right) - 2\varepsilon\left(1 - \left(\frac{k_l}{k_{wick}}\right)\right)}{2 + \left(\frac{k_l}{k_{wick}}\right) + \varepsilon\left(1 - \left(\frac{k_l}{k_{wick}}\right)\right)}\right) \tag{10}$$

Bai *et al.* [23] use the Navier-Stokes equations to analyse the temperature distribution through the wick in a purely radial direction and integrating between the inner and outer radius of the wick, produce the following equation:

$$G_{wi} = \frac{\dot{m} C_{pl}}{\left(\frac{d_o}{d_i}\right)^{\eta} - 1} \tag{11}$$

where the exponent η is:

$$\eta = \frac{\dot{m} C_{pl}}{2\pi k_{eff} L_{wi}} \tag{12}$$

The equation proposed by Chaudary and Bhandari and reported by Bai *et al.* [23] is used to determine the effective thermal conductivity.

$$k_{eff} = (k_{max})^n \times (k_{min})^{1-n} \tag{13}$$

The exponent *n* in Eq. (13) is a constant that can vary between 0.42 and 0.5. Bai *et al*. [23] point to a value of 0.42 which gives the best comparison to data. The two values k_{max} and k_{min} refer to the parallel (Q_{xy}) and serial (Q_{uw}) thermal conduction paths respectively. They in turn are determined by the following equations:

$$k_{max} = \varepsilon \times k_f + (1 - \varepsilon) \times k_{wick} \tag{14}$$

$$k_{min} = \frac{k_f k_{wick}}{\varepsilon k_{wick} + (1 - \varepsilon) \times k_f} \tag{15}$$

Eqs. (11-15) are adopted in this model due to their greater sophistication.

The heat used to raise the temperature of the incoming liquid is given as:

$$Q_f = G_f\left(T_{ev-if} - T_{cc-if}\right) \tag{16}$$

and the thermal conductance is simply:

$$G_f = \dot{m} C_{pl} \tag{17}$$

The final thermal conductance for Q_{HL2} is associated with the two-phase heat transfer in the saturated CC fluid. This is difficult to determine and conventional methods usually involve the use of advanced modeling software [26]. However, with the use of a bayonet to cool the inner surface of the wick core, the importance of the two-phase heat transfer is reduced and is considered negligible in this model.

Because the heat transfers being considered are only in the wick, are in parallel and are considered across the same temperature difference, the thermal conductance of the second heat leak can be found by the summation of Eq. (11) and Eq. (17) and the heat leak given as:

$$Q_{HL2} = \left(\frac{\dot{m} C_{pl}}{\left(\frac{d_o}{d_i}\right)^{\eta} - 1} + \dot{m} C_{pl} \right) \left(T_{ev-if} - T_{cc-if} \right) \tag{18}$$

where the exponent η is defined in Eq. (12).

The remainder of the heat transferred into the liquid/vapour interface is used to boil the liquid on the surface of the wick. This is expressed as:

$$Q_{ev} = \dot{m} h_{fg} \tag{19}$$

Eq. (7), Eq. (18) and Eq. (19) show that the calculations for the second heat leak, $Q_{HL2,}$ and the heat of evaporation, Q_{ev}, are interdependent and require additional information. For instance, Q_{ev} can be solved using Eq. (7) if the heat leak is known. This, however, requires that the mass flow rate be known so that the thermal conductance G_{HL2} can be calculated, and the mass flow rate can only be calculated using Eq. (19) if the heat of evaporation is known. Additionally, the heat and thermal conductance associated with the heat leak require that the temperature of the CC be known.

The model approaches this dilemma by assuming two values as inputs: the second heat leak and the CC temperature. With these assumptions, the energy of evaporation is calculated using Eq. (7), which allows the mass flow rate to be determined from Eq. (19). The actual heat leak for the particular set of assumed values can then be calculated using Eq. (18). The model compares the assumed Q_{HL2} value to the calculated value, corrects the error, and, after a number of iterations, the accurate heat leak for the selected CC temperature is determined. It is not possible at this point to deduce the CC temperature and its value must be assumed. There is an upper limit on the assumed CC temperature as the fluid in the CC is never at a higher temperature than the CC wall. Thus:

$$T_{cc-if} < T_{cc-wall} \tag{20}$$

2.2.2. Compensation chamber

The analysis of the CC begins with the heat transferred between the CC wall and the ambient environment, Q_{amb}, given as:

$$Q_{amb} = G_{amb}(T_{amb} - T_{cc-wall}) \tag{21}$$

Since this model is of a terrestrial LHP in an open environment, the heat transfer mechanism between the CC wall and ambient is natural convection and the conductance coefficient G_{amb} is expressed as:

$$G_{amb} = 1.32\pi L_{cc} d_o \left(\frac{T_{amb} - T_{cc-wall}}{d_o}\right)^{0.25} \tag{22}$$

Q_{amb} can be calculated since the temperature of the ambient environment is known and the temperature of the CC wall has been assumed. The model assumes that the ambient environment heats the CC wall, therefore the ambient temperature is prescribed as greater than the CC wall temperature. This is only the case at certain heat loads and the temperature of the CC wall will eventually become greater than the ambient. In this event, the temperatures in Eq. (22) switch and heat flows to the surrounding environment.

There is a summation of heat transfers at the CC wall as ambient heating and the heat leak between the CC wall and the evaporator wall are both transferred to the fluid in the CC. There is the possibility of a third heat transfer, Q_{add}, as some LHPs have a heater or cooler attached to the CC wall [3]. By adding a cooler, such as a thermosyphon, the operating temperatures of the LHP at steady-state can be reduced, resulting in greater efficiency. A heater effectively primes the LHP, analogous to priming heaters in a CPL [7], allowing for a more stable start-up and reducing the time required to reach steady-state. Heaters can also be used to stall the LHP if their heat input is sufficiently great. The summation of heat transfers is given as:

$$Q_{cc} = Q_{amb} + Q_{HL1} + Q_{add} \tag{23}$$

This model is intended to simulate the behaviour of an LHP without additional heat transfer devices on the CC, and the value of Q_{add} is zero.

The heat entering the CC is then found using Eq. (23). The heat transfer between the CC wall and the fluid is given as:

$$Q_{cc} = G_{cc}\left(T_{cc-wall} - T_{cc-if}\right) \tag{24}$$

This thermal conductance is too complex to be accurately modelled mathematically. This is due to a number of factors such as the movement of the fluid in the CC, the different thermal

resistances of the liquid and vapour phases present and the shifting void fraction and orientation of the interface as the LHP is elevated or tilted. There is also the consideration that the LHP operates under two modes. At low heat inputs, the two-phase region in the condenser is relatively short, resulting in there being more liquid in the outer loop and a void fraction in the CC. As a result of the void, both liquid and vapour are present and the CC interface temperature is at saturation. While a void exists in the CC, the LHP is said to operate in variable conduction mode as there is a decrease in operating temperatures during this period proportional to the decrease in void fraction. Once the void fraction reaches zero, the LHP enters into its constant conductance mode, where the operating temperatures increase as the heat input increases. The pure liquid in the CC is at a lower temperature than its saturation temperature. The CC can therefore contain a void with the fluid at saturation or it can be flooded with subcooled liquid, making it difficult to obtain an accurate value for the thermal conductance.

The thermal conductance G_{CC} is usually found empirically with the temperature of the fluid at the CC inlet, CC wall and evaporator wall [21,23,25]. This approach, however, relies on experimental data. Unlike the empirical determination of G_{ev}, which was agreeable because it is independent of heat load, the estimation of the CC thermal conductance would have to be generated for every scenario of operation. This is unacceptable and the method by which the model bypasses the need to calculate G_{CC} will be discussed in Section 2.7. The calculation of G_{CC} is not an immediate requirement, however, as the temperature of the CC fluid interface, which can be calculated using Eq. (24) if the thermal conductance is known, is already assumed from the calculation of the second heat leak.

For steady-state operation, the heat from the CC wall and the heat leak through the wick are combined to heat the subcooled liquid from the CC inlet. This is given as:

$$Q_{in} = Q_{cc} + Q_{HL2} \tag{25}$$

The general equation for the heating of the subcooled liquid is given as:

$$Q_{in} = \dot{m} C_{pl} \left(T_{cc-if} - T_{in} \right) \tag{26}$$

Eq. (26) requires that the inlet temperature be assumed to determine the heat capacity of the liquid. By assuming the temperature of the CC inlet, the heat required to raise the temperature of the subcooled inlet liquid to the temperature of the CC fluid interface can be calculated and compared to the value determined using Eq. (25). This energy balance is used in the model solution discussed in Section 2.7.

The assumed temperature of the CC inlet liquid is constrained by upper and lower limits. The CC fluid heats up the subcooled inlet fluid and thus the inlet temperature can never be greater

than the CC fluid interface temperature. The liquid entering the CC has been transported from the subcooled portion of the condenser where it reached a minimum temperature equal to the heat sink temperature. The temperature of the CC inlet fluid is then never lower than the condenser temperature. These limits are expressed as:

$$T_{cc-if} > T_{in} > T_{cond} \tag{27}$$

Combining all the inequalities associated with the assumed variables produces the following inequality which must hold when the assumed variables are selected.

$$T_{ev-wall} > T_{cc-wall} > T_{cc-if} > T_{in} > T_{cond} \tag{28}$$

Not included in this inequality is that the assumed heat leak must be positive.

This completes the mathematical model of the CC and evaporator. By using three assumed temperatures and the second heat leak, the temperatures and heat transfers through every part of the thermal nodal network can be found and, consequently, the energy balance over the CC determined.

2.3. Vapour grooves

The vapour formed on the outer surface of the wick is transported to the evaporator outlet through channels machined into the wick or evaporator wall. Vapour is formed along the length of the grooves and despite there being contact with the wall, the model assumes zero heat transfer, that is, the temperature of the vapour, $T_{ev\text{-}if}$, remains constant. This assumption is considered due to the low conductivity of the vapour and its quick passage through the grooves. The vapour becomes superheated as there is a drop in pressure through the grooves, given as:

$$\frac{dP_{vg}}{dx} = -f\frac{\rho v^2}{2d_{vg}} \tag{29}$$

where the hydraulic diameter of a square vapour groove is given as:

$$d_{vg} = \frac{2tw}{t+w} \tag{30}$$

The mass flow rate increases along the length of the grooves as more liquid from the wick cavity is drawn through the wick and evaporated at the fluid interface further back in the grooves. This culminates in the maximum mass flow rate at the vapour groove exit, which is calculated using Eq. (19). There is no simple method to determine the increase in mass flow rate per unit length in the vapour grooves. Bai *et al*. [23] solve this by assuming the mass flow rate increases linearly, which is a fair assumption if the vapour grooves have a consistent surface and are heated uniformly. The mass flow rate and vapour velocity can then be considered to be

constant and at their maximum for half the length of the vapour grooves, simplifying Eq. (29). The velocity, in terms of mass flow rate, is given as:

$$v_{vg} = \frac{\dot{m}}{ntw\rho_v} \tag{31}$$

The pressure drop is calculated in a single step since the velocity of the vapour is assumed constant along the length of the grooves. Eq. (29) is rewritten by substituting in Eq. (30) and Eq. (31) and the pressure drop over the length of the vapour grooves is given as:

$$dP_{vg} = -f\frac{L_{vg}(t+w)\dot{m}^2}{4n^2t^3w^3\rho_v} \tag{32}$$

Realistically, the pressure drop in each groove may not be equal as the vapour temperature will differ. In a cylindrical evaporator, the grooves positioned on the side away from the heat source may receive less heat, resulting in a lower mass flow rate and consequentially a lower pressure drop. In this event, the pressure drop equation Eq. (32) would require the n^2 variable be removed and the pressure drop calculated separately for each groove, or Eq. (32) would need to be amended with a coefficient to reflect these differences in the vapour grooves. However, if the wick has azimuthally positioned grooves, the vapour pressure and mass flow rate can be assumed equal because the vapour is distributed evenly. Eq. (32) can then be used without loss of accuracy.

The coefficient of friction, *f*, depends on whether the flow is turbulent or laminar, as determined by the Reynolds number and is calculated from the Poiseuille and Blasius correlations. For Moody frictional coefficients, these are:

$$f = \frac{64}{\mathrm{Re}} \quad \text{for Re} < 2200 \quad \text{Laminar Flow} \tag{33}$$

$$f = 0.3164\mathrm{Re}^{-0.25} \quad \text{for Re} > 2200 \quad \text{Turbulent Flow} \tag{34}$$

where the Reynolds number, Re, is given by:

$$\mathrm{Re} = \frac{\rho_v v_{vg} d_{vg}}{\mu_v} = \frac{4\dot{m}}{d_{vg}\mu_v\pi} \tag{35}$$

The pressure at the vapour groove outlet is obtained by using the saturation pressure of the vapour from the evaporation temperature, $T_{ev\text{-}if}$, as the initial pressure and subtracting the pressure drop given by Eq. (32).

2.4. Vapour and liquid lines

The transport lines are considered together because they are essentially the same with only the phase of the fluid and the direction of ambient heat transfer being significant differences. The

equations defined here therefore apply to both transport lines and are adapted from the model of Bai *et al*. [23].

2.4.1. Temperature change

The temperature change of the fluid is due to thermal contact with the surrounding terrestrial atmosphere. For the modeling of an aerospace LHP this can be neglected as greater insulation would be applied to prevent heat creep, or a radiation heat transfer can be considered instead. This model ignores thermal creep along the pipe to simplify the mathematics but is a fair assumption for low thermal conductivity piping materials such as stainless steel. The general equation for the heat transfer, assuming that heat is rejected from the fluid, is:

$$\frac{dQ_f}{dx} = \left(\frac{UA}{L}\right)\left(T_f - T_{amb}\right) \tag{36}$$

where the thermal resistance is given by the sum of the resistances between them:

$$\frac{L}{UA} = \frac{1}{h_i d_i \pi} + \frac{\ln(d_o/d_i)}{2\pi k_{wall}} + \frac{\ln(d_o/d_i)}{2\pi k_{insulation}} + \frac{1}{h_o d_o \pi} \tag{37}$$

Inside the transport lines, the fluid creates a convective thermal resistance characterised by the coefficient of heat transfer, h_i, as follows:

$$h_i = \frac{(\mathrm{Nu})k_f}{d_i} \tag{38}$$

The Nusselt number, Nu, requires the nature of the flow be determined. The fluid in both the vapour and liquid line is considered to be fully developed and steady. The fully-developed consideration is due to the high length to diameter ratio of the tubing. The nature of the flow can be found using the Reynolds number calculated using Eq. (35). For laminar flow:

$$\mathrm{Nu} = 4.36 \text{ for constant heat flux} \tag{39}$$

$$\mathrm{Nu} = 3.66 \text{ for constant temperature} \tag{40}$$

When the flow is turbulent, the Nusselt number is given by the Dittus-Boelter correlation:

$$\mathrm{Nu} = 0.023\mathrm{Re}^{0.8}\mathrm{Pr}^{\mathrm{n}} \tag{41}$$

Where the exponent, n, is 0.4 when the fluid in being heated and 0.3 when the fluid is being cooled. The Prandtl number, Pr, is found using the following equation.

$$\mathrm{Pr} = \frac{C_p \mu}{k} \tag{42}$$

The convective coefficient for the fluid can be calculated using Eq. (38) and these formulas. As the transport lines are calculated in incremental steps, the values of the physical properties in the

above equations are found from the pressure and temperature of the preceding element where the temperature and pressure are known.

The wall and insulation thermal resistances are given by Fourier's Law of Thermal Conduction through a cylinder. Insulation is not mandatory but can significantly improve the performance of the LHP. If insulation is applied to the liquid line but not the vapour line, the outer loop can be made to reject greater amounts of heat whilst minimising heat absorption, producing better performance and overall thermal conductance. Insulation is application sensitive and it is included in the model for the sake of completion. In this study no insulation was applied to either transport line.

The coefficient of heat transfer provided by natural convection on the outside of the pipe or insulation is expressed as:

$$h_o = 1.32\left(\frac{T_o - T_{amb}}{d_o}\right)^{0.25} \tag{43}$$

where T_o and d_o are the temperature and diameter of the outer surface of the pipe.

The heat transferred between the environment and the fluid results in a temperature change in the fluid, expressed for heat rejection from the transport line as:

$$\frac{dQ_f}{dx} = -\dot{m}C_p\frac{dT_f}{dx} \tag{44}$$

Combining Eq. (36) and Eq. (44) and solving for the change in temperature over a unit length produces the following formula which allows the change in fluid temperature to be calculated incrementally:

$$\frac{dT_f}{dx} = -\frac{1}{\dot{m}C_p}\left(\frac{UA}{L}\right)\left(T_f - T_{amb}\right) \tag{45}$$

2.4.2. Pressure drop

The pressure drop in the transport lines due to both friction and gravity is given as:

$$\frac{dP_f}{dx} = -f\frac{\rho_f {v_f}^2}{2d_i} \pm \mathrm{g}\rho_f \sin\varphi = -f\frac{8\dot{m}^2}{\rho_f \pi^2 {d_i}^5} \pm \mathrm{g}\rho_f \sin\varphi \tag{46}$$

The frictional coefficient is found by determining the Reynolds Number using Eq. (35) and Eq. (33) or Eq. (34). The second term is the gravitational pressure change which develops when the condenser is elevated or lowered relative to the evaporator. The convention used in this model is that a positive angle θ is used when the condenser is elevated above the evaporator and the

flow is gravitationally assisted. Eq. (46) is altered to reflect gravity for each line: the sign before the gravitational term is positive for the liquid line and negative for the vapour line.

The model calculates the temperature and pressure of the fluid by dividing the transport lines into discrete increments, *dx*, and determining the change in these qualities per increment over the length of the transport lines.

2.5. Condenser

The condenser is considered as three separate regions: the superheated region which accepts vapour from the end of the vapour line and removes its sensible heat; the two-phase region where the vapour changes into liquid; and the subcooled region which decreases the temperature of the liquid further.

2.5.1. Superheated and subcooled regions

The superheated and subcooled regions are modelled using the same mathematics as the transport lines because they are largely the same with a few exceptions. Because they are thermally attached to the heat exchanger, the external temperature is the heat sink temperature and the thermal resistance of the heat exchanger must be used instead of a natural convective thermal resistance. The temperature change in the subcooled and superheated regions is found using Eq. (45) but the total thermal resistance is found as follows:

$$\frac{L}{UA} = \frac{1}{h_i d_i \pi} + \frac{\ln(d_o/d_i)}{2\pi k_{wall}} + R_{heat\ sink} \tag{47}$$

The experimental LHP has the condenser installed in a water jacket through which low temperature water is pumped, counter to the flow of fluid in the condenser. The pressure drops through the superheated and subcooled regions are calculated using Eq. (46) but because gravitational effects in the condenser are ignored, this term may be deleted.

2.5.2. Two-phase region

The two-phase region assumes an annular pattern, where the condensing liquid phase accumulates on the walls of the tubing while the pure vapour phase remains in the central stream. This is reasonable because the mass flow rate is relatively low and annular phase distributions are commonly made when analysing small-to-capillary diameter pipe flow. The analysis of the two-phase region is adapted from the Bai *et al*. [23] model and required four variables to be determined: the vapour quality, X; the film thickness, δ; the vapour pressure, P_v; and the liquid pressure, P_l. The change over a spatial increment dx for each of these is

discussed. A schematic of a section of the two-phase region emphasising the annular flow is shown in Figure 2-2.

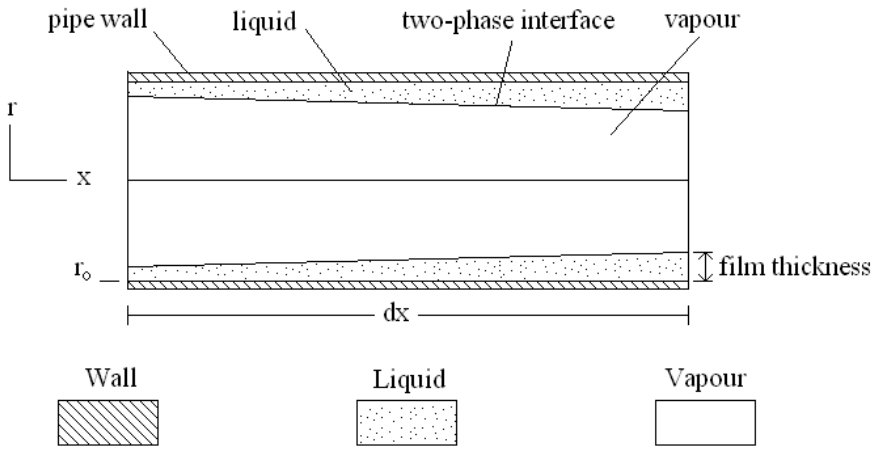

Fig.2-2. Annular flow in the two-phase region adapted from [23]

2.5.2.1. Vapour quality

The vapour quality is the ratio of the vapour mass over the total mass. In pipe flow, this ratio is expressed using mass flow rate and is given as:

$$X = \frac{\dot{m}_v}{\dot{m}} \tag{48}$$

Differentiating Eq. (48) by *dx* gives:

$$\frac{dX}{dx} = \frac{1}{\dot{m}} \frac{d\dot{m}_v}{dx} \tag{49}$$

The change in vapour quality is due to the condensation of the fluid as heat is rejected. Since a phase change occurs, this heat rejection can be found using Eq. (19). The change in mass flow rate of vapour can be found by differentiating Eq. (19) with respect to *dx*:

$$\frac{dQ_{cond}}{dx} = \frac{d\dot{m}_v}{dx} h_{fg} \tag{50}$$

Substituting Eq. (49) into Eq. (50) produces:

$$\frac{dQ_{cond}}{dx} = \frac{dX}{dx} \dot{m} h_{fg} \tag{51}$$

Eq. (36) gives the heat rejected as a function of the temperature difference between the fluid and heat sink. Combining Eq. (36) and Eq. (51) and solving for the change in vapour quality over *dx* produces:

$$\frac{dX}{dx} = -\frac{1}{\dot{m}h_{fg}}\left(\frac{UA}{L}\right)(T_v - T_{cond}) \tag{52}$$

The thermal resistance is given by Eq. (47). The first convective term is the thermal resistance offered by the liquid film and its coefficient of heat transfer can be found Eq. (38). The hydraulic diameter of the liquid film required for this calculation is given by:

$$d_i = 4\delta - \frac{2\delta^2}{r_i} \tag{53}$$

The Reynolds number is found using Eq. (35), where the mass flow rate is that of the liquid, found by multiplying the total mass flow rate by the liquid quality (1-*X*).

The change in vapour quality is dependent on the vapour pressure for determining the temperature and properties of the vapour at saturation, the liquid pressure for calculating the internal convective thermal resistance, and the film thickness, for determining the hydraulic diameter.

2.5.2.2. Film thickness

The interface between the vapour and liquid in the two-phase region is curved due to differences in pressure and the surface tension of the liquid. This balance of forces is given by the Young-Laplace equation:

$$P_v - P_l = \sigma\left(\frac{1}{R_{radial}} - \frac{1}{R_{axial}}\right) \tag{54}$$

The R_{radial} and R_{axial} terms are the radii of curvature in the radial and axial directions respectively. The inverse of the axial radius of curvature tends towards zero as the overall change in film thickness in the axial direction is only a few millimeters and occurs over a distance of a few meters. The radial curvature can be expresses as a function of the film thickness and the contact angle θ:

$$P_v - P_l = \sigma\left(\frac{\cos\theta}{r_i - \delta}\right) \tag{55}$$

The contact angle can be expressed as a function of the change in film thickness over *dx*. This is illustrated in Figure 2-3:

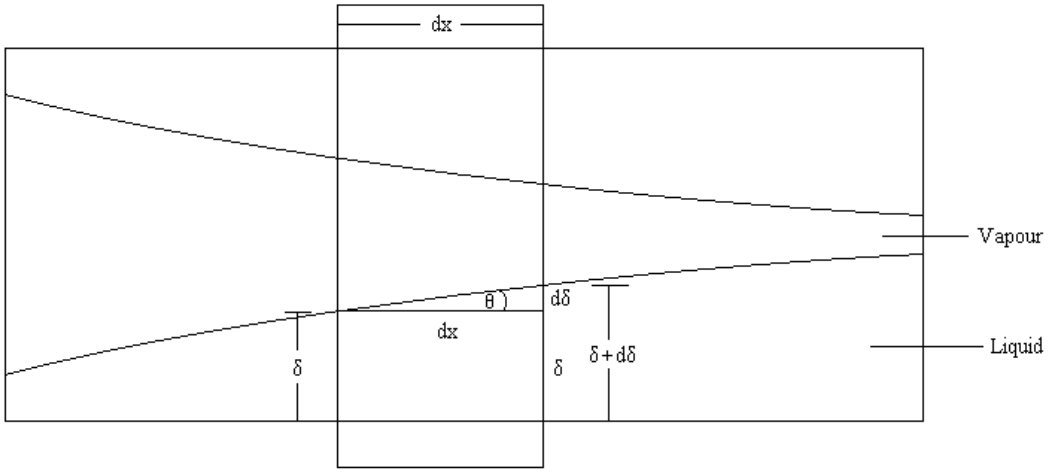

Fig.2-3. Correlation between contact angle and change in film thickness over *dx*

From Figure 2-3, if the spatial increment is small enough to assume a right angled triangle with sides *dx* and *dδ*, the change in film thickness over *dx* is expressed as:

$$\tan\theta = \frac{d\delta}{dx} \tag{56}$$

The contact angle is then solved as:

$$\theta = \arctan\frac{d\delta}{dx} \tag{57}$$

Substituting Eq. (57) into Eq. (55) and applying the relevant trigonometric identities produces:

$$P_v - P_l = \sigma\left(\frac{\cos\left(\arctan\frac{d\delta}{dx}\right)}{r_i - \delta}\right) = \frac{\sigma}{r_i - \delta}\left(1 + \left(\frac{d\delta}{dx}\right)^2\right)^{-0.5} \tag{58}$$

Given the pressure of the vapour and liquid and the film thickness at the beginning of the increment, Eq. (58) can be used to calculate the change in film thickness over the increment.

2.5.2.3. Vapour pressure

The vapour in the two-phase region undergoes a pressure drop due to three factors: a frictional shear stress caused by the vapour in contact with the liquid/vapour interface; a change in momentum as the vapour condenses, producing a retardant shear stress on the vapour; and a momentum transfer shear stress caused by the condensation of the vapour. The last stress is introduced by Bai *et al*. [23] and is employed in this model as it improves the simulation. The general equation for the pressure drop in the vapour region is given as:

$$\frac{dP_v}{dx} = -\frac{2}{r_i - \delta}\left(\tau_{fr} + \tau_{mt}\right) - \frac{d(\rho_v {v_v}^2)}{dx} \tag{59}$$

The frictional shear stress develops because the vapour and liquid travel at different velocities. Due to its turbulent flow, the vapour velocity is calculated as the average velocity, found through the mass flow rate equation. The liquid velocity at the interface is greater than the average liquid velocity because even though it is turbulent at the beginning of condensation, it quickly becomes laminar. In fully developed laminar flow, the maximum velocity at the outer surface of the liquid is approximately twice the average velocity. The frictional shear stress with these considerations is:

$$\tau_{fr} = \pm\frac{1}{8} f \rho_v (v_v - 2v_l)^2 \tag{60}$$

where both velocities are calculated as the average velocity of the phase. The variable sign at the beginning of the equation reflects the possibility that the velocity of the vapour may be less than the velocity of the liquid and should be negative when the liquid velocity is larger. The coefficient of friction is calculated by considering the vapour side of the interface and applying Eq. (33), Eq. (34) and Eq. (35).

The momentum-transfer shear stress proposed by Bai *et al.* [23] is also dependent on the difference between vapour and liquid velocities but multiplied by the change in vapour quality over *dx* and the heat rejected to the heat sink. It is given as:

$$\tau_{mt} = -\frac{dX}{dx}\frac{Q_{cond}}{2\pi h_{fg}(r_i - \delta)}(v_v - 2v_l) \tag{61}$$

The heat rejected to the heat sink is found by integrating Eq. (51) and substituting it into Eq. (61). The following simplified equation emerges:

$$\tau_{mt} = -\frac{dX}{dx}\frac{X\dot{m}}{2\pi(r_i - \delta)}(v_v - 2v_l) \tag{62}$$

The momentum term which follows the shear stress terms in Eq. (59) describes the force acting on the vapour as its momentum changes through condensation, which alters the density and velocity of the vapour over the spatial increment.

The calculation of the pressure drop in the vapour region is dependent on the film thickness, vapour quality, and vapour and liquid pressures.

2.5.2.4. Void fraction correlation

Calculating the change in vapour quality, film thickness or vapour pressure requires that all these variables and the liquid pressure be known first. There are only three equations available

to define four variables at the outlet of each increment, leaving the model incomplete as it stands.

An empirical void fraction correlation proposed by Wallis [38] is the completing equation that allows the film thickness to be determined from the pressure of the vapour and liquid and the vapour quality at a cross section of the condenser. The Wallis correlation is given as [38]:

$$\alpha = \frac{V_v}{V_{total}} = (1 + Xtt^{0.8})^{-0.378} \tag{63}$$

where *Xtt*, the Lockhart-Martinelli parameter, is given by:

$$Xtt = \left(\frac{1-X}{X}\right)^{0.9} \left(\frac{\rho_v}{\rho_l}\right)^{0.5} \left(\frac{\mu_l}{\mu_v}\right)^{0.1} \tag{64}$$

By interpreting the volume ratio as an area ratio across a negligible length, the following ratio is found:

$$\alpha = \frac{A_v}{A_{total}} = \frac{(r_i - \delta)^2}{{r_i}^2} \tag{65}$$

Solving for the film thickness:

$$\delta = r_i\left(1 - \sqrt{\alpha}\right) \tag{66}$$

2.5.2.5. Inlet variables and condenser solution

By using Eq. (52), Eq. (58), Eq. (59) and the void fraction correlation given in Eq. (63) and Eq. (66), the vapour quality, film thickness, vapour and liquid pressure at the end of a spatial increment can be calculated using the initial values. This is repeated for each subsequent spatial increment as is done for the transport and superheated/subcooled lines.

The first element requires initialisation values. The vapour quality cannot be specified as 1 because the void fraction correlation would be zero, resulting in a non-physical result. Rather, as the vapour temperature and pressure become saturated and begin to condense, it is expected that a minor fraction of vapour has already changed phase and thus the vapour quality at the onset of the two-phase region is no longer unity. The model assumes that the initial vapour quality is 0.9999. The vapour pressure is assumed to be the same as the pressure exiting the superheated region as the miniscule condensation presumed is negligible.

The liquid pressure cannot be assumed to be the same as the vapour pressure because this would imply that the change in film thickness is zero according to Eq. (58), which would cause the model to fail. However, the liquid pressure term only appears explicitly in Eq. (58), the equation itself being used to find the liquid pressure. Therefore, at the inlet, values for liquid

pressure, surface tension density and viscosity can be found through the following cycle: first, assume that the liquid pressure equals the vapour pressure, and take the properties of the liquid at this saturation pressure. Next, calculate the film thickness from the void fraction correlation. It is then assumed that the film thickness has grown from zero at the entrance and the change in the film thickness can be found as the film thickness divided by *dx*. By using Eq. (58) and the vapour pressure, the surface tension associated with the pressure of the liquid and the change in film thickness, the corrected liquid pressure can be calculated. This value is then substituted for the assumed pressure of the liquid and the process repeated until there is no change in liquid pressure between iterations. This value is the inlet liquid pressure and the inlet film thickness can then be calculated.

The solution of the two-phase region follows a similar pattern. With the key values known at the beginning of any spatial increment, their change is calculated over the increment and the outlet values are consequently found. The change in vapour quality over *dx* can be calculated from the entry values of the increment and Eq. (52), and the exit value found. The vapour pressure is similarly calculated from Eq. (59). With the liquid pressure and film thickness, the solution progresses into the same corrective loop as is employed in the initial increment and the correct liquid pressure and film thickness at the end of the increment are produced.

Since condensation occurs at constant temperature, the temperatures of the vapour and liquid at the entrance and throughout the two-phase region are the saturation temperatures corresponding with the vapour and liquid pressures. As the fluid exits the two-phase region, the temperature and pressure of the liquid phase becomes the initial pressure and temperature of the subcooled region. The two-phase region may take longer than the remainder of the condenser to fully condense and thus both liquid and vapour may enter the liquid line. There is also the possibility that vapour may begin condensing before the end of the vapour line. In both cases, the portion of the transport line in question is modelled with the two-phase flow considerations and equations above, with the thermal resistances and heat sink temperature changed to reflect the transport lines thermal contact with the ambient.

2.6. Mass equation

The solution to the model requires that the void fraction in the CC be known which requires that the fluid mass in the CC be known. This is achieved by the summation of fluid masses in the system subtracted from the total working fluid inventory.

$$M_{cc} = M_{ch} - M_{wi} - M_{vg} - M_{vl} - M_{cond} - M_{ll} \tag{67}$$

In order to calculate the void fraction and determine what mode of operation the LHP is in, the following equation is used.

$$\alpha = \frac{\rho_l V_{cc} - M_{cc}}{(\rho_l - \rho_v)V_{cc}} \tag{68}$$

The use of the void fraction in solving the model is discussed in Section 2.7.

A void fraction exists in the CC during low heat loads and decreases as the heat load increases until it becomes zero and the CC floods. Due to the CC no longer being able to store excess fluid from the outer loop when this occurs, there is a steady reduction in the length of the two-phase region of the condenser as the heat load increases. The LHP is in constant conductance mode as the restriction on the two-phase length necessitates greater operational temperatures.

It is often the case that the lowest operating temperatures and the best LHP performance occur when the CC has just been flooded and the LHP transitions between variable and constant conductance mode. The LHP can be designed to operate at maximum performance for a selected source heat by calculating the volume of the CC such that the void fraction will have just reached zero when the condenser is fully utilised. This is an important design consideration in certain applications, where spatial constraints on the evaporator and CC must be balanced against the performance of the LHP. The conventional method of determining the CC volume and working fluid inventory is given by Ku [1]. The following two mass distribution equations must be considered.

The void fraction in the CC is at its greatest when the entire loop outside the CC is flooded, typically during its coldest startup. The mass charge for this mass distribution is given as [1]:

$$M_{ch} = \rho_{l,c}\big(V_{loop} + (1-\alpha)V_{cc}\big) + \rho_{v,c}(\alpha V_{cc}) \tag{69}$$

where the densities are referenced at the coldest temperature the LHP will experience. The volume of the loop is the summation of the volume of every component in the LHP except the CC.

At the highest operating temperature, the vapour lines and condenser will be filled with vapour. The mass charge for this mass distribution is given as [1]:

$$M_{ch} = \rho_{l,h}(V_{ll} + V_{wi} + (1-\beta)V_{cc}) + \rho_{v,h}(V_{vl} + V_{cond} + \beta V_{cc}) \tag{70}$$

where the densities are referenced at the highest temperature experienced by the LHP. The α and β coefficients in Eq. (69) and Eq. (70) represent the void fraction that the designer of the LHP intends the CC to have during the cold and hot cases respectively. In practice, to avoid wick dry-out, there must always be sufficient liquid in the CC. This is pertinent during low power operation when the void fraction is at its greatest and it has been suggested that the void

fraction never be greater than 0.5 [6,8,23]. In the hot case, it is usual for the CC to be flooded, meaning that it is a fair assumption to consider the second void fraction to be 0. The mass charge can be calculated from either Eq. (69) or Eq. (70). The volume of the CC can be calculated by equating these equations.

The use of these equations has drawbacks concerning the accuracy of the mass distribution for each case. These equations do not reflect the variation in liquid and vapour densities throughout the system and instead considering the fluid to have a constant liquid and vapour density throughout the LHP. Eq. (70) considers the condenser to be filled with vapour but the condenser should always have a portion of its volume which contains pure liquid. Eq. (70) suffers the most from these errors while Eq. (69) is accurate enough to be used in calculating the mass charge.

Due to the mass distribution errors implicit in Eq. (70), the CC volume cannot accurately be calculated by equating Eq. (69) and Eq. (70). An accurate model of the LHP, however, could accurately determine the mass distribution in the high temperature case and therefore could be used to design the CC dimensions which satisfy both the mass distributions for the cold and hot cases. This further illustrates the use of the mathematical model as a tool of LHP design.

2.7. Model solution

The model is implemented in MATLAB and determines if the temperature of the heat source, T_s, for a given heat load, Q_s, is acceptable. The acceptability of the source temperature is defined with three criteria: an energy balance must exist in the CC; the void fraction in the CC must be acceptable; and the pressure drop in the system cannot be larger than the maximum capillary head which the wick can produce.

The existence of an energy balance in the CC is found by determining if the heat entering the CC through the CC wall and wick, given by Eq. (25), is equal to the heat needed to raise the temperature of the incoming subcooled liquid, given by Eq. (26). Before these heats can be compared, however, the four initial assumed values need to be corrected. These assumed values are: the second heat leak, Q_{HL2}; the temperature of the CC wall, $T_{cc\text{-}wall}$; the temperature of the CC fluid, $T_{cc\text{-}if}$; and the temperature of the CC inlet, T_{in}.

Once the four assumed variables have been selected, with the temperatures conforming to Eq. (28), the first variable which can be corrected is the second heat leak. As discussed in Section 2.2.1., the second heat leak can be corrected for an assumed CC wall and CC fluid temperature over a number of iterations. With the CC temperatures assumed and the correct heat leak determined, the mass flow rate and saturation temperature of the vapour in the vapour grooves can be calculated. These values, together with the mathematics given in the preceding sections,

provide the temperature and pressure drop through the vapour grooves, transport lines and condenser. This concludes with the temperature and pressure of the liquid entering the CC. The correct value of T_{in} is found by replacing the assumed CC inlet temperature with the temperature of the liquid leaving the liquid line and repeating the process for a number of iterations until there is no difference between the assumed and calculated T_{in} values.

The temperature of the CC fluid follows immediately once the temperature of the CC inlet is known. Apart from determining the temperature of the liquid line outlet, the model also produces the pressure of the liquid entering the CC. Since this model neglects the bayonet, there is no pressure difference between the CC fluid and liquid line outlet. Assuming that the CC fluid is saturated, the pressure at the liquid line outlet can be used to determine a corresponding saturation temperature. This is the temperature of the CC fluid, $T_{cc\text{-}if}$.

The temperature of the CC wall is usually found by first determining the thermal conductance between the CC wall and fluid empirically [23,25]. In an effort to reduce the dependency on experimental data, the model is configured such that this thermal conductance is not needed. This means that the model cannot explicitly determine the CC wall temperature, and the CC wall temperature therefore remains an assumed value. The model is able to provide a solution to the LHP, however, by generating two sets of operating temperatures for a given heat load: one set in which the CC wall temperature is slightly below the temperature of the evaporator wall; and a second set in which the CC wall temperature is slightly greater than the CC fluid temperature. These two CC wall temperatures represent the maximum range of possible temperatures which the CC wall temperature could have whilst maintaining Eq. (28). The two temperature sets give the range in which the experimental data can be expected to fall. By selecting either of these CC wall temperatures and making the initial assumptions required of the other assumed variables, the model can correct the heat leak, CC inlet and CC fluid temperatures and determine whether the source temperature under investigation produces the requisite energy balance in the CC. If it does not, the source temperature is changed and the process repeated. Once an acceptable source temperature is found, the other CC wall temperature is assumed and the entire process repeated.

If the temperature of the heat source produces an energy balance in the CC, the model analyses whether the void fraction in the CC is acceptable. If Eq. (68) produces a value between 0.5, the maximum permissible void fraction, and zero, the CC contains a void and the void fraction is acceptable. A void fraction greater than 0.5 indicates that the source temperature needs to be increased until both an energy balance and acceptable void fraction are established. If the void fraction is less than 0, the CC has become flooded and the LHP has entered its constant conductance mode of operation. The CC fluid is no longer saturated and has become subcooled

to some temperature between the saturated temperature of the CC fluid and the CC inlet temperature. The exact temperature to which CC fluid has subcooled cannot be calculated explicitly and the solution algorithm proceeds by decreasing the CC temperature in increments until an energy balance and a void fraction of zero are established. If neither occur before the CC fluid temperature equals the CC inlet temperature, the source temperature is changed and the process repeated.

The final criterion which defines the solution is the pressure drop in the system. Unless the wick has the necessary capillary head to overcome the pressure drop, the LHP will fail even with an energy balance and acceptable void fraction in the CC. To determine the pressure drop the LHP experiences, the following summation of the pressure drops in each component is used:

$$\Delta P_{system} = \Delta P_{wi} + \Delta P_{vg} + \Delta P_{vl} + \Delta P_{cond} + \Delta P_{ll} \tag{71}$$

The pressure drop through the wick is provided by Darcy's Law:

$$\Delta P_{wi} = \frac{\dot{m}\mu_l \ln\left(\frac{d_o}{d_i}\right)}{2\pi\rho_l K_{wi} L_{wi}} \tag{72}$$

The capillary head which the wick exerts on the fluid varies as the pressure drop varies but has a maximum value associated with the pore radius. Using the Young-Laplace equation given in Eq. (54) and assuming the pores are circular, which allows the radii of curvature to be considered equal, the maximum capillary head is given as:

$$\Delta P_{cap} = \frac{2\sigma}{r_{pore}} \tag{73}$$

The LHP operates successfully only if the pressure drop through the system is less than the maximum capillary head the wick is able to exert, given by the following inequality:

$$\Delta P_{cap} \geq \Delta P_{system} \tag{74}$$

2.8. Discrepancies in the model

The model is subject to a number of recognised inconsistencies. These can be divided into deficits in the model itself and deficits in the model due to overlooked specifications in the LHP being modelled. These are considered separately.

2.8.1. Model specific discrepancies

In the analysis of the second heat leak, it is assumed that the energy is transferred through the wick radially, from the outer surface of the wick to the surface of the wick core. However, due to the presence of the vapour grooves and the sintered internal structure of the wick, in which

pores can take complex, three-dimensional paths between the interior and exterior of the wick, this is a simplification. Bai *et al.* [23] discuss this discrepancy in their development of the thermal conductance through the wick and how the actual thermal conductance will be slightly different. However, the use of a radial heat transfer model is not unique to this analysis and is considered sufficiently accurate.

A significant assumption in the analysis of the second heat leak is the neglect of the evaporation and condensation heat transfer between the wick core and the two-phase interface in the CC. This assumption was made in order to bypass the complicated mathematics required in the calculation of the second heat leak. However, the two-phase heat transfer has a significant impact on the amount of heat being leaked. Since the two-phase component of the heat transfer is ignored, the simulated heat leak through the wick will be much lower than the actual value. However, the two-phase heat transfer is only a consideration when the CC fluid is in a saturated state and should disappear at high heat loads when the CC floods. Additionally, research by Zhang *at al.* [9] shows that at high heat loads the mass flow rate would be large enough to collapse any residual vapour trapped in the CC, meaning that there should be no need to simulate the two-phase heat transfer after the LHP enters the subcooled CC fluid mode. The two-phase heat transfer is still significant at low heat loads however.

The model asserts that the fluid in the CC, whether flooded or at saturation, is at a single temperature and pressure. While this assumption is correct when the CC is flooded, there is a difference in temperature when the fluid is saturated between the vapour and liquid phases as the vapour phase is at saturation temperature while the liquid phase is subcooled. As well as suggesting a temperature disparity, this also implies that the fluid in the CC is continually mixing, making the fluid behavior highly complex. It has been suggested that this discrepancy can only be handled by a sophisticated, three-dimensional analysis of the CC [23,25]. In this model however, two-phase considerations in the CC have been neglected or simplified and the assumption of a single temperature in the CC fluid given as the saturation temperature of the incoming subcooled liquid is acceptable. The complexities of the CC fluid do not carry over to the constant conductance mode and the differences associated with this discrepancy will only occur during low power inputs when the variable conductance mode occurs. This discrepancy also only applies for terrestrial applications where gravity divides the liquid and vapour phases. In aerospace applications where gravity is absent or significantly lower, the fluid becomes a suspended, homogenous mixture of vapour and liquid and the assumption of a uniform temperature is acceptable.

This model does not take the influence of the bayonet into account. Because the bayonet is transporting subcooled liquid while in contact with the warmer CC fluid, a heat transfer and

temperature change occurs. There is also a pressure drop as the liquid travels along the bayonet. The effect of the pressure drop is negligible as the length of the bayonet is limited. More influential is the placement of the bayonet exit. The bayonet is positioned so that subcooled liquid exits into the wick core, essentially reducing the temperature of the CC fluid localised in the inner cavity. This will result in an increase in the second heat leak, although the temperature increase of the liquid in the bayonet reduces the impact of this discrepancy somewhat.

The condenser analysis has a few shortcomings. The model considers the two-phase region of the condenser to be under the annular flow regime without liquid entrainment. This simplifies the mathematics and is a fair assessment of the flow as the narrow, long condenser piping and evenly distributed circumferential cooling provided by the heat exchanger suggest annular flow. However, this is considered to occur for the entire length of the two-phase region when in reality it is only applicable for the majority of the initial length. Towards the end of the region, the increasing liquid film size and decreasing vapour velocity reduce the stresses keeping the flow annular and slugs begin to form. The size, location and effect of these slugs are unpredictable but they will affect how the condenser performs, resulting in a difference between theory and experiment.

Another shortcoming of the model is the omission of thermal conduction between increments along the transport line piping. This has been done to reduce the complexity of the model. The effect of neglecting the heat conduction in the piping is difficult to predict but it can be argued that the effect is minimal as the shortness of the spatial increments and relatively low temperature difference between these differential elements mean that whatever heat is being added on the higher temperature side will be removed on the lower temperature side.

Finally, the model does not indicate whether or not the system will stabilise. LHP have unusual behaviours when operated under certain conditions which can lead to non-steady-state operation. For instance, they have a tendency, at high heat inputs, to oscillate due to the close thermal contact between all the components [9]. These temperature oscillations are normally unwelcome in LHP operation as they can lead to higher operational temperatures and unstable thermal management. Since the model is not transient, the oscillations and their severity cannot be determined and thus there are potential conditions under which the theoretical results will be substantially different from the physical results.

2.8.2. Discrepancies associated with physical LHP

The vapour exiting the evaporator is superheated due to the pressure drop in the vapour grooves. However, if there is a void present between the wick and evaporator exit, the vapour may be heated further due to prolonged contact with the evaporator wall. Such a void is not common

practice and has been excluded from the model for the sake of simplicity. A void does however exist in the experimental LHP built in this study and the additional vapour superheat will affect the experimental data, resulting in a discrepancy.

The model assumes that only working fluid exists in the LHP being modelled. However, there is the possibility of non-condensable gases (NCG) entering the system, either through poor charging, insufficient vacuuming or reactions between the working fluid and other materials in the LHP over time. Their presence has been considered before and there have been studies done on their effects [6]. Any NCG in the system will be transported through the lines to the CC where it remains as the liquid is drawn through the wick, as can be seen if Figure 2-4.

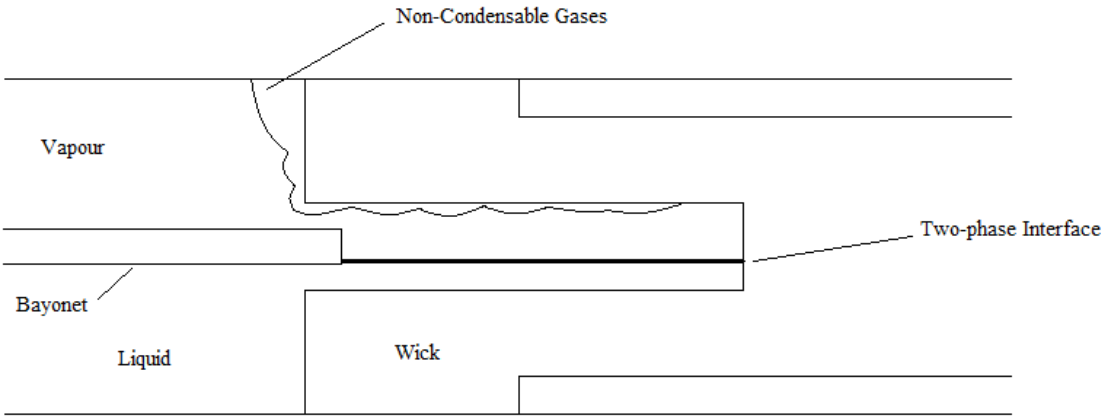

Fig.2-4. Non-condensable gases in the compensation chamber

Since NCG do not condense, they simply occupy space in the CC, reducing the volume available for the working fluid, meaning the CC will flood at a lower heat input. The heat input when the CC floods is usually the point when operational temperature are at their optimum and thus the volume of the CC is designed for a specific heat input. This heat input is reduced if NCG are present. There is also the possibility of NCG in the inner cavity increasing the heat leak through the wick and reducing the amount of liquid able to be drawn through the wick. These all influence the experimental results and cannot be accounted for in the model since the amount of accidental NCG contamination is impossible to determine.

The transport lines are modelled as straight sections of piping without bends. This is inaccurate as there will necessarily be bends which increase the pressure drop. These were not included in the model as an LHP could have quite a complicated transport line path, with any amount of bends at any angle and in any dimension, making an attempt to allow for transport line customisation in the model difficult. There will therefore be an unaccounted for pressure drop in

the experimental LHP not reflected in the theoretical results. The same applies for the condenser section.

There is a further pressure drop unaccounted for in the system. It is assumed that the vapour line, condenser and liquid line are a continuous length of piping but in reality, these lines can be composed of separate sections of piping. For instance, since the greatest pressure drop in the system is through the vapour line, the LHP may use a larger diameter piping for the vapour line and condenser than for the liquid line, meaning that at some point the sections will be joined. The joint will provide an additional pressure drop based on factors such as the diameters of the two sections of piping, the shape of the ends and the way they are joined. Instrumentation such as thermocouples, tee union fittings, and the section of thermocouple itself which interferes with the flow, will also cause a pressure drop. Since these considerations can be varied and complex, with dozens of thermocouples sometimes placed throughout the system, they have been removed from the model but nevertheless influence the experimental results.

The condenser may present a number of complications not reflected in the model. For instance, the model presents the condenser as a straight section of piping free of the influence of gravity. These are shortcomings as the condenser could easily be arranged into any shape and at any angle, gravity-adverse or gravity-assisted. Even if the model was to account for gravity, the bends in complex condenser configurations would probably result in flow which is gravity-assisted in some portions and gravity-adverse elsewhere. This would be difficult to simulate since the effects of gravity on the condenser are significant, shortening or elongating the two-phase region and influencing the formation of slug and bubbly flow.

3. WICK SINTERING

3.1. Introduction

The most important component in an LHP is the porous wick housed within the evaporator. The wick is interesting from a manufacturing perspective as the requirement for characteristics such as high porosity, high permeability and low average pore radius must be optimised to suit the application, even when these factors conflict. Although this study did not require a predefined set of wick properties, optimisation of the various physical aspects of the wick was investigated. The various important features of the wick are discussed below: the powder from which it is sintered, physical dimensions, porosity, permeability, the pore radius and the machining process adopted. The experiments and studies which allowed these parameters to be optimised are then detailed. Finally, the results of the various wicks fabricated are compared and the final sintering specifications determined which produce the most effective wick. The machining of the wick to produce the vapour grooves and inner core is described, demonstrating the success which was achieved in manufacturing a functional, effective wick.

3.2. Design parameters

The various physical aspects which characterise a porous wick structure and their importance and influence over each other are discussed below:

3.2.1. Sintering powder selection

Many powder materials can be used to sinter an effective porous wick structure. The chief concern when selecting a powder is the working fluid, which is chosen for the given application. Once the working fluid is specified, only powders which will not react with it can be chosen, although, even with this primary limitation, there are usually many alternative powders.

Powder selection requires careful consideration of factors such as thermal conductivity, which directly affect heat leaks, the availability of the powder, and particulate size. Typically, a lower thermal conductivity and an average particle size of a few microns is preferred but if this is not possible then a material with a low particle size will be used at the cost of having a higher thermal conductivity [2]. Metallic wicks are therefore often preferred.

If the application calls for a design which will guarantee that wick dry-out does not occur, such as in aerospace or aeronautical systems, a secondary wick is often utilised which extends into the compensation chamber [2]. Such a design can be seen in Figure 3-1.

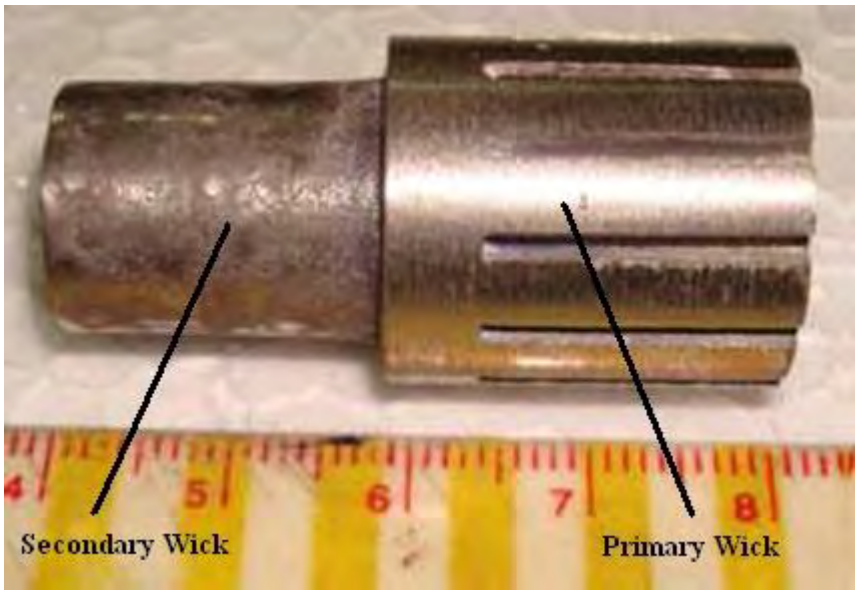

Fig.3-1. Photograph of a sintered wick with secondary wick [30]

This secondary wick can be sintered from the same material as the primary wick but it is usually composed of a material with a greater particle size and a lower thermal conductivity. Since the function of the secondary wick is only to ensure fluid enters the primary wick, its capillary action can be set aside and it can instead be used to increase the overall thermal resistance of the wicks. Two types of powder are usually selected for the inner and outer wick.

Single wick designs usually use a single sintering powder, such as pure nickel, copper or titanium [11,19]. Some studies conducted tested a mixture of powders or other chemicals to improve the final sintered product or ease the manufacturing process [29,32]. The addition of binding elements, strengthening elements or pore enhancers to the primary particulate can be used to change the properties of the part. However, as Xin *et al.* [29] show, there is rarely any benefit gained by these mixtures without loss in another aspect of the wick. Also, additives can require additional equipment and processes during fabrication, such as solvent baths and furnaces for debinding, which were not feasible in this study [32,40].

In this study, the working fluid was ammonia and, supported by previous studies and designs in other research [2,6,23,34], nickel powder was chosen as the sintering material. This was based primarily on the high corrosion resistance of nickel, making it ideal for use with ammonia which is very reactive. Nickel is a good thermal conductor, due to its metallic nature, but its thermal conductivity is lower than competing alternatives such as copper. The powder used in this research has an average particulate diameter of 10 μm, which is not ideal given the preference towards smaller particles in the 2.5 μm range [29,31,34]. The powder is also only 99.5 percent pure rather than the favoured 99.999 percent, leaving trace amounts of impurities. A difference

in purity this small is dismissible although the impurities did manifest themselves in the sintering. An SEM image of one such impurity found in a sintered wick can be seen in Figure 3-2 and its chemical composition is given in Figure 3-3.

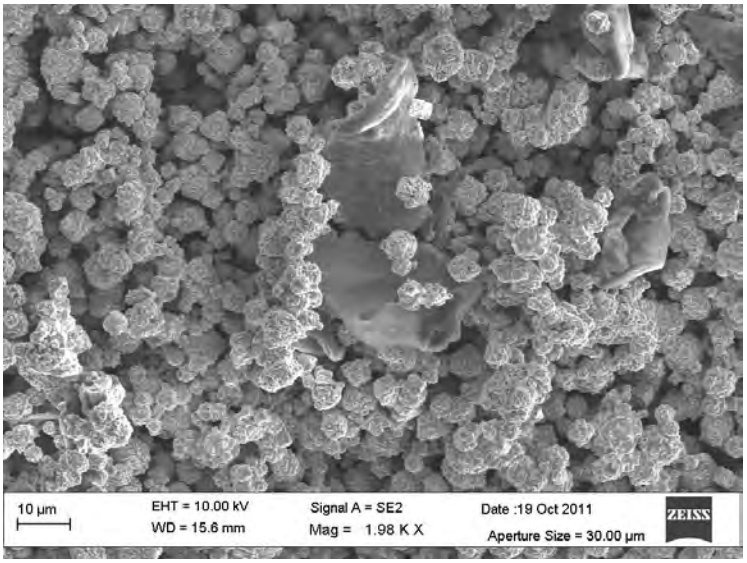

Fig.3-2. An SEM image of an impurity found in a sintered wick fabricated for this study

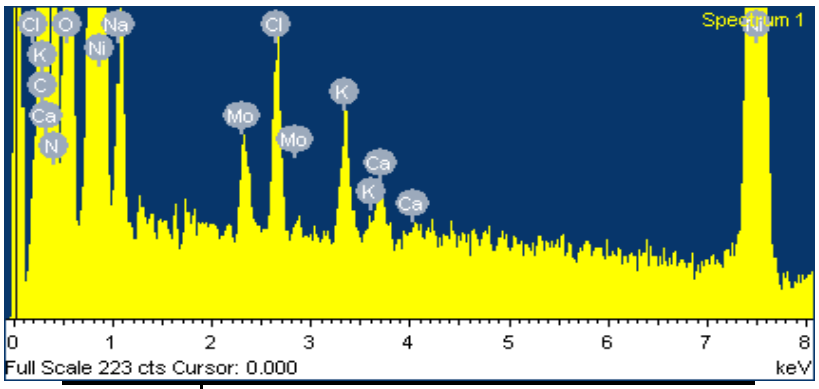

Element	Weight%	Atomic%	Compd%	Formula
C K	16.46	24.37	60.3	CO2
N K	2.96	3.76	11.43	N2O5
Na K	0.35	0.27	0.47	Na2O
Cl K	0.26	0.13	0	
K K	0.21	0.09	0.25	K2O
Ca K	0.08	0.04	0.12	CaO
Ni K	20.96	6.35	26.67	NiO
Mo L	0.34	0.06	0.51	MoO3
O	58.38	64.92		
Totals	100			

Fig.3-3. An energy-dispersive X-ray (EDX) of the impurity

The chemical analysis performed on these impurities using an EDX spectroscope showed the impurities are composed of a collection of oxides. These impurities are rare and thus do not impact on the functionality of the wick.

3.2.2. Physical dimensions and accuracy

Because the wick needs to fit into the evaporator casing and form a seal between the evaporator and compensation chamber, the dimensions of the sintered wick have to be highly accurate. Powder metallurgy has the advantage that parts can be sintered with a high dimensional accuracy, although this depends on the sintering technique applied.

The two techniques commonly used to produce wicks are loose powder sintering and cold-press sintering. In both processes, the powder is placed into the mould before it is inserted into the furnace and during the heating process the particles begin to bond with each other without entering the liquid phase and the sintered powder retains the shape of the mould to create the final product. This also leads to a powder metallurgical phenomenon called densification in which the final density of the sintered structure is greater than the pre-sintered or "green" density [41]. This translates to the volume of the wick in the mould reducing. Figure 3-4 shows the shrinkage of one of the loose powder sintered wicks produced in this study.

Fig.3-4. Photograph of a loose powder sintered wick in the mould

The fraction by which the wick would shrinks is difficult to predict but generally it reduces a few hundred microns in diameter and substantially more in length. Densification allows the wick to be easily pulled from the mould but the reduction in volume raises problems for dimensional accuracy.

In loose powder sintering, the powder is placed into the mould either loose or slightly compressed while in cold-press sintering the powder is compacted using a press before being

sintered. In the former, the lack of powder compression means the properties of the wick can vary throughout the final product. This is because the distribution of powder is not uniform and thus certain volumes within the pre-sintered powder structure will have a greater density than others. This means that a loose-powder sintered cylindrical wick will have an unpredictable reduction in diameter which will vary throughout its length. In cold press sintering, the pressure placed on the powder ensures that the uniformity of the distribution of powder is improved and that all areas of the wick will sinter evenly. There is then a better uniformity of diameter reduction with the cold-press technique. There is also a lower final volume reduction because more powder is required for the compact to be formed, resulting in a higher green density than with loose sintering.

From a purely dimensional accuracy perspective, cold-press sintering is superior. However, after further analysis of other properties of the wick and the techniques themselves, it will be demonstrated that the benefits which cold-pressing brings to dimensional accuracy are not important enough to warrant its use over loose powder sintering. The uneven reduction in diameter caused by loose powder sintering can be overcome by machining the wick.

3.2.3. Porosity

The wick functions by drawing liquid from the compensation chamber and wick inner core through its porous interior to the outer surface where vapour grooves are machined. Thus the ideal wick should be as porous as possible, generally in the region of 55-75% [2,6], while still being able to provide adequate capillary action. However, the porosity of the final product is affected by a number of factors in the manufacture of the wick. These include particulate properties such as the average particle size, the shape of the particle and choice of additives. Manufacturing choices also contribute to the porosity and the most influential of these are the sintering technique and the sintering temperature and time. Concerning technique, cold-press sintering and loose powder sintering produce significantly different results. Because of the high degree of compression needed in cold-press sintering, the green compact has a lower porosity than its loose powder alternative due to the press reducing the size of the pores present before compression. The process of sintering also closes smaller pores more readily than larger pores, causing a large reduction in porosity through densification during the initial stage of sintering [41]. These two phenomena mean that loose powder sintering produces a significantly more porous wick than cold-pressing, available literature suggesting a difference of about 20% [29].

Other manufacturing parameters which affect porosity are the sintering temperature and sintering time which are discussed together because of their interdependency. Sintering temperature refers to the maximum temperature the furnace reaches, while the sintering time

refers to how long the furnace remains at that temperature. The literature available refers to a few optimal sintering times and temperatures but these are only convenient as guides because the heating characteristics of a particular furnace also influence the final porosity. For instance, Xin *et al.* [29] report an optimum temperature and time of 650°C and 30 minutes whereas Wu *et al.* [35] found an optimum porosity at 600°C. The furnace used in the former heated up by 20°C every minute whereas the latter was set at 10°C per minute. The furnace used in this study had a maximum heating rate of 10°C per minute which was further reduced for safety. Because the heating conditions are so different in other studies, a study on the optimum sintering temperature and sintering time was conducted separately.

Many aspects of the wick are directly dependant on its porosity, such as permeability, thermal resistance and physical strength. Emphasis should be placed on maximising the porosity of the sintered wick and for this reason the loose powder sintering technique was chosen as it produces wicks with high porosities.

A density test is can be used to measure porosity. This involves measuring the mass of a dry sintered wick, M_{dry}, the mass of the wick when it is fully saturated with fluid, M_{sat}, and the mass of the saturated part when it is suspended in fluid, $M_{suspend}$. Distilled water is usually chosen as the fluid which the wicks are saturated with. Eq. (75) is then used to calculate porosity, ε.

$$\varepsilon = \frac{(M_{sat} - M_{dry})/\rho_l}{(M_{sat} - M_{suspend})/\rho_l} = \frac{M_{sat} - M_{dry}}{M_{sat} - M_{suspend}} \tag{75}$$

A study on the sintering temperature and holding time that would quantitatively optimise the porosity was then conducted and the testing procedure and results are described in Section 3.3.3.1 and Section 3.4.1.

3.2.4. Permeability

Permeability is the wick's resistance to flow. It is best if the wick is fabricated to be as permeable as possible since this allows for a lower pressure drop through it. Along with porosity, high permeability is a defining property of an exceptional wick.

To sinter a highly permeable wick, the same factors which influence porosity apply. Cold-pressed wicks sintered using the same regime as their loose powder counterparts display a lower permeability [29]. This is because permeability is dependent on porosity and average pore diameter since the greater the amount or size of pores in the wick, the less the flow of fluid through the wick will be inhibited by friction. Apart from fabrication technique, the temperature and time of sintering are influential. Because of their dependency, the same conditions which produce good porosity also produce good permeability. However, there remains a need to

quantify the permeability since it is required as an input to the mathematical model for determining pressure drop through the wick. While it is possible to determine the permeability by measuring the pressure drop across a sample and applying Darcy's law, it is more economical to use an equation relating permeability to the porosity and average diameter of the particulate. A simplified Carmen-Kozeny equation, which is similar to Darcy's law but uses the porosity and particle diameter as variables, is given as [29]:

$$K = \frac{d^2 \varepsilon^3}{180(1-\varepsilon)^2} \tag{76}$$

In this equation, d is the average particle diameter. Importantly, this estimation depends on the particulate being spherical which is discussed in Section 3.3.3.2. In this study, the permeability of the wicks was calculated from the measured porosities and their overall functionality, as defined by porosity and permeability, is described in Section 3.4.2.

3.2.5. Pore radius

The average pore radius must be determined because of its impact on the physical limitations of the system. Capillary action is produced by the viscous nature of the liquid in the pores which allows the liquid to be pulled through the wick and overcome the pressure difference between the evaporator and CC. This difference in pressure must match the pressure drop throughout the entire system, thus if the capillary force of the wick is insufficient to generate flow, the system will fail. The maximum available pressure the wick is able to generate is determined by the viscosity of the liquid and the average pore radius. The smaller the pore radius is, the greater the adhesive and cohesive forces of the fluid in the pore. The viscosity and pore radius are related to maximum capillary pressure by Eq. (73).

$$\Delta P_{cap} = \frac{2\sigma}{r_{pore}} \tag{73}$$

The capillary pressure is inversely proportional to the pore radius, meaning a smaller pore is important for the fail-safe functioning of the system or for the development of longer or gravity-adverse LHP designs.

The pore radius can be found experimentally through a statistical analysis of a wick image, usually from a Scanning Electron Microscope (SEM) [29]. Other methods are popular such as the bubble point test [4], which can be used to experimentally determine the largest pore diameter. The best empirical test is to install the potential wick in a system and see if it performs under extreme conditions. This is unnecessary, however, as the information from the SEM statistical investigation and the safety factors used in the design should guarantee performance.

3.3. Manufacture and analysis

The fabrication of a wick began with the manufacture of a suitable mould which was then filled with the chosen sintering powder and heated in an inert gas furnace to a predetermined temperature for a predetermined period of time. When complete, the sintered wick was removed from the furnace once it had cooled and its various physical properties were measured or calculated and documented.

3.3.1. Sintering Mould

Since the LHP being developed was not application sensitive in terms of its outer loop length or diameter and length of the evaporator, the wick need not be constructed with any specific dimension. However, the limitations on size were established by the available space within the furnace used in the manufacture process.

The space available in the furnace was a 3.375 *l* cube. Suspended from the top of the furnace was a thermocouple used to measure the temperature of the furnace while it was operating. This thermocouple extended about 35 mm from the roof of the furnace. The furnace had four elements suspended along the walls, two each side, and on the wall opposite the door was an orifice through which inert gas entered the chamber. A photograph of the interior of the furnace is shown in Figure 3-5.

The mould was designed such that it fitted into the available volume without blocking the gas entry hole and was not close to any element whilst maintaining a similar ratio of length to diameter found in comparable studies [9,11,21,23]. A two-halved mould was machined with each half-mould having a length of 120 mm, a width of 40 mm and a height of 30 mm. The moulds were machined from graphite which was chosen for its high thermal conductivity, low coefficient of expansion, poor interaction with nickel and its common use in wick manufacture and other applications [29,30,31,34,40]. A semicircular, cylindrical cavity was machined into each of these moulds so that the wick could sinter as a cylinder when both half moulds were fitted together. The cavity was 100 mm long and 18 mm in diameter. The length was mainly influenced by the spatial constraints of the furnace while the diameters of the wicks used in similar studies were around 18 mm. The wick was machined down to a more suitable diameter after sintering. Although the cavity was nominally 100 mm in length, it had 3 mm fillets machined at either end, making the actual cylindrical part of the cavity around 80 mm in length.

Fig.3-5. A photograph of the interior of the furnace

To keep the two halves together whilst sintering, a groove was machined around the top edge of one of the half-moulds, dubbed the female, while a corresponding ridge was machined into the other, the male. The low tolerance between the ridge and groove provided enough friction to hold the two halves in place without a clamp. In order to fill the mould once the two halves were joined, the female half had a 10 mm hole drilled into it vertically at one end through which nickel powder could be fed. The two mould halves can be seen in Figure 3-6. The feeder hole is visible on the female part of the mould.

Fig.3-6. The two half-moulds with male on left and female on right

3.3.2. Sintering

The sintering process chosen was the loose powder sintering technique. The two half-moulds were joined together and the inner cavity of the mould filled with the nickel powder, after which the mould was placed into the furnace. Nickel readily oxidises at elevated temperatures but must

remain unoxidised when the sintering temperature is between 550 °C and 650 °C, thus an inert gas furnace was used. A vacuum pump was used to evacuate the furnace. When the vacuum pressure reached its lowest value, an argon gas canister was opened and the pressure in the furnace increased to atmospheric levels. The gas outlet valve was then closed and the vacuum pump switched off in quick succession to prevent any air from returning to the furnace. The furnace was switched on and the sintering process started. The mould and powder were heated up to the required temperature, held there for a set period of time, and then allowed to cool to room temperature before being removed from the furnace and the wick pulled from the mould.

Due to limitations on the heating rate of the furnace elements and the heat leak to atmosphere after the interior increased above 300°C, the heating regime employed raised the temperature of the furnace from ambient to the sintering temperature in two and a half hours. This lead up time was used for all sintering temperatures during the wick optimisation. Once the sintering temperature was reached, the furnace dwelled for 10 minutes before cooling down. This sintering time was maintained for all sintering temperature experiments.

3.3.3. Wick analysis

The sintered wick had four properties which were of interest: the dimensions of the wick, the porosity, the permeability and the average pore radius. Of these, only the latter three were immediately important to the mathematical model since these could not be altered after sintering. The dimensional accuracy of the wick was not as important to the operation of the wick because the wick would be machined to the necessary dimensional specifications without loss of functionality.

3.3.3.1. Porosity analysis

The porosity was found using a density test. To measure the masses, an electronic scale, precise to a thousandth of a gram was used. For the dry mass, the wick was simply placed on the scale and a reading taken. The wet mass measurement began by submersing the wick in a container of near-boiling distilled water for about six hours to ensure that the porous volume of the wick has been completely saturated with water. The wick was then removed from the container and weighed on the scale. The mass of the wick while it was submersed in water was measured using a weight with known mass and an arm balance. Attaching the weight and wick suspended in distilled water to each arm of the balance allowed the submersed mass to be indirectly measured as the difference between the measured mass of the weight and its actual mass. All measurements were repeated a number of times to generate an average and using Eq. (75), the porosity of the wicks were calculated. These results are given in Section 3.4.1.

3.3.3.2. Permeability analysis

The literature suggests Eq. (76) is a sufficiently accurate method of calculating the permeability [29]. This requires only two values: the porosity and the average particle diameter. The porosity was calculated while the average particle diameter was given by the manufacturers along with other important data like the purity of the nickel powder. The Carmen-Kozeny equation assumes that these particles are perfectly or near perfectly spherical which is another consideration in the purchase of sintering powder and a characteristic not often provided by the manufacturers. The information supplied with the nickel powder used in this research stated that the average particle diameter was 10 μm and subsequent analysis of the wick using SEM imaging demonstrates their reasonably spherical nature. This can be seen on Figure 3-7.

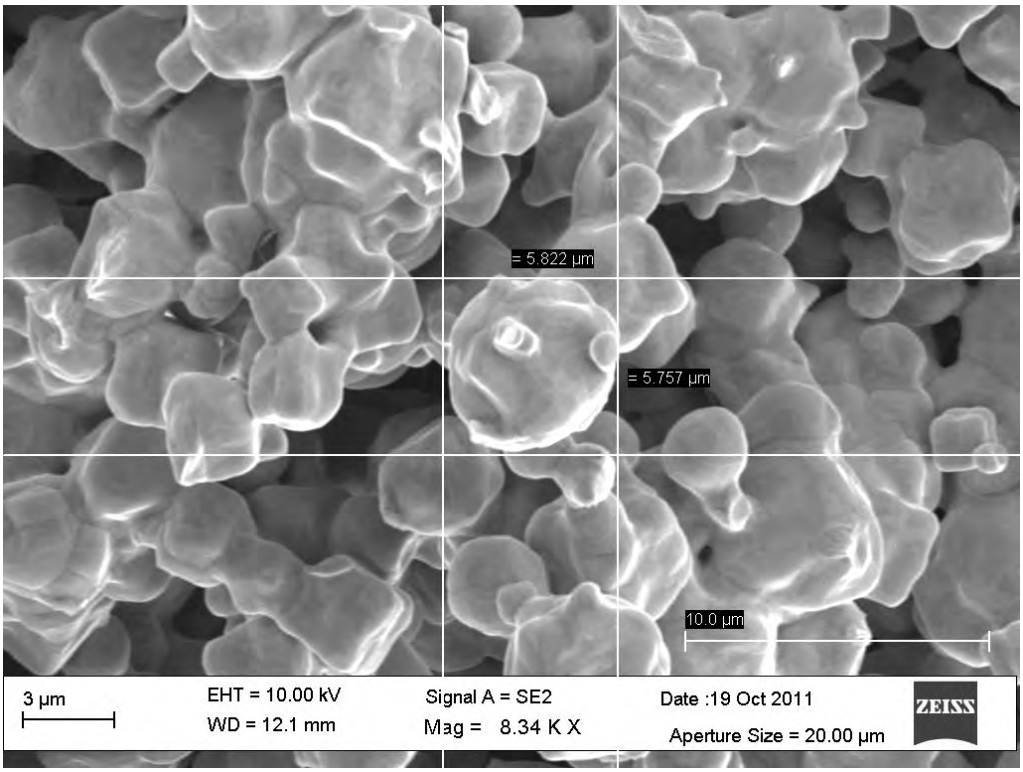

Fig.3-7. SEM of a sintered wick from this study illustrating particle size and shape

Using this data, the corresponding permeability of the wick was calculated. The results are shown in Section 3.4.2.

3.3.3.3. Pore radius analysis

The average pore radius was found from statistical analysis of SEM images of the porous microstructure of the wick. An SEM image of a fractured cross section of a wick was taken at a number of magnifications. The difficulty with selecting the optimum magnification was in finding a balance between images which clearly show pores with areas often a fraction of a

micron, and having a large enough image to make the number of pores visible statistically acceptable. Thus images with magnifications of 500, 800, 1500, 6000 and 8000 were taken and the visibility of the pores examined. The most useful magnification was 1500 times, as both large and small pores were visible.

The nature of SEM microscopy is that the images which are taken are in greyscale. This means that the particulate appears light whilst the pores in between them appear darker. An example from a SEM is shown in Figure 3-8.

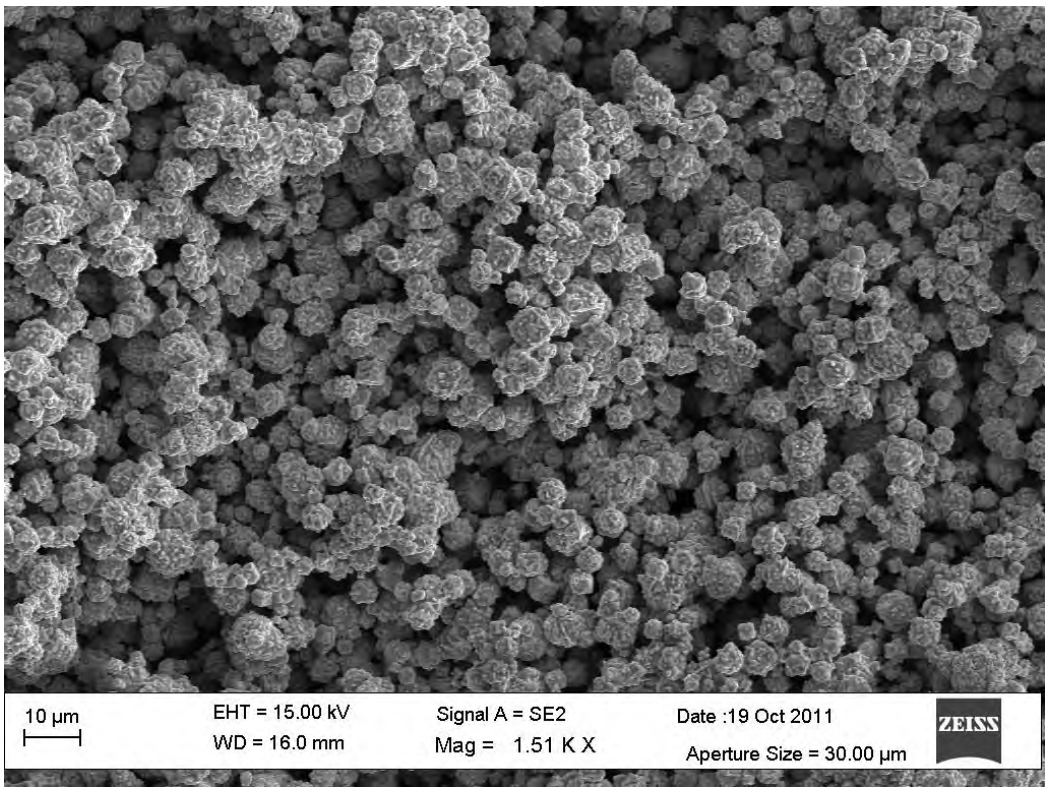

Fig.3-8. A SEM image of a wick, magnified 1500 times

To highlight the dark regions and thus the pores, a binary map of the image was constructed. A binary map is a black and white converted image, in which the black and white areas are determined by selecting a threshold value between 0 and 225 in the original picture. There were, however, some technical aspects to this method which proved to be problematic and needed to be refined in order to develop an accurate binary map.

Before the binary threshold could be applied to the images, the images had to be uniform in contrast and brightness to maintain a level of consistency. The SEM produced images which were taken at a variety of contrasts as the orientation of the surface of the wick could not be kept constant. This produced images which, while clear to the observer, were visibly quite different. Since the process by which they would be analysed would be automated, the contrast

had to be adjusted and uniform for each image. The two image processing software packages which were investigated were the MATLAB Image Processing Toolbox and Nikon NIS-Elements Image Analysis plug-in. Both packages had the capacity to adjust the contrast in a number of ways, including manually adjusting the maximum and minimum ranges. It was found that both packages have an automated contrast adjustment setting which spreads the original image's intensity spectrum such that the intensity profile remained the same but began and ended at 0 and 255 respectively. A visual inspection of this contrast setting as adjusted by the NIS-Elements package shows that it delivers a clear and accurate view of the pores in every image and thus was chosen as the standard contrast for each image. Figure 3-9 illustrates an example on the contrast adjustment given by the NIS-Elements package.

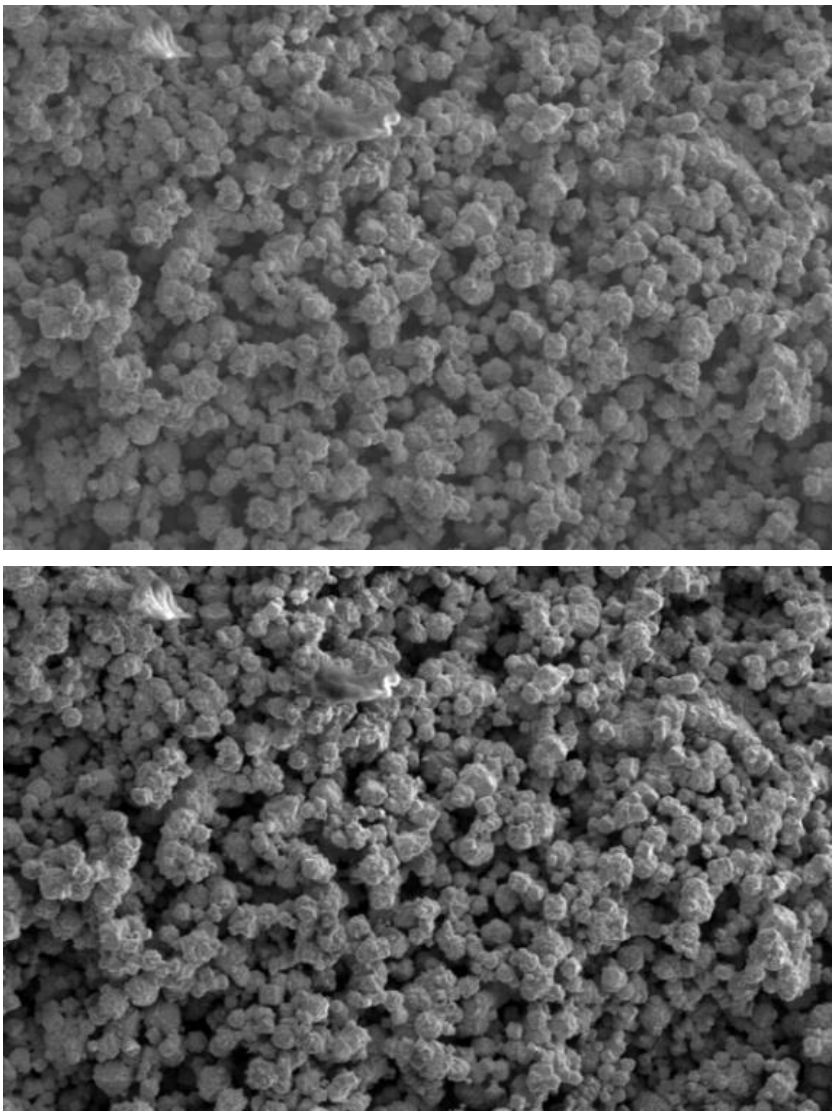

Fig.3-9. Original (top) and contrast adjusted (bottom) SEM images

The contrast adjustment was, however, found to darken particles if they are deep within the pores, as can be seen in Figure 3-10. These images have been brightened for visual clarity.

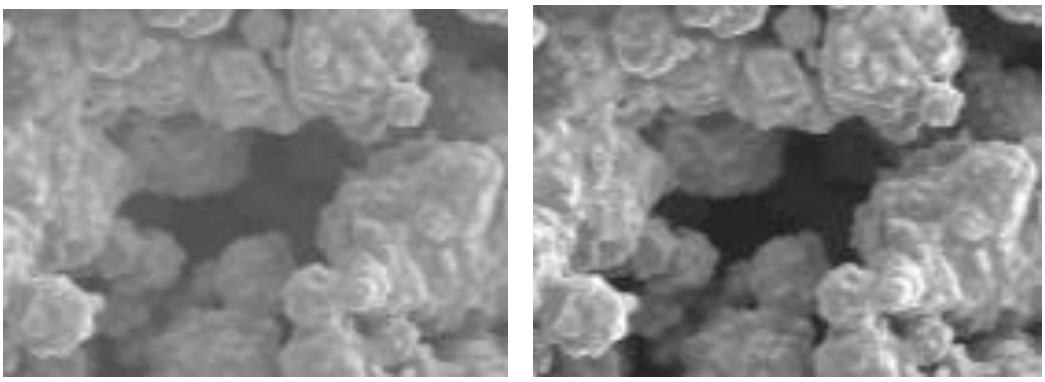

Fig.3-10. Original (left) and contrast adjusted (right) images of a pore

This was not problematic as the pixels which compose the pores in these images had grayscale intensities sufficiently different to the particles to be differentiated by the thresholding process and the particles were removed when the binary image was created.

Once the images had had their contrasts altered, the threshold used to create the binary could be defined. The threshold could be anywhere between 0 and 255 or between any two intensities. The range of values within the threshold definition were replaced with a value of one and appeared white on the binary map, while the values outside the definition were allocated with zero and appeared black. Since the aim was to highlight all the darker pores, the threshold had to be on the lower regions of the spectrum. As with the contrast setting, a certain level of uniformity of processing was required and a particular threshold value was needed which could be used for all SEM images. Without a consistent threshold value, it could be argued that the binary of one image would be inconsistent with others since a slight variation in the threshold could significantly change the size of the pores and upset the statistical results. With a consistent threshold value, even if the thresholding value produced an inaccurate binary map, the fact that it and the contrast were consistent allowed the pores to be comparatively examined. The process of selecting a thresholding value was done purely by inspection and the threshold value used on all the SEM contrast adjusted images.

The visual inspection was conducted to find the threshold which produces the most accurate binary image of the pores. The contrast adjusted image was loaded into Nikon NIS-Elements and the threshold application opened. This allowed the threshold to be set to any particular intensity, the selected threshold spontaneously appearing as a binary on the image. By adjusting the binary to appear transparent rather than white, the software developed shapes corresponding to the outer edge of the pores. The resulting image allowed the actual image to be compared to the binary which would be generated. An example is shown in Figure 3-11.

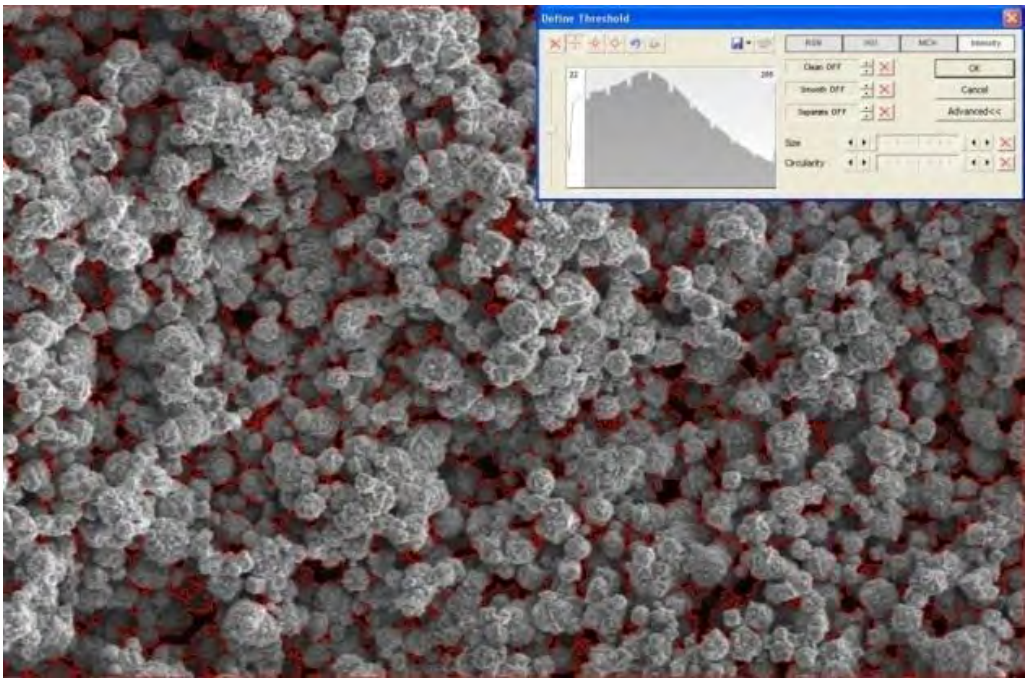

Fig.3-11. A transparent binary in red superimposed on a SEM image

It is not immediately obvious from Figure 3-11 but this particular intensity threshold was inadequate. Some of the pores had been rendered too large by this binary as the threshold had been set too high to remove the darker particulates visible within the pores. Figure 3-12 shows a close up of one such pore from the above example, where lighter shades, indicating the presence of particulate, were within the perimeter of the pore. This image has been brightened for visual clarity.

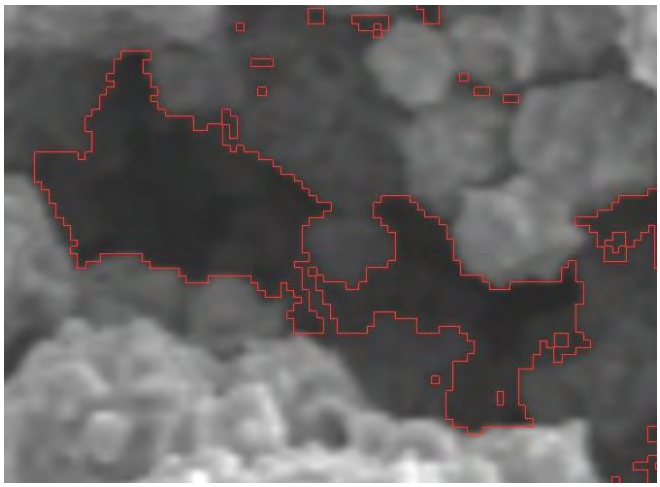

Fig.3-12. Close up of a pore from the previous image

Another area of concern were pores so small they only appear as a single pixel or a handful of connected pixels. A binary which was too low would not register these pores as they do not

appear to be as dark as the larger pores. Although the contrast adjustment performed previously was intended to correct this, the danger was still present and careful observation was required.

Both MATLAB Image Processing Toolbox and Nikon Elements have the option to smooth and clean the image. The former function remove pixels from the binary according to the mean intensity of their surrounding pixels, effectively increasing the circularity of the pores, and the latter removes all small pixels. These functions, if utilised, result in many pixels being disregarded and consequently many pores are either reduced in size or removed completely. Thus neither of these options is utilised in the creation of the binary map.

After adjusting the intensity threshold and visually inspecting the SEM image of the wick, the most accurate threshold value for all contrasted images was found to be 15. This binary displays the larger pores accurately, removing the inner particulate whilst still accounting for the numerous smaller pores. An imposed binary map can be seen in Figure 3-13 with this threshold.

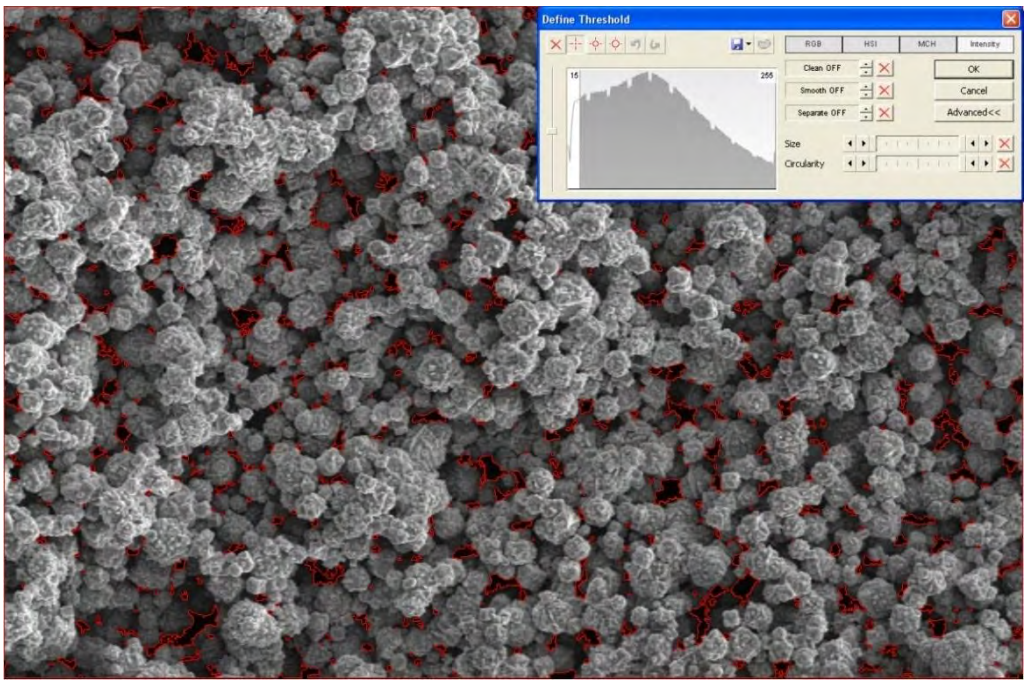

Fig.3-13. A SEM image with a binary threshold setting of 15 superimposed

Once the binary has been defined it was edited to remove all pores in contact with the outer edge of the picture before being processed using MATLAB Image Processing Toolbox. The pixels which composed the pores were detected using the object counting algorithm. This algorithm required a connectivity specification, either a 1, 4, or 8. The connectivity determined whether pixels connected together, either horizontally, vertically or diagonally, should be classed as a single object. A connectivity of 1 separated every pixel into its own individual entity, rendering it useless for this application. A connectivity of 4 or 8 is better, as both class a

large pore as a single object, but a connectivity of 4 would separate any diagonally placed pixels into two individual objects. A connectivity of 8, on the other hand, assumed all pixels connected in any way were part of the same body and allocated them as a single object, which was a better estimation. This was because, even if these pixels related to separate pores, assuming that a small pore was part of a larger pore produced a statistical worst case scenario since the calculated average pore radius would then be slightly larger than the actual average pore radius. A connectivity of 4, where the pixel was kept as its own object meant the number of recognised pores was greater, producing a lower average pore radius.

By activating the counting algorithm with a connectivity of 8, the total number of pores was quickly calculated. A second algorithm calculated the total area of the pores in pixels. The total porous area in micrometres was found by multiplying the pixel area by the squared pixel length which was found by calibrating the original image in NIS-Elements. The total area was then divided by the total number of pores to find the average pore area and consequently the average pore radius. The results are discussed in Section 3.4.3.

3.3.4. Wick optimisation

Due to their importance in the operation of the LHP, the porosity, permeability and pore radius of the wick must be optimised in the sintering process. Since the sintering time and lead up time were kept constant, the only variable that was considered was the sintering temperature. In order to produce the best porosity, permeability and pore radius, a study was conducted to determine the sintering temperature which would optimise these properties in the wick.

Previous studies suggest that the optimum sintering temperature is in the region of 600°C for a period of 30 minutes [29]. Because of the low heating rate of the furnace, the sintering time for the wicks was shortened to 10 minutes. Determining optimum sintering temperature was then a matter of sintering several wicks over a range of temperatures and comparing their properties. Five temperatures between 550°C and 620°C were considered. This range goes below 600°C because the wicks were exposed to slightly lower temperatures for longer, aiding in sintering, and thus the sintering temperature did not need to be as high. The temperatures chosen were 550°C, 570°C, 580°C, 600°C and 620°C.

3.3.5. Machining

The porous nickel cylinders produced by sintering were machined with an inner cavity to allow the liquid in the CC to be absorbed into the wick and with vapour grooves to transport evaporated fluid to the vapour line. These features can be seen in Figure 3-14:

Fig.3-14. Wick with inner core and vapour grooves

Machining is an important consideration as fundamental properties of the wick can be affected or the entire wick broken by the machining process.

The effects of machining were investigated by visually inspecting the features using scanning electron and optical microscopy to determine how the machined surface had altered. Two experimental wicks were used, one saturated with distilled water and the other kept dry. They were used to determine what effect the presence of water in the pores may have on the pore structure during machining.

The first test determined if the machined surfaces were still permeable. This was done by first drying out the wet wick and then pouring near boiling water into the inner cavity and vapour grooves of both wicks. The permeability of the surface was indicated by how readily the water was absorbed. The next test was a comparison of the wet and dry machined surfaces to the outer, non-machined surface and a portion of the cross-section of the wicks. This was by visual inspection of SEM and optical microscope images of these surfaces. A machined surface which looked similar to these surfaces indicated that the machined surface had not suffered damage. The permeability test and images from the SEM and optical microscope are discussed in Section 3.4.4.

3.4. Results

Figure 3-15 to 3-17 show porosity, permeability and pore radius against sintering temperature for wick optimisation. It is apparent that the optimum sintering temperature was 550°C where the highest porosity and permeability are found. The pore radius at this temperature was inconclusive.

3.4.3. Porosity results

The porosity is graphed in Figure 3-15 against sintering temperature.

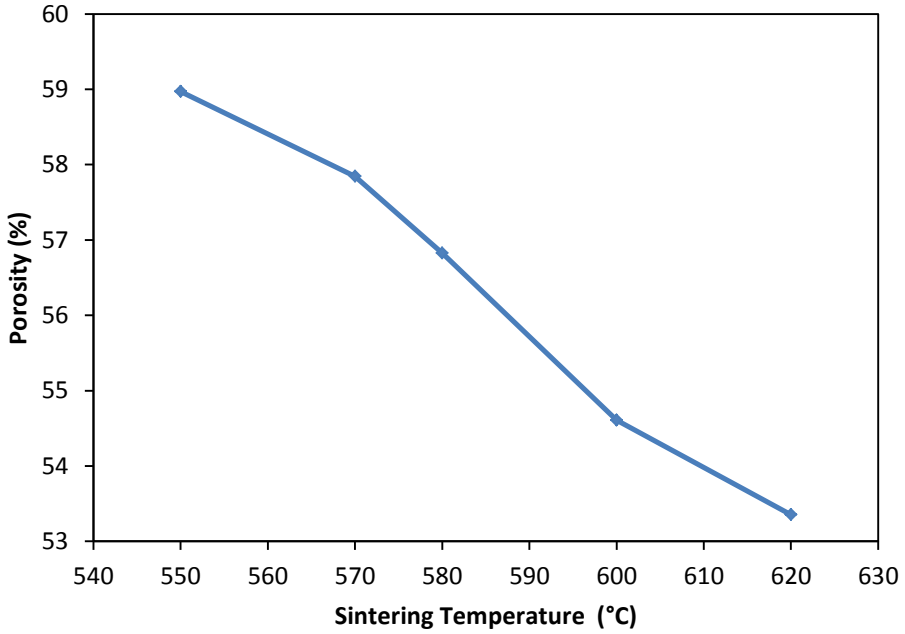

Fig.3-15. Graph of average porosity versus sintering temperature

Figure 3-15 suggests an almost linear decrease in porosity as the sintering temperature is increased. This was expected as increased heating leads to greater interparticulate fusing and mass transfer through the wick [41], reducing the size of larger pores and closing finer ones. From the above data, it would seem that the range of sintering temperatures investigated was not large enough. This range of temperatures was based on similar studies but reduced as to account for the increase in lead-up sintering time. This reduction appears to have been too conservative as the linear decrease suggests that a higher porosity could be found at temperatures even lower than 550°C.

To determine if the temperature range was too conservative, an additional wick was sintered at 520°C to see if the trend extended that far back. If the trend remained linear, the porosity of this temperature should have been 62%. However, the density tests conducted on the wick found its porosity to be around 59%. From this it can be determined that even if the porosity does increase above 59% between 520°C and 550°C, this increase will not be much greater and thus the data collected is sufficient to conclude that the optimum wick sintering temperature for this research is 550°C. Many studies utilise wicks with porosities between 55% and 60%, meaning that the wick sintered here was satisfactory for its purpose.

3.4.4. Permeability results

The permeability is graphed in Figure 3-16 against sintering temperature.

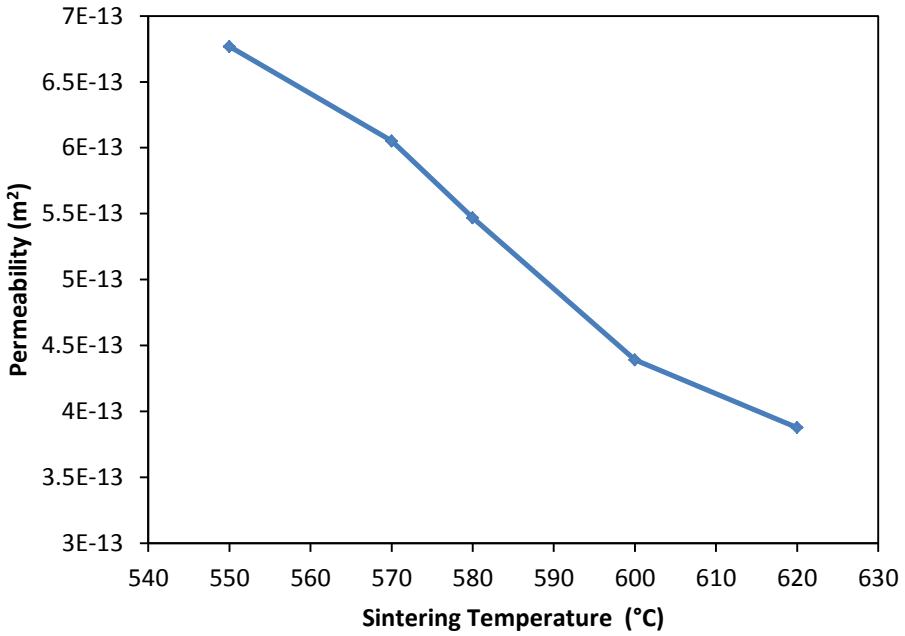

Fig.3-16. Graph of permeability against sintering temperature

Figure 3-16 shows a nearly linear decrease as sintering temperature increases, as with the porosity. This is due to the use of the Carmen-Kozeny equation in which permeability is almost directly proportional to porosity. This means that optimisation of porosity will directly lead to an optimisation in permeability.

From the collected data, the greatest permeability, found at 550°C, is 6.77 x 10^{-13} m^2 which is unusually high when compared with other studies which report values in the low 10^{-13} and 10^{-14} range [23,29], even with more porous wicks. This is because permeability is also proportional to the square of the average particle diameter. The powder used here has a much higher average particle diameter than that used in similar studies, thus contributing to a higher permeability. In most studies, smaller diameter particles are preferred over larger ones, but clearly this is not in order to maximise permeability. Rather, sintering with smaller particulate results in very fine pore radii which increase the maximum pressure head the wick can generate at the cost of permeability. It is sufficient to state that sintering at 550°C with a large particle size powder produced an exceptionally permeable wick.

3.4.5. Pore radius results

The average pore radius is graphed in Figure 3-17 against sintering temperature.

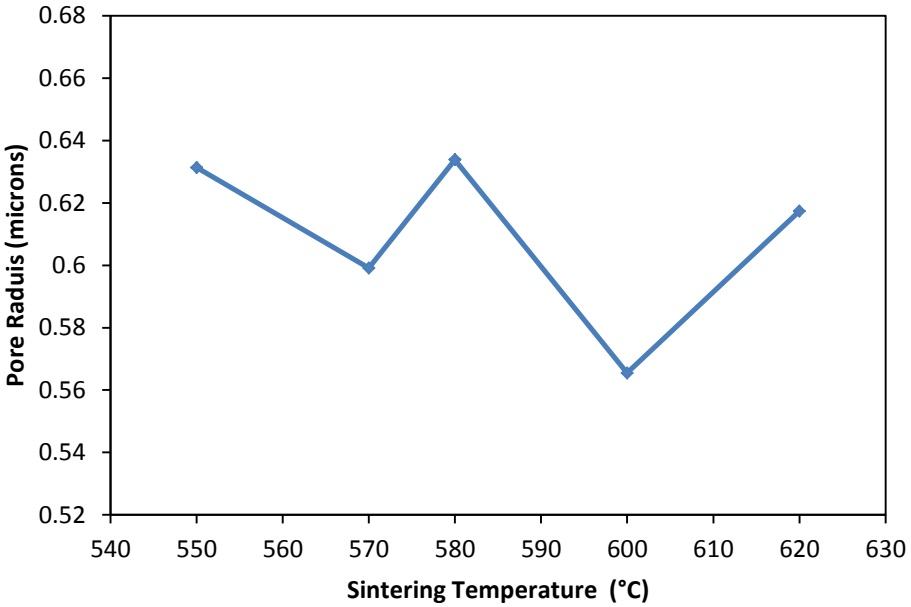

Fig.3-17. Pore radius versus sintering temperature

The average pore radius in Figure 3-17 appears erratic, with no clear correlation between pore radius and sintering temperature. This does not mean that a correlation does not exist but that factors such as the sintering technique upset the findings. The loose powder sintering technique produces wicks with non-uniformly distributed properties and averaged porosity and permeability values were found by considering the wick as a whole. The pore radius, however, was found using an image of a portion of a wick cross-section and thus the value found only described that particular portion of the wick and not the average. As an illustration, a wick sintered at 620°C had SEM images taken near the top and near the bottom of a cross section. The average pore radius at the top was found to be 0.65 µm while the average pore radius at the bottom was found to be 0.58 µm. There is a clear variation in pore radius throughout the wick.

The pore radii shown in Figure 3-17 are unusually small, considering the powder used in this research had a large average diameter and it was believed that finer powders would induce finer pores. It is possible the nature of loose powder sintering reduces the average pore size more than was originally believed. However, this is simply speculation and will have to be considered in further research.

Because of the inconclusive pore radius results, the wick was optimised in terms of porosity and permeability and not pore size. Instead, the average pore radius was considered a design constraint on the LHP once the optimised wick had finally been sintered. The pore size of the final wick could not be determined from the results so a pore radius greater than all the recorded radii was used instead. The use of this enlarged pore radius introduced a safety factor into the design of the LHP which prevents the capillary pressure ever being too weak to overcome the pressure drop in the outer loop. A safety factored average pore radius of 1 μm is considered sufficient to satisfy the pressure drop design constraint in the LHP. Using Eq. (73), an average pore radius of 1 μm and considering the liquid in the wick to be at 45°C with the corresponding surface tension, the maximum pressure the wick can produce is 37.7 kPa.

3.4.6. Machining results

It was necessary to test if the wicks were still permeable after machining. This was done by pouring near boiling water into the inner cores. The water was almost immediately absorbed into the wicks, indicating that both surfaces were still permeable.

An optical microscope was used to view three areas of both the wet and dry wicks: the outer surface, a cross-section created by fracturing the wick and the machined vapour grooves. The surface of the inner core could not be captured satisfactory and was not included but it was assumed the surface would be sufficiently similar to that of the vapour grooves. The images captured for the vapour grooves, looking at the bottom of the groove and sides of the groove respectively, are given in Figures 3-18 and 3-19. In the side view of the vapour grooves, the dark region at the bottom of both images is the lip of the vapour groove.

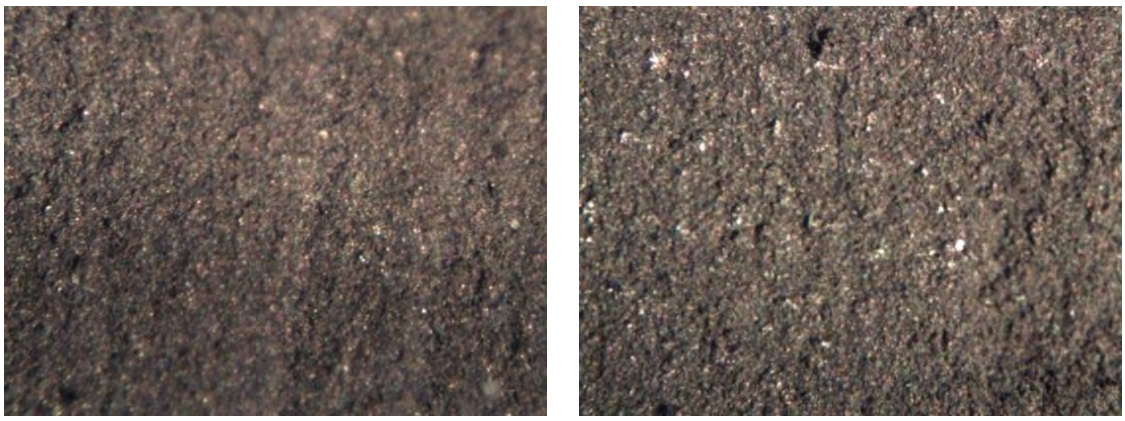

Fig. 3-18. Images of the bottom of the machined vapour groove for the wet wick (left) and dry wick (right) magnified 40 times

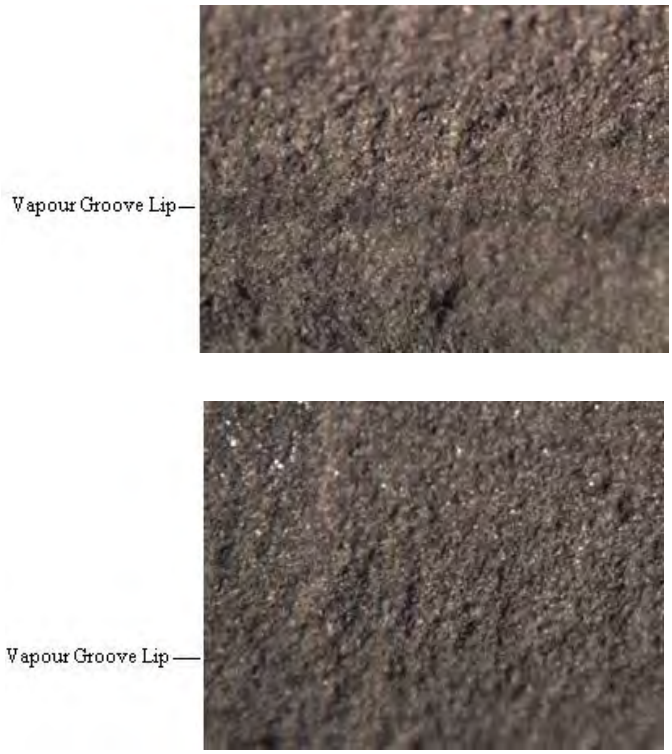

Fig.3-19. Images of the side of the machined vapour groove for the wet wick (top) and dry wick (bottom) magnified 40 times

There is good similarity between the wet and dry machined wicks, although slight differences exist. While the images are comparable, an obvious difference is the larger number of bright spots on the dry wick images. Initially these were thought to be areas of the wick ground down by the drilling process. However, these spots were found throughout both wicks, as shown in Figure 3-20. It is thought that these are simply clusters of particles orientated to reflect the light.

Fig.3-20. Images of the outer surface of the wet wick (left) and dry wick (right) magnified 40 times

It was determined that machining a dry wick produced vapour grooves and an inner chamber with a quality and functionality comparable to those machined into a water-saturated wick and that the machined surfaces on both were still permeable. Saturating the wick with water therefore had no effect on the machining.

In addition to the optical microscopy, two SEM images of the machined vapour groove bottom surface and a fractured cross section surface are given in Figure 3-21. From these it is clear that there is little difference in pore distribution and structure, indicating that the drilled surface is as porous and permeable as the interior of the wick.

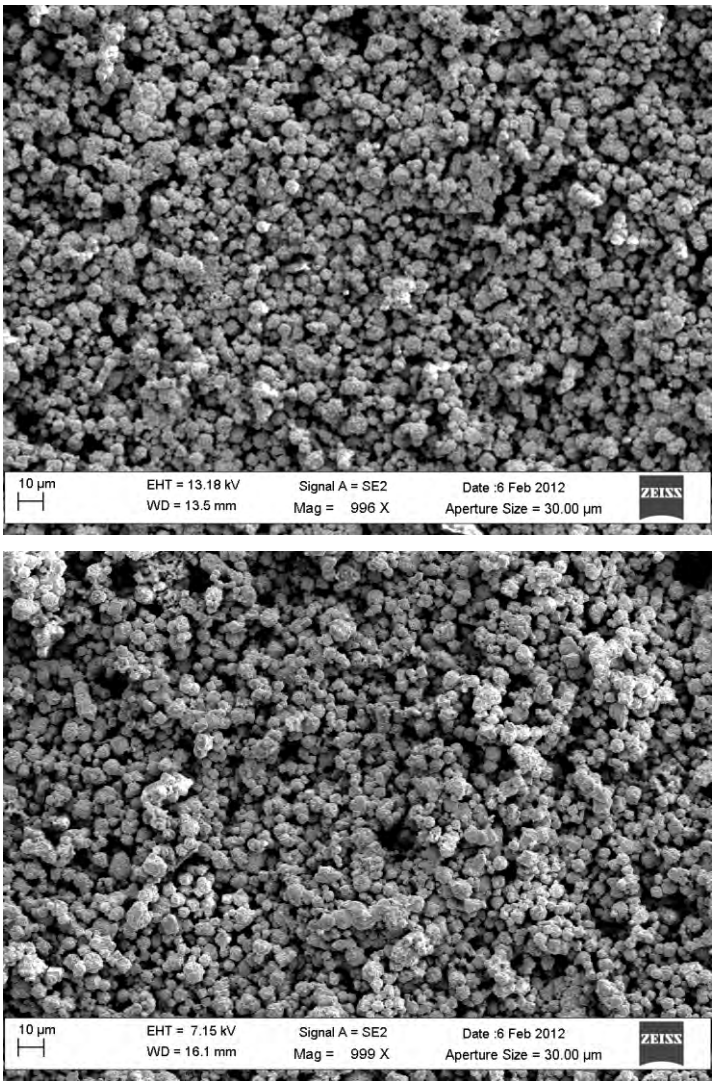

Fig.3-21. SEM images of a machined surface (top) and a cross-section (bottom) magnified 1000 times

However, the machined surface and the outer surface of the wick in Figure 3-22, appear very different. The outer surface of the wick has a more level and uniform appearance due to the effects of sintering against a surface. By comparison, the action of the drill has created a jagged

and rough surface, exposing and opening the pores in the vapour grooves. This suggests that the machined surface is more permeable than the sintered outer surface. The large bodies in the sintered outer surface SEM image are impurities and can be ignored.

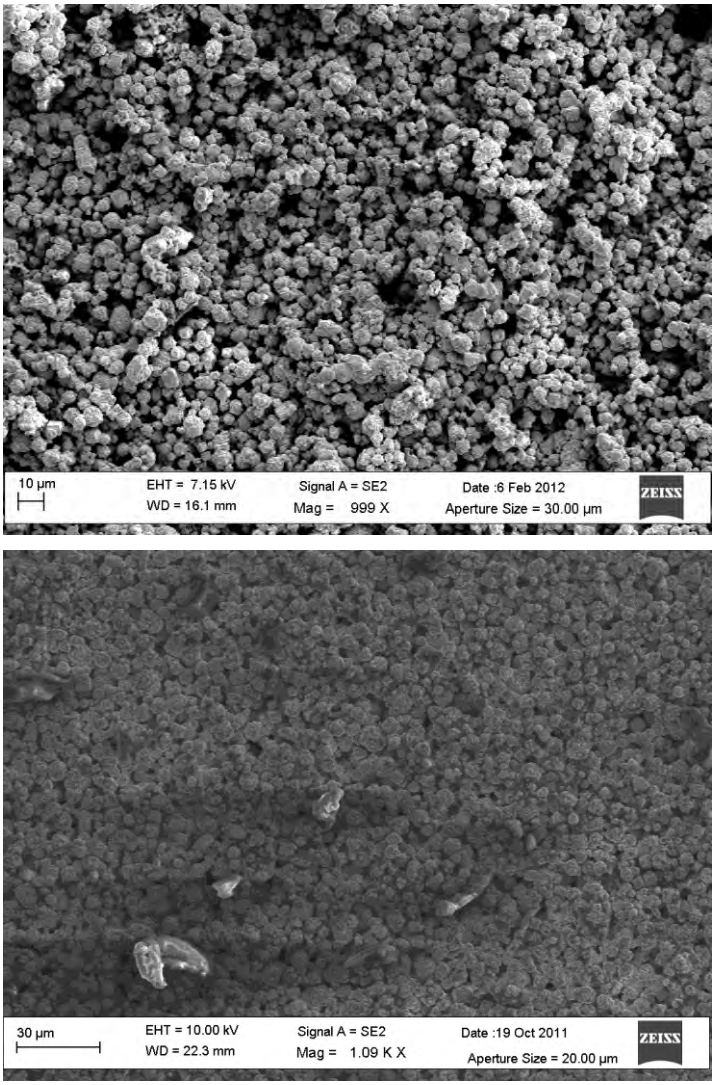

Fig.3-22. SEM images of a machined surface (top) and an outer surface (bottom) magnified 1000 times

Initial concerns about the effect of machining were dismissed as the action of the drill did not distort or grind the pores shut. Rather, the machining removed particles in contact with the tool, exposing a highly porous and damage-free interior.

It can thus be concluded that the machined surfaces are at least identical to the porous interior of the wick. Not only is there no loss of functionality through machining, but it may in fact improve the functionality of the wick.

4. CONSTRUCTION AND TESTING

4.1. Introduction

Validation of the mathematical model proceeded by verifying its predicted values against empirical values from an experimental LHP. This chapter details the construction of the LHP and additional components such as the heater, heat exchanger and instrumentation. The selection of the working fluid, namely ammonia, is discussed along with the safety precautions taken. Finally, the testing methodology is described, including the procedure to validate the mathematical model and test the LHP with elongated transport lines and in gravity-assisted or gravity-adverse orientations.

4.2. Experimental LHP setup

Apart from its basic sections, the experimental LHP includes additional components which are necessary for operation and testing but which do not affect the physics of the fluid directly: the heat source, charging and venting section, heat exchanger and instrumentation.

4.2.1. Heat source and saddle

The heat source is a flat plate heater which simulates an electronic heat source such as a CPU (Figure 4-1). During testing, the power to the heater can be varied to document the performance of the LHP at a variety of heat inputs. Considering the potential need for a high heat input, the heater is specified to generate 400 W of heat at 230 V. The evaporator is 100 mm long and the final dimensions of the heater are 100 mm by 130 mm. The heater has holes punched into each corner to secure it to the saddle (Figure 4-1).

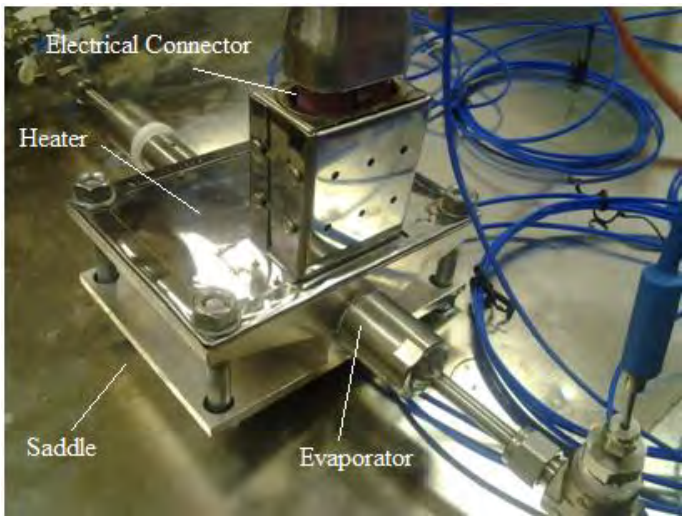

Fig.4-1. The heater, saddle and electrical connector

A sliding voltage regulator is used to vary the power supply to the heater (Figure 4-2).

Fig.4-2. The sliding voltage regulator

The resistance of the heater can be calculated from its maximum power and voltage specifications, and the heat input to the LHP for a particular voltage is calculated.

A saddle, shown in Figure 4-1, is attached between the heat source and evaporator to provide thermal contact. This was machined from aluminium due to its low cost, ready availability and high thermal conductivity (approximately 250 W/mK). The saddle was composed of two halves to allow it to be disassembled and removed. The halves were machined with semicircular grooves down the middle of each to allow the evaporator to be clamped between them. A chamfer was machined into the top half-saddle piece and sections of metal from either side of the central evaporator groove on the bottom half-saddle were removed. These alterations allowed the saddle to act as a thermal wedge, diverting all the heat directly through to the evaporator and ensuring uniformity of the heat load. Holes were machined into the underside of the chamfer for thermocouples. Before assembly, the evaporator, saddle and heater were coated with thermal paste to increase the conductance. The heater and saddle were covered with insulating cloth during operation.

4.2.2. Evaporator

The evaporator is a hollow section of tubing containing the sintered wick. It must have an adequate inner diameter to accommodate the wick and be long enough to fit the entire wick. The evaporator wall thickness must withstand the maximum pressure of the working fluid at its highest working temperature and the material must be compatible with the working fluid. For this latter requirement, 316 stainless steel was chosen for its high corrosion resistance properties.

The inner diameter of the evaporator was machined such that the wick could be inserted with a slight interference fit. The wick has a porosity of 60%, permeability of 6.77×10^{-13} m^2 and estimated pore radius of 1 μm, an outer diameter of 16.5 mm and a length of 80 mm. The evaporator had an inner diameter of a few microns less than 16.5 mm.

A suitable wall thickness was required so that the pressures within the evaporator could be contained. This was important as ammonia is toxic to personnel and has high vapour pressures at high temperatures. That is, saturated anhydrous ammonia at 35 °C has a vapour pressure of 13.508 bar and at 60 °C has a vapour pressure of 26.156 bar. An outer diameter of 20 mm and wall thickness of 1 mm were used. Calculations showed these dimensions can withstand high pressures with a large safety factor and are also in line with similar sized LHP evaporators [8,9,19,23].

After the wick was inserted, a 20 mm void was present in the evaporator to accommodate the difference in evaporator and wick length. Figure 4-3 shows the wick installed in the evaporator and the void. A gap is visible between the wick and the evaporator wall, caused by a misalignment when the wick was inserted. This gap did not present any problems however.

It was found that when the wick was pressed into the evaporator, the slightly smaller diameter of the evaporator shaved off the oversized diameter of the wick, preventing an interference fit from forming. Sealing the wick will be discussed in the analysis of the CC in Section 4.2.3.

Fig.4-3. The wick inserted into the evaporator

Once the wick was inserted, the evaporator was enclosed and the vapour line connected. Welding an end cap onto the evaporator was not possible, therefore a detachable end cap was machined with 22 mm inner diameter threads and the vapour line inlet pipe welded into it, while

the evaporator had corresponding external threads. This end cap was then screwed onto the evaporator once the wick had been installed. The evaporator can be seen in Figure 4-4 and the end cap with the vapour line inlet is shown in Figure 4-5. The CC shares a common envelope with the evaporator.

Fig.4-4. The evaporator and CC with threading

Fig.4-5. The evaporator end cap

4.2.3. Compensation chamber

To ensure contact between the CC and evaporator, they were combined into a continuous section of tubing. An integrated CC is beneficial from a simulation perspective as the model assumes that the heat leak between the evaporator wall and CC wall is conducted along a straight tube (Figure 4-6).

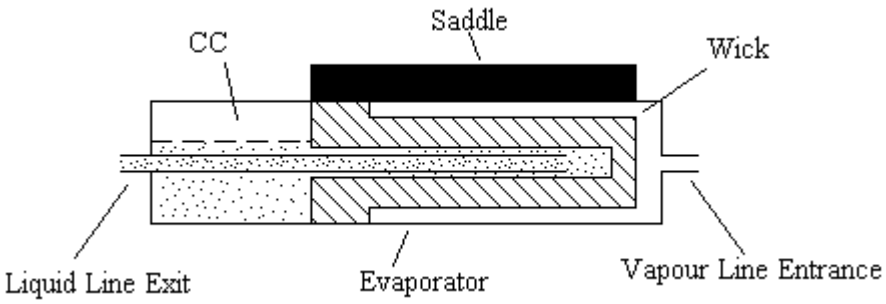

Fig.4-6. The CC as an extension of the evaporator

The CC and evaporator have the same outer and inner diameters of 20 mm and 16.5 mm respectively. The length of the CC is 60 mm. A bayonet was attached to the CC end cap by welding a section of stainless steel tubing through its center. A section of the liquid line was welded to the outside of the end cap. Internal threads were machined 20 mm into the end cap, while the remainder of the cap providing additional volume to the CC. A detachable end cap benefits the experimental LHP because if the CC volume needs to be enlarged, another end cap can be made with a greater additional volume. The CC end cap, bayonet and liquid line exit are shown in Figure 4-7.

Fig.4-7. The compensation chamber end cap with bayonet

The bayonet is 110 mm long and terminated about halfway into the wick core, allowing room for the subcooled liquid to collect in the core before it is drawn through the wick or flows into the remainder of the CC. Since the wick core was 7 mm in diameter, a portion of the bayonet, which was initially 6.35 mm in diameter, was machined down to 4 mm to prevent obstruction to the flow.

A hermetic seal is required between the vapour and saturated sides of the wick in order to prevent superheated vapour from escaping into the CC and radically reducing the cooling ability of the LHP. A hermetic seal is best created by employing a knife-edge seal. This is, however, not feasible due to the frailty of the wick. Instead, an O-ring and silicone are used to form a compression seal around the edge of the wick. This requires that a sleeve be machined which applies the required compressive force on the sealants.

The sleeve was made of ammonia compatible plastic and machined with an outer diameter of 16.5 mm. In order to minimise the reduction in CC volume, the inner diameter is 14 mm. The sleeve fits between the O-ring and the back of the CC end cap, the force on the sleeve as the end cap is screwed onto the CC providing the compression seal.

4.2.4. Vacuuming, charging and venting

The vacuuming, charging and venting station is a branch installed on the liquid line, just before the CC to encourage working fluid to collect there during charging. The branch and fittings can be seen in Figure 4-8.

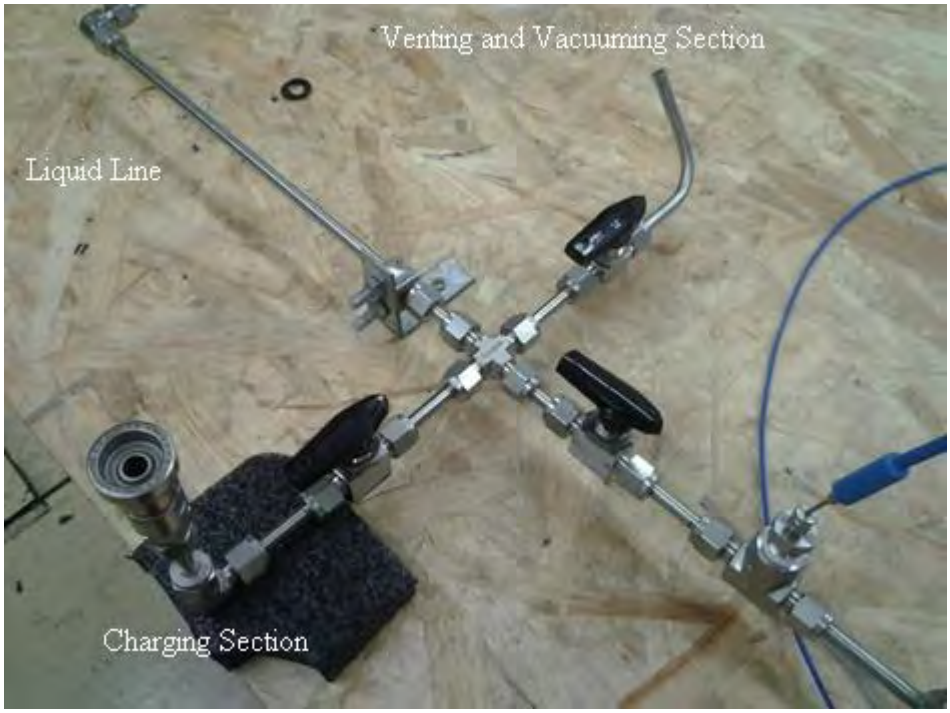

Fig.4-8. The charging and venting station

On the far side of the branch are a ball valve and a short section of piping angled away from the operator. This was used to vacuum the system beforehand and vent the refrigerant to atmosphere when the LHP needed disassembly. Directly opposite the venting and vacuuming section, placed on the accessible side of the liquid line for ease of operation and safety, was a

female quick-connect which was used to charge the system. A ball valve is placed between the branch and the quick-connect as the quick-connect was found to leak if exposed to high internal pressures. The system is charged by first filling and then attaching a charging cylinder with the corresponding male quick-connect, discussed in Section 4.4.2. Figure 4-8 also shows a ball valve on the liquid line between the branch and CC inlet thermocouple. This ball valve was fitted after it was found that venting excess mass from the system this close to the CC resulted in a large pressure drop in the CC which caused the compression seal between the sleeve and the wick to rupture. Should some mass need to be vented during operation, the CC inlet is closed before the venting valve is opened and then reopened to resume operation.

4.2.5. Transport lines

The liquid and vapour lines are constructed out of 6.35 mm outer diameter and 3.05 mm inner diameter piping. LHP devices can support narrow transport lines and 3 mm inner diameter tubing is used to demonstrate this. This piping is unusually thick but was selected for a number of reasons. Large outer diameter piping is able to safely withstand the pressure of the ammonia when it reaches high temperatures and will increase the thermal resistance between the fluid and the atmosphere. This latter point is further aided by the piping being made of 316 stainless steel. The lengths of the transport lines were subject to experimentation and the two sets of lengths which were used to construct experimental LHP layouts are discussed in Section 4.5.2.

The transport lines are fitted between the evaporator/CC and the condenser. The lines are suspended due to the evaporator outlet and CC inlet being raised by the saddle and the condenser being raised by the heat exchanger. To prevent the transport lines from bending and warping under their own weight, a number of brackets are evenly placed along each transport line. The brackets tighten around the lines and are secured to the base platform. Apart from keeping the lines level and secured to the base, the brackets also allow the LHP to be elevated by lifting and tilting the base it is attached to. This was required as one of the parameters being tested in the experimental LHP is its ability to operate in adverse and assisted gravity, accomplished by raising either the evaporator or the condenser above the other.

4.2.6. Condenser and heat exchanger

The condenser is composed of the same tubing used in the transport lines and was 1.25 m in length. In typical LHP applications, the condenser can take many shapes and be cooled by a variety of heat exchangers. However, the condenser and heat exchanger configuration employed here are relatively uncommon.

A popular configuration is for the condenser to be wound into a serpentine shape, with a number of 180° bends, and be attached to a chilled plate [5,9,23]. A drawing of such a condenser is shown in Figure 4-9.

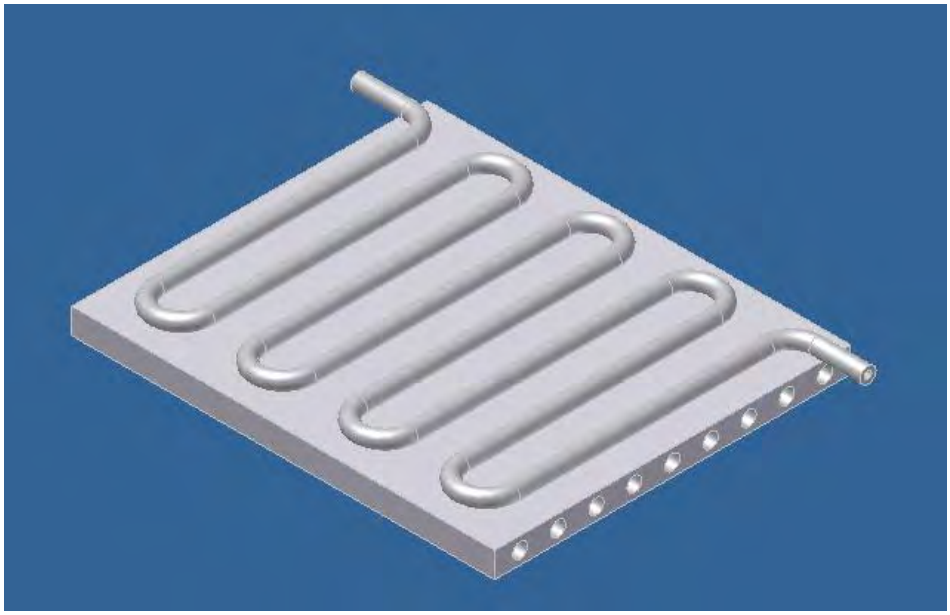

Fig.4-9. Serpentine condenser attached to cold plate

Coiling the condenser into a serpentine shape reduces the space it occupies and is common in practical applications. The cold plate is usually attached to or part of an aluminium block machined with multiple channels through which cold refrigerant is pumped, usually a mixture of glycol and water.

This heat exchanger was rejected for what this study considers a superior and simpler heat exchanger. A tube of flexible plastic hose was wrapped around the condenser, creating a coaxial jacket heat exchanger. Apart from being cheaper and easier to fabricate, the coaxial jacket also permits certain assumptions made in the mathematical modeling of the condenser. The use of a cold plate requires the condenser model take into account that the piping is attached to the plate on one side whilst the remainder of the pipe circumference is open to ambient temperature. This requires calculating the area of the segment of the tube in contact with the plate as well as the thermal resistance of the method by which the condenser is bonded to the plate. Because the cooling channels are spaced and the condenser winds over the surface of the plate, the cooling is also not necessarily uniform and studies which use this method of cooling distribute a number of thermocouples around the plate to determine temperature contours. The condenser in the water jacket, however, is completely surrounded by chilled fluid with a known temperature and flow rate, allowing a simpler and more accurate mathematical representation of the condenser. A drawing of such a heat exchanger is given below in Figure 4-10.

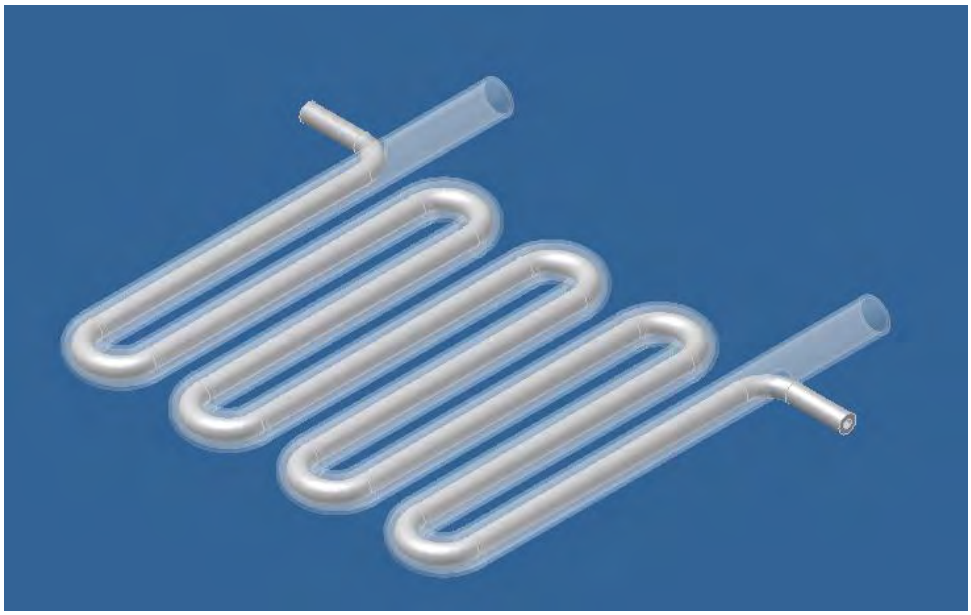

Fig.4-10. Serpentine condenser in coaxial jacket heat exchanger

The coaxial jacket heat exchanger was simplified further by removing all the bends, allowing the tube to be easily fitted over the condenser. A straight condenser is unusual but has advantages pertinent to this research beyond allowing ease of assembly of the coaxial jacket heat exchanger. The mathematical model assumes that the condenser does not have any bends in it. This was done to simplify the mathematics but understood to be a possible discrepancy. Since the condenser in the experimental LHP is a straight section of pipe, this potential discrepancy is removed, allowing for a more accurate simulation of the condenser. The model also does not take into account the effects of gravity in the condenser. If the condenser was bent into a serpentine shape and elevated, gravity would have a significant effect, depending on the orientation of the bends, which would not be simulated and would produce a discrepancy. With the straight pipe condenser, however, gravitational effects are not experienced in the condenser when it is elevated because the fluid is flowing perpendicular to gravity for all experimental scenarios. The condenser in the LHP fabricated in this research is thus a straight section of pipe and it and the jacket can be seen in Figure 4-11.

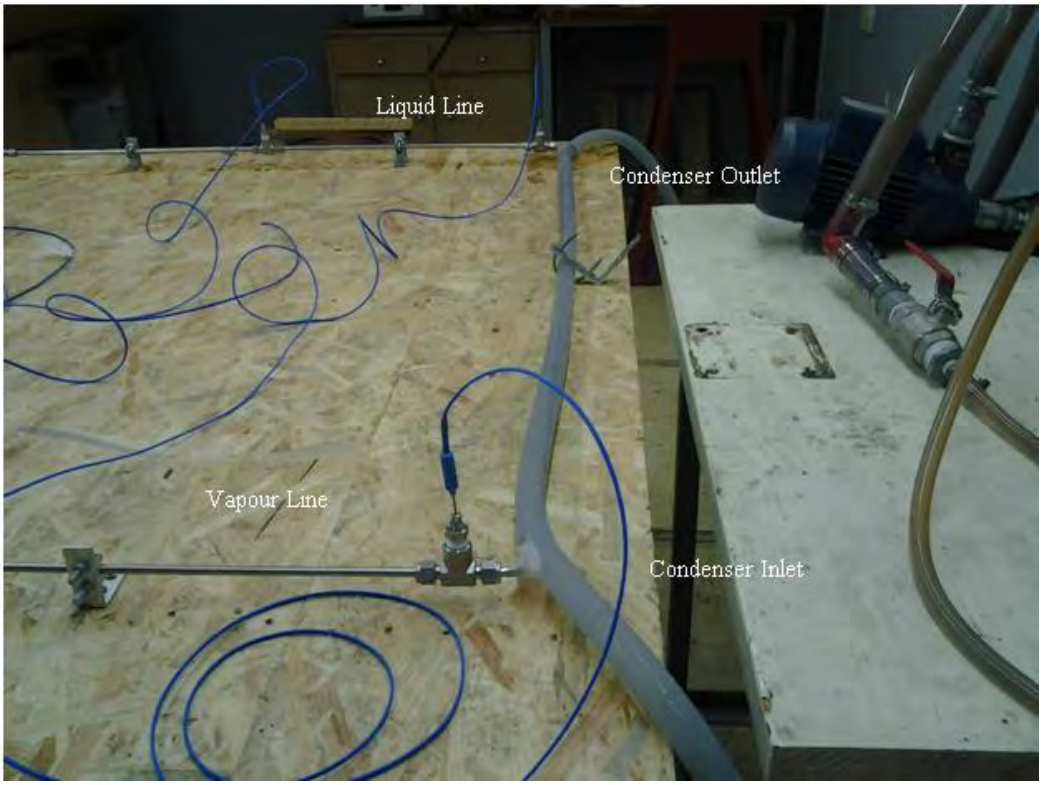

Fig.4-11. The condenser and heat exchanger

The condenser is cooled by pumping ice-chilled water through the coaxial jacket, with the inlet to the heat exchanger positioned at the condenser exit while the outlet is positioned near the condenser entrance, shown in Figure 4-11. This produces a counter-flow heat exchange which improves subcooling near the end of the condenser. The pump which drives the water through the jacket is connected to a reservoir into which ice is periodically placed to maintain a low temperature. The flow rate of the water was measured to be 0.6 *l*/s and the plastic tubing had an inner diameter of 15 mm. The temperature of the ice water was found to be around 8°C, varying by 2°C depending on how often ice was added.

4.3. Instrumentation

The experimental LHP permits the measurement of temperature profiles of the working fluid under steady-state operation and under a number of experimental conditions. The majority of the instrumentation is tasked with determining the temperatures of the fluid at various points throughout the system. There is also additional instrumentation which improves safety and determined the input heat.

A total of eleven type T thermocouples are placed around the system. These points are shown in Figure 4-12. Note that this is the thermocouple distribution for the experimental LHP setup with

long transport lines, discussed in Section 4.5.2. The vapour and liquid line thermocouples (T5 and T8) are not included in the standard LHP.

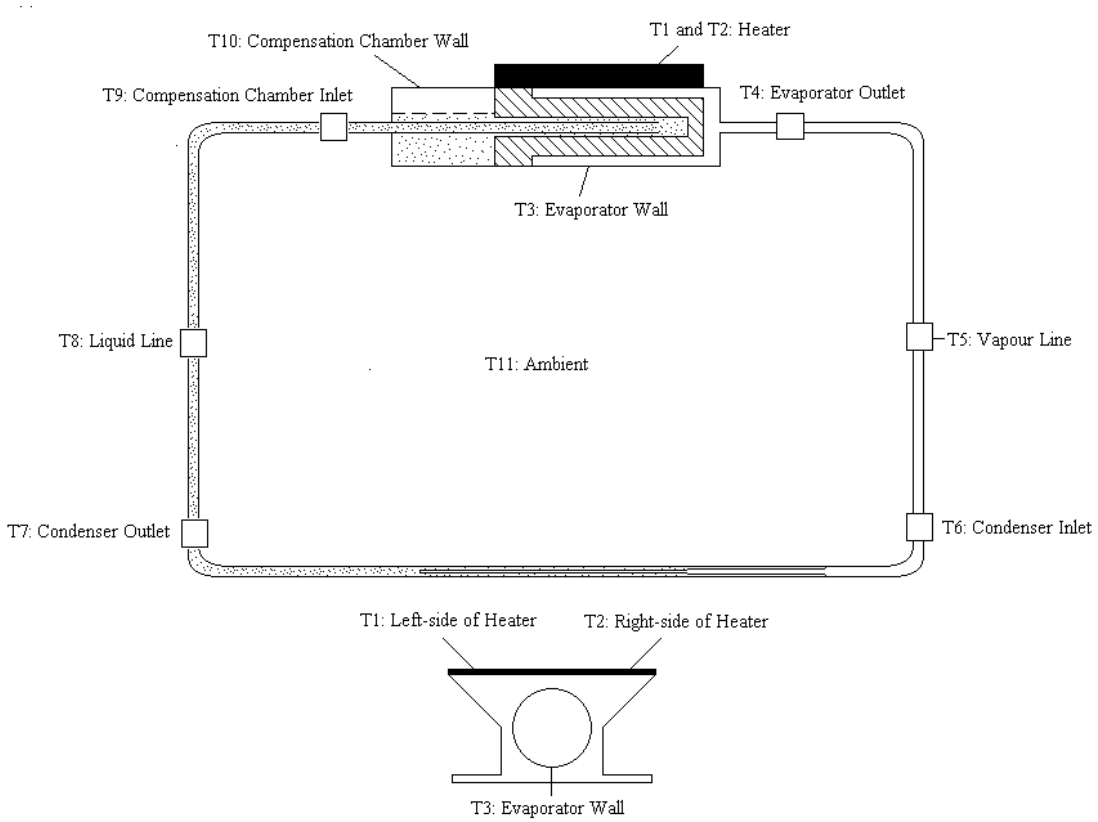

Fig.4-12. Diagram of distribution of thermocouples

Thermocouples T1, T2, T3 and T10 are exposed tip thermocouples attached to the walls and surfaces of the evaporator, CC and heater. No thermocouples intrude into the CC or evaporator. Thermocouples T4 to T9 are placed into the fluid itself by installing tee branches and thermocouple fittings along the loop. These are made with grounded stainless steel sheaths to withstand the corrosive ammonia and their tips extend to the centre of the piping. Thermocouple T11 measures the ambient temperature in the room. All these thermocouples are connected to a National Instruments data acquisition system.

Measurement errors associated with the thermocouples and the National Instruments data acquisition module are combined to determine the uncertainty of the readings. T-type thermocouples between 20°C and 80°C, both shielded and exposed, have a maximum error of 1°C [42]. Between 20°C and 80°C, the data acquisition module has a typical error of 1-1.2°C and a maximum of 2-2.2°C [43]. Combining the two errors, the maximum uncertainty is expected to be approximately 3°C.

Apart from the thermocouples, the system has a pressure gauge installed just after the evaporator outlet. The pressure gauge is shown in Figure 4-13.

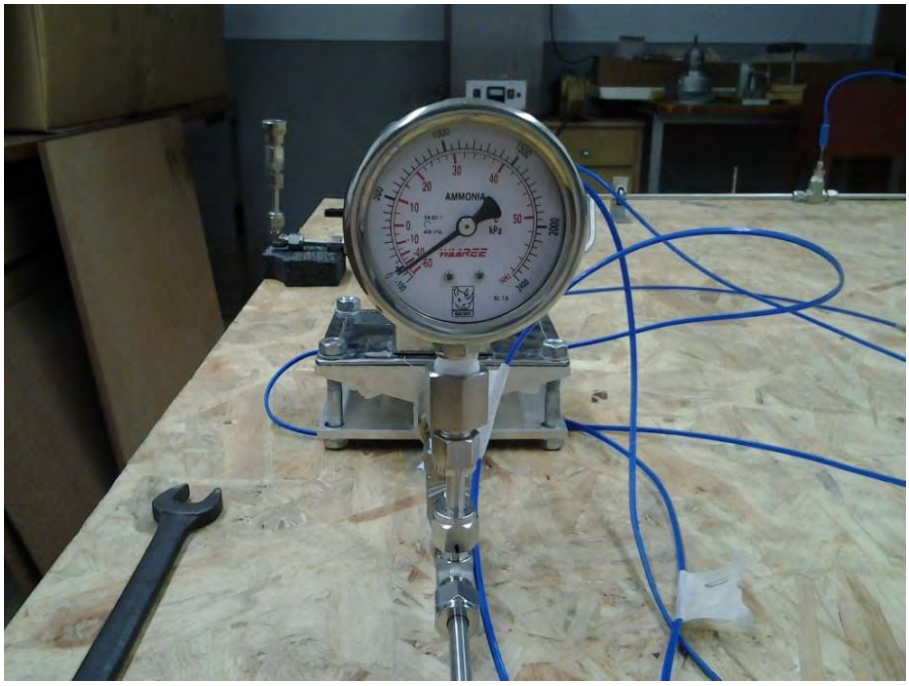

Fig.4-13. Pressure gauge

Since ammonia has high vapour pressures between 35°C and 60°C, a pressure gauge is used to monitor pressure. Although the fluid exiting the evaporator is slightly superheated and the system pressure can be calculated by examining thermocouple T4, the installation of the pressure gauge allows the pressure to be determined directly, which is safer during operation.

The pressure gauge is tailored for use in ammonia systems and has corresponding temperatures for saturated ammonia. This allows the degree of vapour superheating to be determined by comparing T4 with the saturation temperature on the gauge. The instrumentation can also assist in determining if the fluid in the system is at saturation. This is important when charging the system.

A voltmeter is attached to the AC power supply shown in Figure 4-2. This is used to accurately determine the power being delivered to the heat source and allows the heat load to be increased in increments of 10 V during testing.

The data acquisition system is plugged into a computer which runs a LabVIEW application. Temperature readings are recorded once every second and displayed in real-time. This feature allows the visual determination of whether the LHP has reached steady-state. Readings taken for all the thermocouples are written to a spreadsheet for further analysis.

4.4. Working fluid

A number of working fluids can be used in an LHP as long as the materials chosen are compatible with them. Because chemical compatibility is so important, the selection of the working fluid is usually given precedence over other design parameters.

4.4.1. Selection of working fluid

The selection of the working fluid influences material choices in the LHP, such as possible powders for the sintering of the wick and the piping throughout the system. It also affects the operation of the system, with some refrigerants being thermodynamically superior while others may be easier and safer to work with. In this study, six potential refrigerants were considered, namely methanol, ethanol, acetone, water, R134a and ammonia.

One of the hallmarks of a good working fluid is its ability to absorb as much heat as possible, which is reflected by its latent heat of evaporation and specific heat. Since the LHP is a two-phase heat transfer device, a large latent heat of evaporation was sought. Another property which is prioritised is a large change in pressure over change in temperature along the saturation curve of the fluid. This is essential as the CC and evaporator are thermally connected according to the Clausius-Clapeyron relation. Selecting a fluid which minimised the temperature difference across the wick for a large pressure drop in the outer loop will significantly improve the LHP performance. Other properties of interest are the densities of the liquid and vapour as these affected the mass charge required; the thermal conductivity of the liquid as this influences the heat leak through the wick; and the vapour pressure at the highest acceptable temperature as this determines the maximum safety conditions under which the LHP may operate. Properties of the potential working fluids are given in Table 4-1. Note that 60°C is considered a nominal maximum temperature but is sufficiently high to usefully compare the refrigerants. The minimum temperature, 20°C, reflects room temperature. Where not specified, the thermophysical properties are given for saturated fluid at 40°C.

\

Table 4-1. Chemical properties of various refrigerants [44]

	Methanol	Ethanol	Acetone	Water	R134a	Ammonia
Latent Heat of Evaporation (kJ/kg)	1010	905	519	2406	163	1099
Specific Heat of Liquid/Vapour (J/kgK)	2630/ 3955	2757/ 1649	2182/ 1473	4179/ 1455	1498/ 1145	3510/ 4932
Density of Liquid at 60°C/20°C (kg/m^3)	752.79/ 790.93	754.29/ 789.59	744.28/ 790.19	983.16/ 998.16	1053/ 1225	545.24/ 610.2
Density of Vapour at 60°C/20°C (kg/m^3)	0.175/ 1.03	0.798/ 0.1124	2.57/ 0.601	0.13/ 0.017	87.38/ 27.78	20.493/ 6.7025
Thermal Conductivity of Liquid (W/mK)	0.202	0.1663	0.16	0.6306	0.0747	0.4435
Saturation Pressure at 60°C /20°C (bar)	0.84713/ 0.13032	0.471275/ 0.059245	1.1567/ 0.246616	0.1995/ 0.0234	16.82/ 5.71	26.156/ 8.58
Boiling Point at 1.013 bar (°C)	64.482	78.24	56.08	100	-26.07	-33.32

The refrigerants with the highest latent heat of evaporation and specific heat are water, ammonia, methanol and ethanol. These also have the highest liquid thermal conductivity but, since the metallic wick contributes significantly to the heat leak, this is considered secondary. Because the largest pressure drop in the system is in the vapour lines, a high vapour density is important. This consideration singled out ammonia and R134a. The fluids with the largest pressure difference per unit temperature (found by comparing the saturation pressures between 60°C and 20°C) are also found for ammonia and R134a.

Due to its high latent heat of evaporation and large pressure difference per unit temperature, ammonia was the best choice. Auxiliary chemical properties, such as vapour density and specific heat also made ammonia preferable. Ambirajan *et al*. [3] discuss a vapour figure of merit which can be used to determine the best working fluid for a given temperature range. Between -50°C and 100°C, ammonia is the preferred working fluid.

Using ammonia eliminates brass and copper as materials but permits stainless steel and nickel. The most significant disadvantage of ammonia is that it is hazardous, both personally and environmentally.

4.4.2. Charging

A charging cylinder is used to fill the system (Figure 4-14).

Fig.4-14. The charging cylinder

This allows the storage and transportation of anhydrous ammonia. A ball valve is positioned between the cylinder and quick-connect to prevent leaks from the male quick-connect. Above the cylinder is a pressure gauge, charging section and vacuuming section. The charging and vacuuming sections both contain ball valves to close the cylinder once it is charged. The charging section, the long section of piping opposite the hollow storage cylinder, ends with a compression fitting. This is fitted to a regulator attached to a canister of refrigeration-grade ammonia when the vessel is charged. The vacuuming section ends with a short pipe section onto which a vacuum pump can be connected.

The charging cylinder is filled by first connecting the charging section to the ammonia tank with the regulator closed and both ball valves open. A vacuum pump is then connected to the cylinder and a vacuum drawn and held for a few seconds to ensure no air remains in the cylinder and regulator valve. The ball valve on the vacuum section is then closed. Due to the hazardous nature of ammonia, leak checking is necessary and the pressure gauge on the regulator, which can show pressures below zero, is used to see if the vacuum was being held without leaks.

The cylinder is charged by opening the ammonia canister and regulator. To induce liquid ammonia in the charging cylinder, it is first chilled to condense the ammonia vapour. This is done with a small Styrofoam bath which is taped over the storage cylinder. The bath contains methanol and is cooled with liquid nitrogen (Figure 4-15).

Fig.4-15. The charging cylinder with bath

The methanol is frozen by the liquid nitrogen, creating a layer of approximately -98°C ice around the cylinder. After a few minutes exposure to the ice, the cylinder can be filled with approximately 40 g of ammonia. Increased exposure time leads to even greater mass charges, with a maximum of approximately 60 g, although, at this mass, the pressure in the cylinder rises to 16 bar once the cylinder returns to ambient temperature and is not deemed safe.

The charging cylinder is connected to the LHP and the system is evacuated before charging (Figure 4-16).

Fig.4-16. The charging cylinder connected to the charging station

The mass charge can then be introduced by opening the ball valve at the bottom of the charging cylinder and allowing the ammonia to flow into the system. The charging cylinder is then removed by disengaging the quick-connects.

LHP devices are sensitive to working fluid inventory and introducing the correct mass charge was an area of concern in this study. While it was possible to calculate the required mass charge, charging the system with precisely that amount was extremely difficult.

The mass which is introduced is calculated by measuring the weight of the charging cylinder before and after the procedure and finding the difference. If the mass charge is too little, topping up is possible from the cylinder. If the system is overcharged, the excess can be vented out by releasing small masses incrementally. A single, quick vent was found to remove approximately 0.1 g from the LHP. This method allowed a reasonably accurate mass charge to be introduced to the LHP although the precise mass remained unknown.

4.4.3. Venting and safety considerations

Venting the system consists of turning a ball valve and releasing the ammonia to atmosphere. This presents certain hazards to humans, since ammonia is exceptionally hydrophilic, and it will attack any exposed moist areas, which are typically the eyes, mouth, lungs and any open sores or cuts. It then ionises in the moisture creating aqueous ammonia, leading to cell degeneration after long exposure. Interaction with the eyes may cause temporary blindness. Fortunately, ammonia has an extremely pungent odor well below the harmful level, giving personnel ample time to vacate in the case of a leak. These facts were kept in mind whilst experimentation proceeded [45].

During construction, the experimental LHP exhibited leaks through the evaporator and CC end caps. These were stopped by additional thread tape. Leaks were identified by passing a strip of litmus paper over each connection in the system until the source was found.

4.5. Testing

The experimental LHP was used to validate the mathematical model and to investigate performance in various orientations and layouts.

4.5.1. Horizontal operation

Startup and testing followed the following procedure:

1. The LabVIEW data acquisition software was initialised.
2. The condenser pump was started and ice added to its reservoir. Ice is continuously added throughout operation.
3. Once the reservoir began to cool down, the power supply was switched on and set to 30 V, producing a heat load of approximately 6 W.

4. The temperatures of the heat source and evaporator began to rise as startup commenced.
5. Once the source temperature begins to level out, operation is maintained for 30 minutes to achieve steady-state.
6. Once steady-state has been achieved, the power supply is increased by 10 V.
7. Steps 4-6 repeat until the temperature of the system pressure exceeds 18 bar.
8. The power supply and condenser pump are stopped and the insulation around the heater and evaporator removed.
9. Once the test is concluded, the steady-state temperature data are collected and analysed as a function of heat load.

The steady-state analysis for horizontal operation is discussed in Section 5.2.

4.5.2. Transport line length variation

Because of the small pore size expected of the sintered wick, LHP devices can usually develop large pressure heads which allow the fluid in the condenser and lines to be transported great distances while the LHP remains functional. To test this hypothesis, two variations of the layout were constructed with different transport lengths. Only the transport line sections between the elbows and the condenser were altered, producing the following layouts: a standard LHP, in which the liquid and vapour line lengths are 0.655 m and 0.64 m respectively and an elongated LHP in which the liquid and vapour line lengths are 1.396 m and 1.418 m respectively. A front view of the standard LHP is shown in Figure 4-17 while the elongated LHP can be seen in Figures 4-18.

The procedure for testing these layouts is identical to that used in the horizontal operation on the standard layout. Results are compared with each other to identify the effect of transport line variation on overall performance. The findings are reported in Section 5.4.

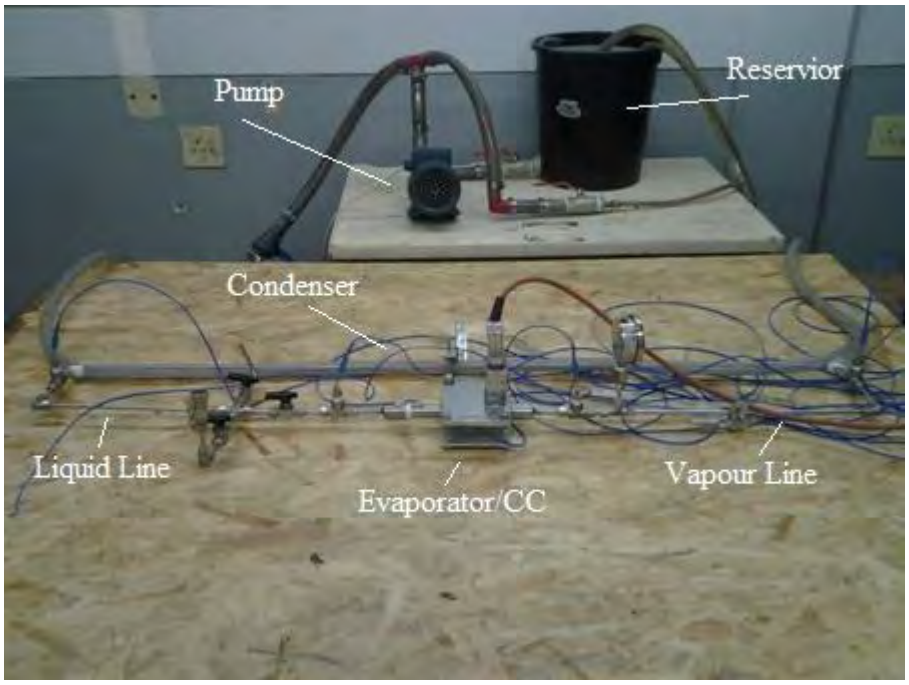

Fig.4-17. The standard LHP

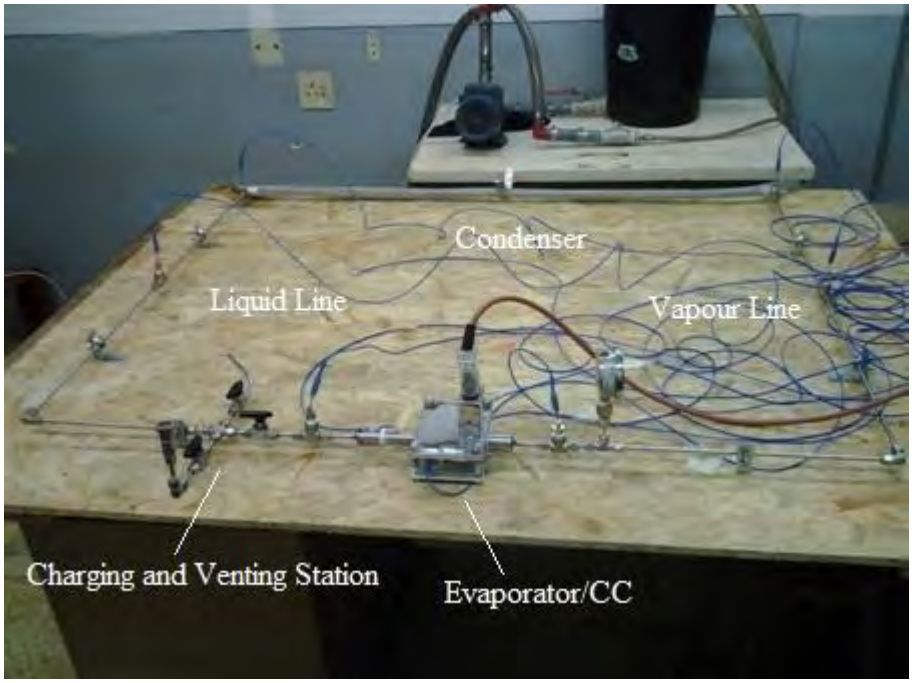

Fig.4-18. The elongated LHP

4.5.3. Gravity-assisted and gravity-adverse operation

Driving pressures in the LHP wick permit the device to operate against gravity. The LHP is placed into a gravity-adverse scenario by raising the evaporator above the condenser, causing the liquid transport line to be negatively affected and increasing the pressure difference required

to complete the loop. This effect is investigated by elevating the evaporator above the condenser at different angles.

In a gravity-assisted position, the condenser is elevated above the evaporator and the performance is expected to increase as the pressure difference required to circulate the fluid is reduced. The two scenarios are represented schematically in Figure 4-19.

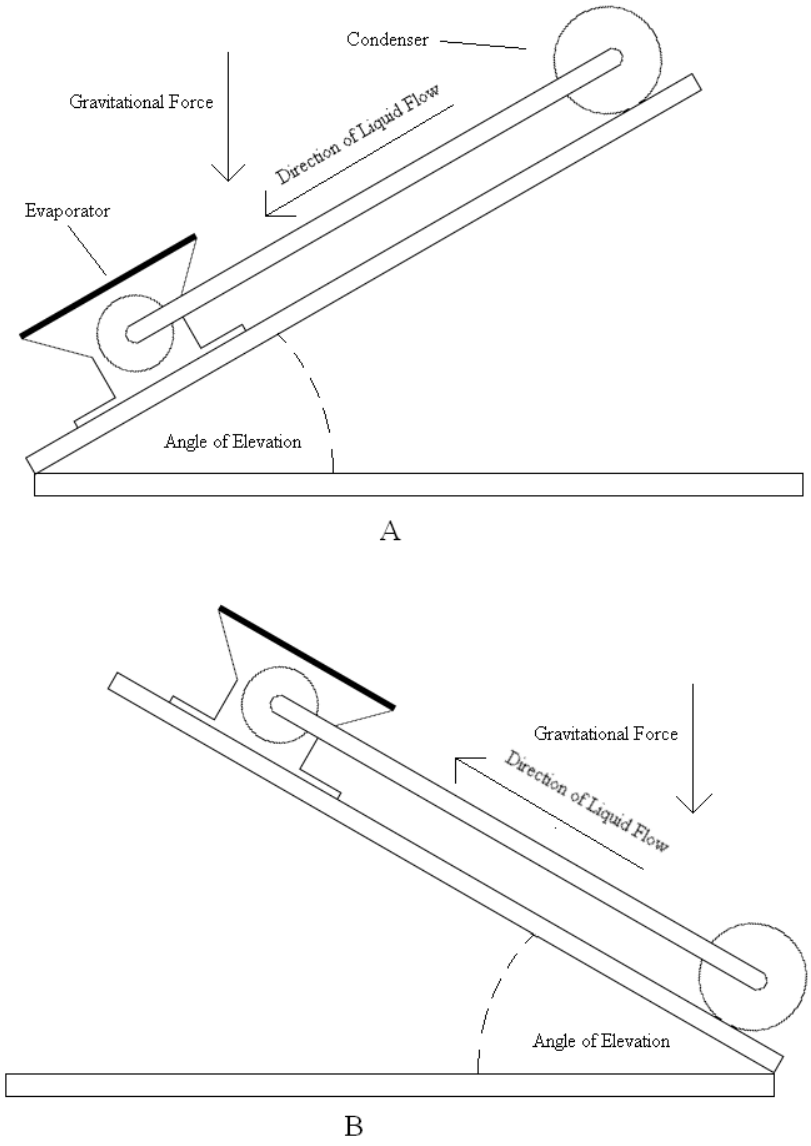

Fig.4-19. Gravity-assisted (A) and gravity-adverse (B) elevations

It is important to note that the LHP is only being varied in elevation, not tilt. In these layouts, tilt is the elevation of one transport line over the other and was not tested because the CC does not contain a secondary wick to ensure liquid contact with the primary wick.

In the elevation experiments, the LHP first achieves steady-state before the platform is elevated. Although the LHP can start in the gravity-assisted position, it tends to fail in the gravitationally adverse orientation, thus requiring that horizontal startup be successfully achieved prior to elevation.

Due to the size of the platform, the angles by which the LHP can be elevated are relatively small. They do, however, reflect the ability of the LHP to operate in gravity-adverse and gravity-assisted positions and permit investigation of the trends which elevation has on thermal performance. Two angles have been investigated: 5° and 10° in both gravitational orientations. These results are discussed in Section 5.5.

5. RESULTS

5.1. Introduction

In this chapter, theoretical temperature profiles are generated using the LHP model and compared with data obtained in experimental testing of the physical device. Shortcomings in the model are described and performance of the LHP under different operating conditions is discussed. The uncertainty of the readings, calculated as a maximum of 3°C, is not overtly mentioned but its presence in all temperature curves is acknowledged.

5.2. Startup analysis

The 6.8 W startup of the standard LHP is shown in Figure 5-1.

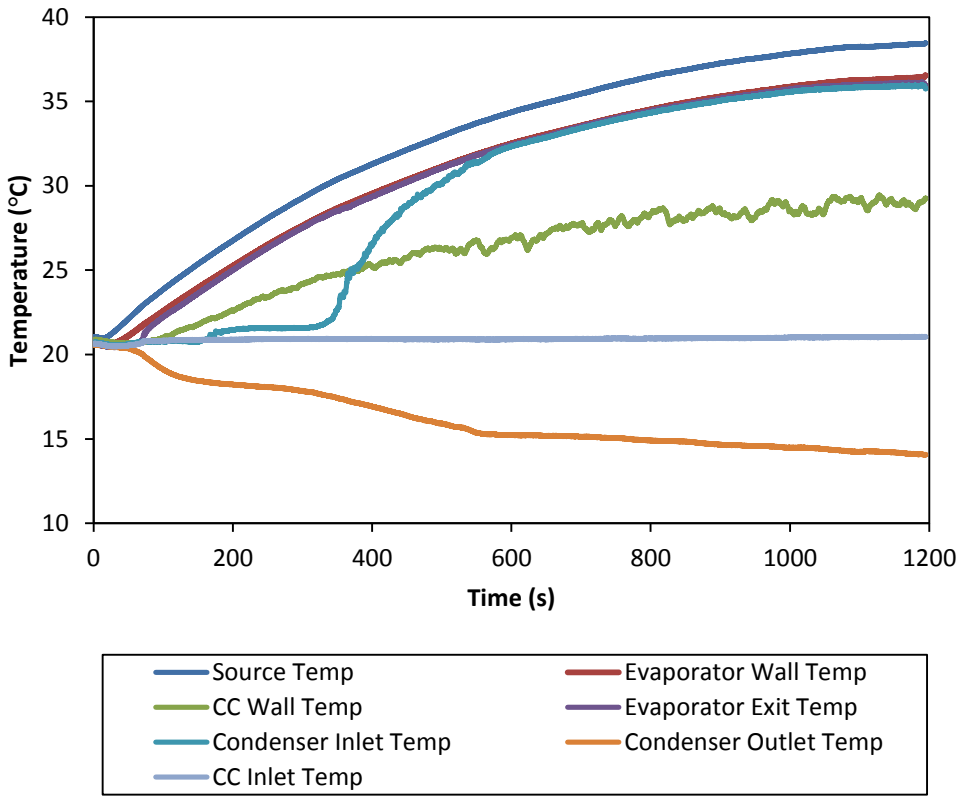

Fig.5-1. Startup of standard LHP at 6.8 W

When the LHP begins startup, the working fluid inventory is evenly distributed throughout the system. This means that there is liquid in the vapour line which must be forced out into the rest of the system. As the LHP begins to heat up, there is first an increase in the source and evaporator wall temperatures. This is followed by the evaporator outlet temperature beginning to rise as saturated vapour enters the line. In Figure 5-1, this can be seen a few seconds into the startup. The vapour temperature increases rapidly until it is just below the evaporator wall

temperature. The vapour continues to expand and fill the line until its interface reaches the condenser inlet, indicated by a sudden increase in the condenser inlet temperature. This can be seen at approximately 200 seconds. The slight rise in the condenser inlet temperature is followed by a rapid increase to the temperature of the vapour, indicating that the vapour line has been cleared of all liquid. The system has achieved successfully startup and is approaching steady-state as the operating temperatures continue increase but begin to level off.

The CC wall temperature rises as the evaporator wall and CC fluid heat it up but also begins to level off. The condenser outlet has a drop in temperature as vapour expands into the vapour line, followed by a steady decrease as the vapour expands through the line, until the vapour interface enters the condenser. This is caused by increasing amounts of subcooled liquid being forced into the liquid line by the expanding vapour. The decrease in condenser outlet temperature becomes much slower thereafter as steady-state approaches.

Startup is not always achieved. Figure 5-2 shows startup failure of the elongated LHP at 12 W.

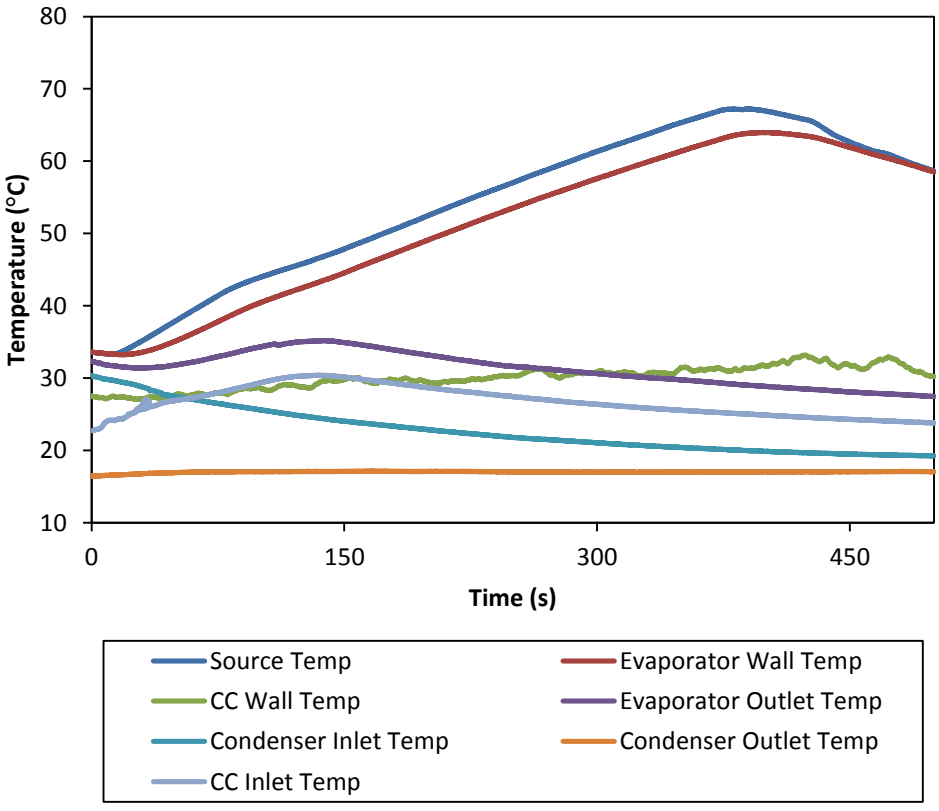

Fig.5-2. Startup failure of elongated LHP at 27 W

In these cases, the heat leak through the wick and low CC inlet subcooling cause the fluid in the CC to heat up and begin boiling. The CC fluid may heat up to the point that the CC inlet

temperature begins to increase rapidly. This can be seen in Figure 5-2. The pressure in the CC increases with temperature and this causes the expansion of the vapour in the line to slow down. The condenser outlet temperature may also level off or increase, indicating reduced circulation. As the pressure on the vapour increases, the vapour interface may begin to recede, characterized by a drop in the condenser inlet temperature. All these events are shown in Figure 5-2.

If the CC inlet temperature rose above the evaporator outlet temperature, the LHP startup would fail. Note that potential startup failure can be identified by the temperature of the evaporator outlet diverging from the evaporator wall while the heat source and evaporator wall temperatures continued to escalate. This is usually found when the system has not yet evacuated the vapour lines and the heat load is too large. It is speculated that this failure is caused by pressure in the CC preventing the vapour region from expanding into the vapour and the vapour being forced into the wick, stalling the system.

It was found that, while the LHP could self-start, the clearance of liquid from the vapour line could be hastened and a reduction of overall startup time could be achieved by artificially cooling the CC. The effects of this are demonstrated in Figure 5-3.

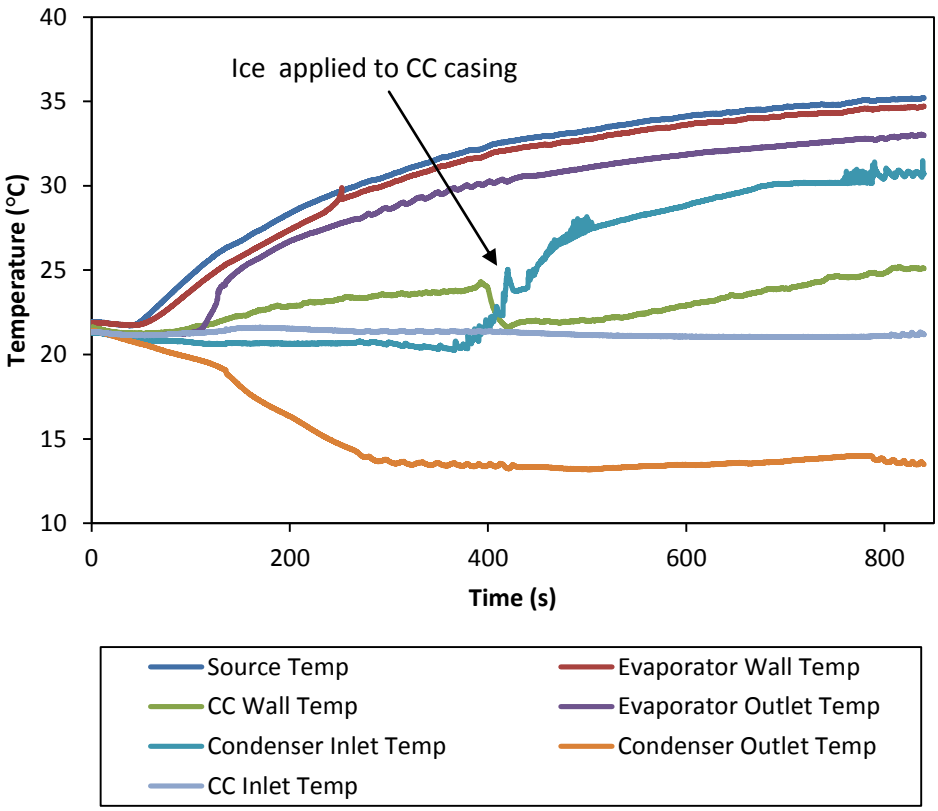

Fig.5-3. Startup of elongated LHP at 12 W

The increased CC fluid temperature, which causes failure, can be reduced by applying cold body, such as ice, to the CC wall. The sudden reduction in CC wall temperature at approximately 400 seconds in Figure 5-2 indicates that ice has been applied. The additional cooling causes the condensation of fluid in the CC, increasing its liquid mass. This draws liquid out of the outer loop, allowing the vapour to rapidly expand through the line and condenser. The vapour interface reaches the condenser inlet almost immediately after the ice is applied, which is indicated by the sudden increase in its temperature.

To confirm that the LHP is functional and working fluid is circulating, the condenser outlet temperature should be low and remain low, demonstrating a continuous supply of subcooling liquid. Despite the LHP functioning, it may not reach steady-state quickly. For instance, the temperatures may very slowly level off. The temperatures could also potentially overshoot the steady-state temperature and then drop, again reaching steady-state over time. It was found that steady-state is usually reached after a lengthy period of 30 minutes or more but LHP devices are not guarantee to reach steady-state and may be prone to small temperature oscillations over time.

5.3. Standard LHP operation at horizontal

The data from the experimental LHP were collated in the form of a profile of the steady-state temperatures of the heat source, evaporator wall, evaporator outlet, condenser inlet, condenser outlet, CC inlet and the CC wall against the heat input. The results of the standard LHP in horizontal operation are given in Figure 5-4.

The results for horizontal testing showed that the LHP produced results consistent with the literature. Figure 5-4 shows an initial decline in temperatures as the LHP operated in its variable conductance mode. At 12 W, the LHP was at its lowest operating temperature, and thereafter, the saddle, evaporator wall and vapour line temperatures began to steadily increase, almost linearly, indicating the constant conductance mode of operation.

The evaporator outlet and condenser inlet temperatures decrease during the variable conductance mode and then increase as the LHP enters the constant conductance mode. Their increase with heat load is much shallower than the evaporator wall and heat source temperature. Extrapolating these curves indicates that if the experimental safety limit attached to the vapour pressure was increased to 60°C, the LHP would reach its maximum permissible heat source temperature of 100°C at a heat load of approximately 200 W. This does not, however, account for the large temperature overshoot before steady-state, which was the true limiting factor in the experiments.

The effect of the saddle on overall performance is pronounced, with a temperature difference between the heat source and evaporator wall of 6°C at the 61W heat load. The thermal resistance of the saddle should be minimised to reduce the overall thermal resistance of the LHP. Attempts to reduce the effects of the saddle are worth pursuing [12,13,14] although this study was not concerned with the component.

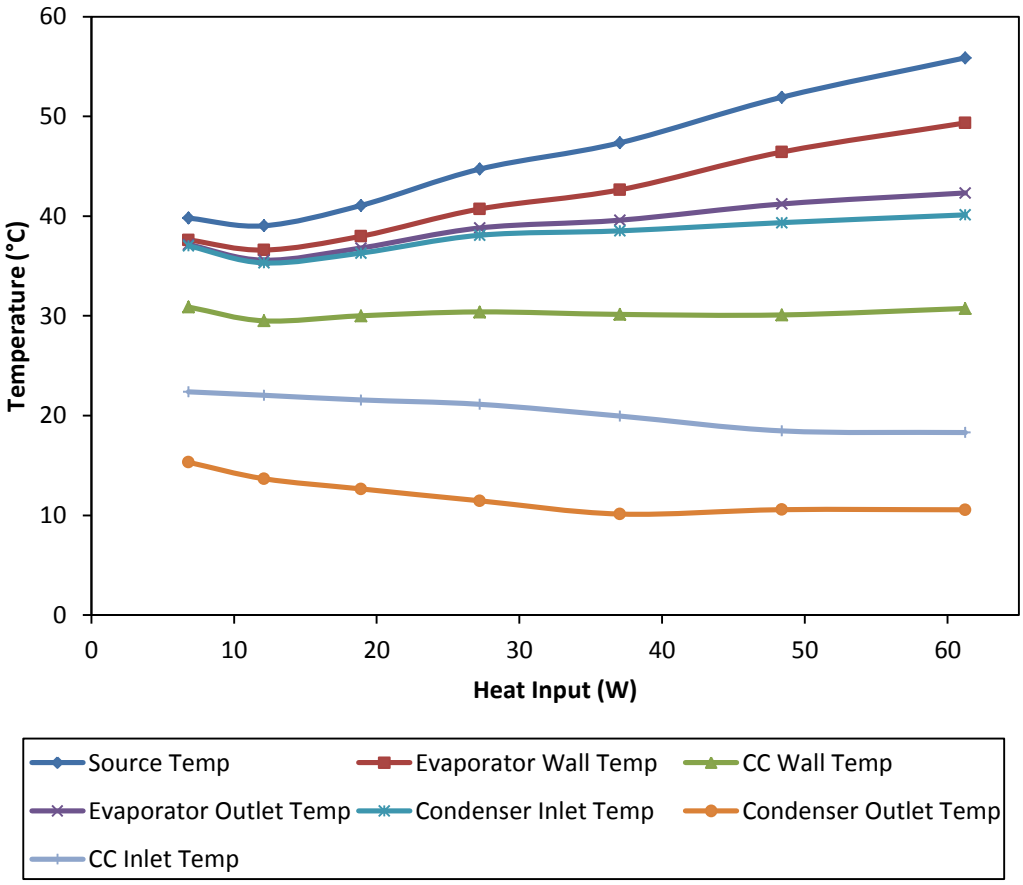

Fig.5-4. Experimental temperature profile for horizontal standard LHP under steady-state conditions

At low heat loads, the evaporator outlet and condenser inlet are similar, with a temperature drop along the vapour line of only a fraction of a degree. Their temperatures increasingly diverge with increasing heat loads, with a difference of approximately 2°C at 61 W. This behavior is the result of the evaporator applying greater superheating to the vapour and the tendency of the vapour to begin condensing very shortly after it enters the transport line.

Condensation is thought to occur along the vapour lines but this was unconfirmed until the elongated LHP was tested. The vapour line of the elongated LHP has three thermocouples installed on it: one at the evaporator exit, one at the condenser inlet and one placed approximately two-thirds of the way along the vapour line. At low heat loads, the temperatures

of all three thermocouples were similar. As the heat load increased, a divergence began to appear between the evaporator exit and condenser inlet temperatures, similar to that shown in Figure 5-4. However, the thermocouple placed along the vapour line was found to have the same temperature as the condenser inlet, even with a temperature difference between the evaporator outlet and condenser inlet of 5°C. This indicates that a portion of the vapour line was isothermal and that condensation must be occurring there. The impact of condensation is that the temperature of the condenser inlet is actually the saturation temperature of the vapour. This also implies that the void in the evaporator allows additional heating of the already superheated vapour leaving the vapour grooves. The degree of the superheating was found by comparing the temperature of the vapour leaving the evaporator with the saturated temperature of the vapour found at the condenser inlet.

This has two immediate consequences for the mathematical model. First, the thermal conductance of the evaporator, G_{ev}, is found empirically by dividing the heat load by the temperature difference between the evaporator wall and saturated vapour. Usually, the saturation temperature is taken as that of the vapour leaving the evaporator, since additional superheating is not considered [23,25]. These observations, however, indicate that additional superheating does occur and that the actual saturation temperature is that of the condenser inlet. This value must be used instead of the evaporator outlet temperature when calculating G_{ev}. Secondly, the mathematical model did not incorporate the additional superheating of the vapour. Since this superheat is found to be around 1W, it will influence the energy balance across the CC.

The condenser outlet and CC inlet temperature curve run parallel and their difference suggests that the liquid experiences a significant temperature increase due to its thermal contact with ambient air. While the temperatures of the heat source and evaporator decreased and then increase, the temperatures of the condenser outlet and CC inlet only decreased. This is due to steadily decreasing heat exchanger temperatures and greater mass flow rates which allow the liquid to become more subcooled and reject less heat.

Overall, the maximum heat load the LHP was able to achieve was lower than anticipated and the operating temperatures were higher than expected. As a terrestrial heat transfer device for electronics, the LHP performed poorly as it was not able to safely and reliably dissipate 100 W of heat typically expected of high-heat flux electronics. The pressure of the vapour was high and limited the maximum heat load, rather than the heat load being limited by the maximum permissible source temperature which would occur in an actual application. Despite this, the LHP nevertheless performed as a two-phase device, as illustrated by the LHP overall thermal resistance shown in Figure 5-5.

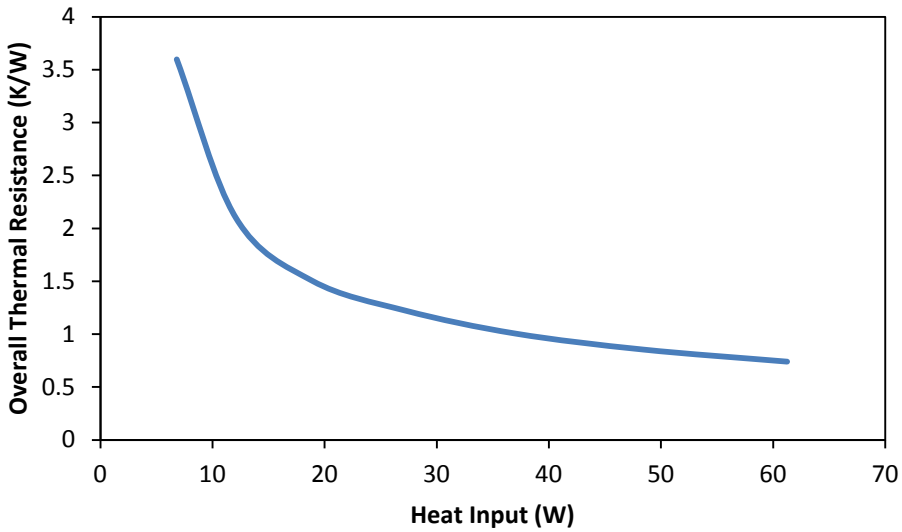

Fig.5-5. The overall thermal resistance of the LHP

Even though this thermal resistance was greater than other similarly sized LHP designs, which are usually in the region of 0.1 to 0.3 K/W at heat loads of upwards of 100 W [11,15,20], this can be attributed to the large thermal resistance of the saddle and the relatively small heat load range applied to the LHP.

5.4. Model results and validation

The model was developed for two reasons: firstly, to simulate the experimental LHP as accurately as possible, and secondly, to function as a design tool. In practice, the model develops two possible temperature profiles for a given heat load, giving a possible range within which the correct temperature profile may exist. It then generates data for both the variable and constant conductance mode of operation and the experimental results are compared to the possible range of operational temperatures.

A few aspects of the experimental LHP are unique to each heat load, which means that the model must be adjusted to properly reflect the experimental LHP data. These amendments to the model are listed here.

1. A variable heat sink temperature was employed as the sink temperature has a significant impact on the operation of the LHP and the model could not afford to maintain a single sink temperature for all heat loads.
2. The thermal resistance of the liquid line was lowered to correctly reflect temperature changes as a function of heat load. The mathematical model was found to predict smaller temperature drops along the liquid line than the experimental LHP experienced.

This is thought to be due to the model not anticipating the heat transfer caused by condensation of water on the line. Because the CC inlet temperature affects the energy balance across the CC, an inaccurate simulation of it would seriously influence the modeling.

3. The calculated thermal resistance of the saddle was found to be inaccurate and was replaced with an empirical value. The cause is likely the imperfect thermal contact between the heater, saddle and evaporator wall.

The model also had two amendments which were in disagreement with empirical data but which were made to support the modeling aim of reducing reliance on experimental data.

4. The thermal conductance of the evaporator, G_{ev}, had to be found empirically. The calculated value for each heat load is shown in Table 5-1. This data illustrates that the thermal conductance is not, in fact, independent of heat load. However, a central aim of the model is to avoid reliance on empirical data, specifically in determining thermal conductances in the evaporator. Thus, to maintain this goal, the model used the averaged G_{ev} value of 9.13 W/K for all heat loads.

Table 5-1. G_{ev} versus heat load

Heat Load (W)	6.8	12.1	18.9	27.2	37.1	48.4	61.2
G_{ev} (W/K)	11.4	9.4	11.1	10	8.4	6.8	6.6

5. The superheating of the vapour was neglected because it would be specific to each heat load and would transgress the goal of reducing empirical reliance in the model.

The model was adjusted to reflect all the preceding concerns, as summarized in Table 5-2.

Table 5-2. Adjustments to model

Heat Load (W)	6.8	12.1	18.9	27.2	37.1	48.4	61.2
Heat Sink Temperature (°C)	15	13	12	11	10	10	10
Coefficient on outer thermal resistance on liquid line	0.5	0.5	0.5	0.4	0.4	0.3	0.3
G_{sad} (W/K)	3.11	4.97	6.12	6.81	7.86	8.81	9.38
G_{ev} (W/K)	9.13	9.13	9.13	9.13	9.13	9.13	9.13
Superheating (°C)	0	0	0	0	0	0	0

With these amendments to the model, Figure 5-6 shows the simulated maximum and minimum temperatures for each heat input.

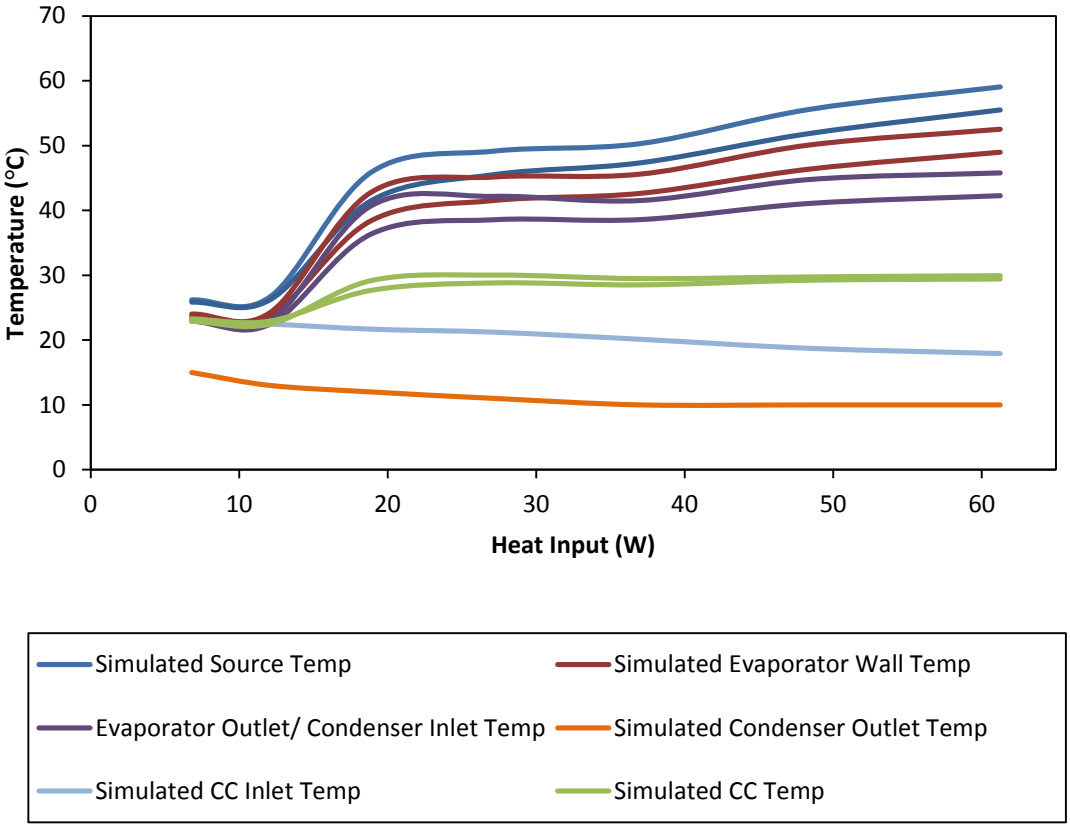

Fig.5-6. Theoretical temperature profile for horizontal standard LHP under steady-state conditions

The evaporator outlet and condenser inlet temperatures curves are combined because the condensation of vapour results in a largely constant temperature throughout the line. The CC wall temperature is not included but would be approximately equal to either the evaporator wall or CC fluid temperatures in accordance with the solution algorithm. The condenser outlet and CC inlet were approximately constant for both the maximum and minimum operating temperatures and thus only a single curve for each is shown.

The consequences of the lack of superheat and a single G_{ev} value for all heat loads were investigated by comparing simulation results for the 61 W heat load. This was a comparison of the range of operating temperatures which the model would produce between four model variants: the pure model; the pure model which has a superheat of 2°C; the pure model with the correct G_{ev} value; and the model with both the superheat and correct G_{ev} value. The comparison is shown in Figure 5-7 below. Only the temperatures of the heat source, evaporator wall,

evaporator outlet and condenser inlet are shown because the remainder of the temperatures remained fairly constant. Only the maximum temperature range is shown since the minimum temperature range producing identical trends.

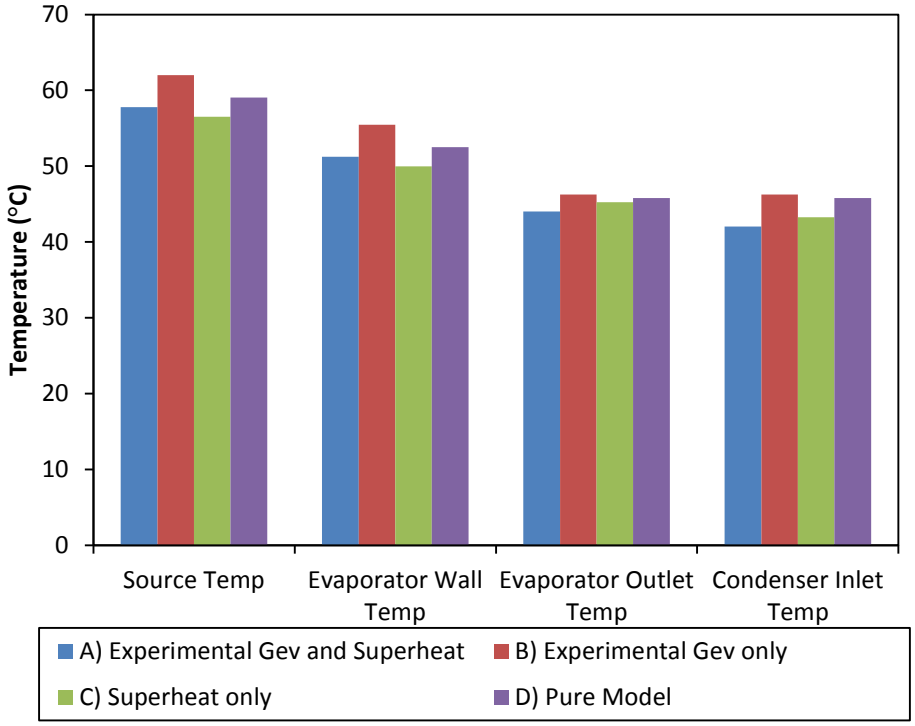

Fig.5-7. Model variant comparison for 61 W

In Figure 5-7, the model variation A has a much lower range than any other variant and, by virtue of the amendments to the model, can be considered the most accurate. If the LHP is modelled with variant C, its range of potential temperatures decreases but the temperatures of the heat source and evaporator wall are below that of A, which suggests it is inaccurate. The model variant B has an increased temperature range, with a large temperature difference between it and variant A for the heat source and evaporator wall. Variant D has a larger range than variant A but not as large a range as variant B. The discrepancy in variant D is the condenser inlet temperature which is a few degrees higher than variant A because of the lack of superheat. Nevertheless, variant D is the more agreeable than either individual amendment and is a fair compromise on the empirical model.

To compare the model solutions and the experimental data, they have been combined in Figure 5-8.

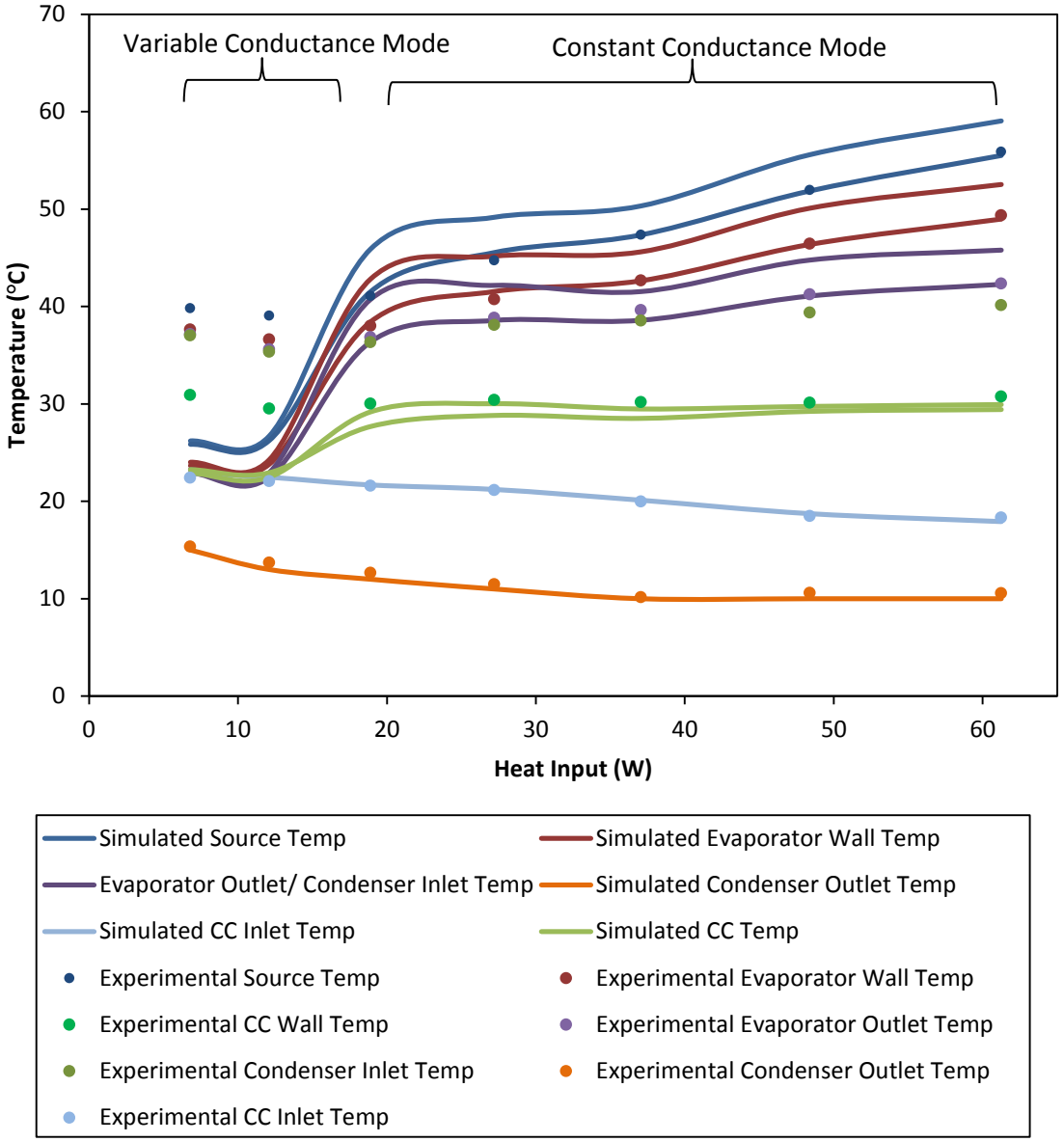

Fig.5-8. Comparison of theoretical and experimental data

From Figure 5-8, model behaviour can be divided into the variable conductance mode and the constant conductance mode. It is apparent that the model does not simulate the variable conductance mode accurately, most likely because of the lack of the two-phase portion of the heat leak through the wick. It was found that as the model increased the amount of heat rejected to the CC, the results became progressively closer to the physical data. An additional heat leak of between 0.4 W and 0.6 W would significantly improve the results of the variable conductance region. However, since the two-phase heat leak through the wick was not included in the model, this inaccuracy is a serious shortcoming.

The constant conductance region is significantly more accurate. Most data points between 18.9 W and 61 W fall within the temperature range of interest while those outside of the range are

very close to the low temperature curve. The exception to this is the condenser inlet, due to the lack of additional superheating and almost immediate condensation of the vapour in the line.

A problem with the simulated data is the large temperature difference between the high and low temperature curves. The heat source temperature, for example, varies by approximately 5°C at 61 W. The experimental data approximates closely with the low temperature curves, which suggests that the higher temperature range could be neglected if further studies were to use this model. The high temperature range should be included, however, as it increases the accuracy of the model by accommodating the measurement errors which may have lowered the experimental temperatures.

Despite the accuracy of the constant conductance simulation, the model was found to be sensitive to the working fluid inventory, with a change of 0.01 g to the mass charge causing the simulated results to radically increase or decrease. For example, the heat source temperature changes by approximately 0.3°C per 0.01 g change to the mass charge. This is problematic as the calculation of the mass in the system is approximate. Possible errors in mass calculation include the incorrect assessment of volumes of the transport lines and the various fittings along them; incorrect simulation of the densities of the fluid in the instrumentation portions of the transport lines; the incorrect calculation of the volume of the CC as well as the possibility of density variation within the CC; and the degree by which the resistance of the natural convective heat exchange in the liquid line is reduced. The void fraction calculation was found to be sensitive to the resolution of the incremental modeling of the transport lines and condenser. An increment of 0.0001 m was found to produce a void fraction which was similar to that found using smaller increments but significantly increased the simulation time. A 0.001 m increment was used as it allowed the simulation to complete rapidly but introduced further void fraction errors. However, the most influential contributor to errors is the void fraction correlation since it directly influences the rate at which the vapour condenses and thus the liquid and vapour mass distributions within each increment, as well as the overall length of the two-phase region. To bypass the sensitivity of the model to the mass charge and the inaccuracies of the void fraction correlation, the model allows the mass charge to deviate by 1%.

The feasibility of the model as a design tool can be determined. Figure 5-7 shows that the assumption of a single, constant evaporator thermal conductance and discounting superheating of the vapour can work in tandem to improve simulated results. The generation of a range of possible operational temperatures is also useful, demonstrating that the need to empirically determine the unknown thermal conductances around the CC is unnecessary. This, however, is only valid for the constant conductance mode of operation. The lack of the two-phase heat

transfer means that attempts to predict the operating temperatures during the variable conductance mode are beyond the capabilities of the model.

Results suggest that the model is rather inadequate as a design tool for the constant conductance mode of operation as well. It requires a reduction of the natural convective thermal resistance in the liquid line which varies with heat load, and the analytical calculation of the thermal conductance of the saddle is inaccurate. In addition, the sensitivity of the model to mass charge and the unresolved calculation of an accurate void fraction mean that the model is inherently tied to this particular LHP, limiting its use as a generic design tool at present. Nevertheless, it has value in shedding light on the general performance of LHPs and their modes of operation.

5.5. Transport line length variation

The temperature profile of the standard LHP is given in Figure 5-4 and the temperature profile of the elongated LHP is given in Figure 5-9.

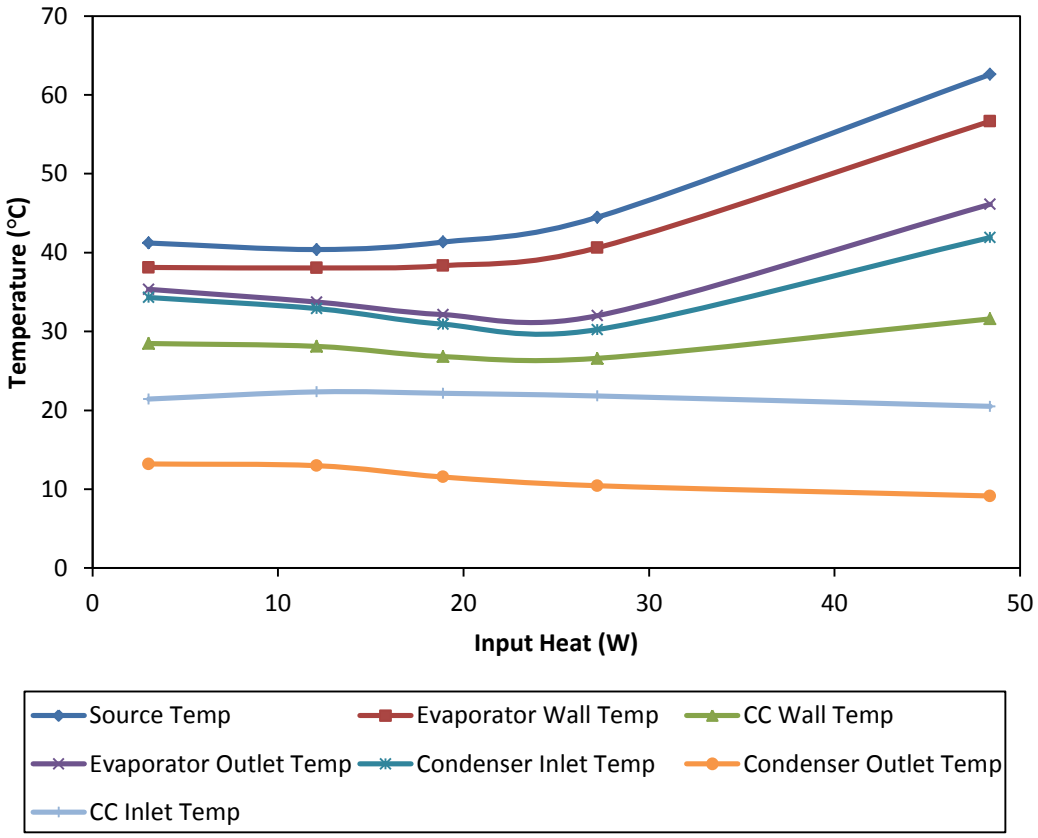

Fig.5-9. Temperature profile for elongated LHP

A notable strength of LHP and a common reason for their employment is their ability to support very large transport and condenser lengths of up to a few metres. Performance depends on orientation relative to gravity, the number of bends in the layout and the pore radius of the wick.

The wick manufactured in this study is estimated to produce a capillary head of 37.7 kPa, thus a LHP was constructed with an approximately 4 m long outer loop and its performance compared to the standard LHP which had an outer loop of only 2.5 m. Figure 5-9 shows the temperature profile of the elongated device, with the expected variable conductance mode of operation followed by the constant conductance mode. Superheating, condensation in the vapour line and a steady decrease in the condenser outlet and CC inlet are also present. The differences between the standard and elongated LHPs are shown by comparing each temperature curve individually. Graphs comparing the values of each significant temperature reading for these two LHP are shown in Figures 5-10, 5-11 and 5-12, with associated sections of the LHP grouped together.

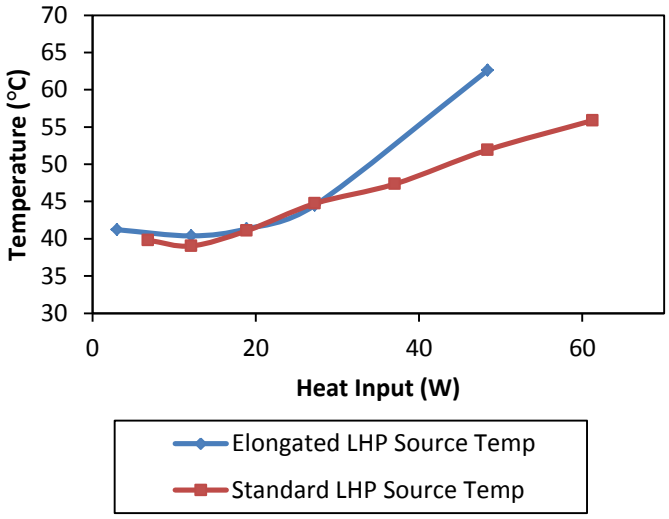

(a)

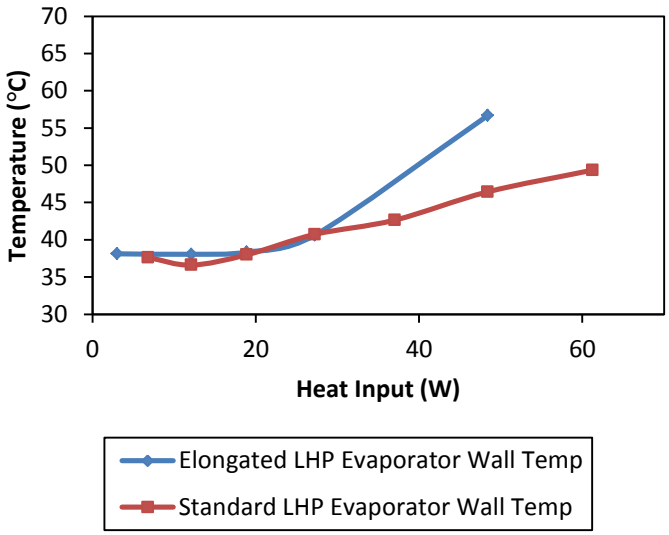

(b)

Fig.5-10. Temperature profiles of the elongated and standard LHP for the heat source (a) and evaporator wall (b)

The heat source temperature is a useful comparative metric between two LHP as it reflects how well the systems would cool a potential electronic device. The graphs in Figure 5-10 show that at low heat loads, for 3 W to 27.2 W, the heat source and evaporator wall for the two LHP had similar temperatures. As the heat load increases beyond 27.2 W, the temperatures diverge rapidly, with the temperatures of the elongated LHP larger than the standard LHP. This is further explained by the data in Figures 5-11 and 5-12.

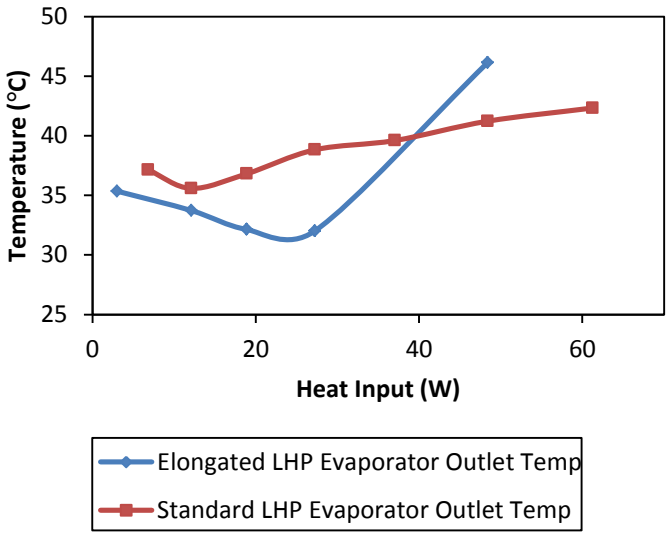

(a)

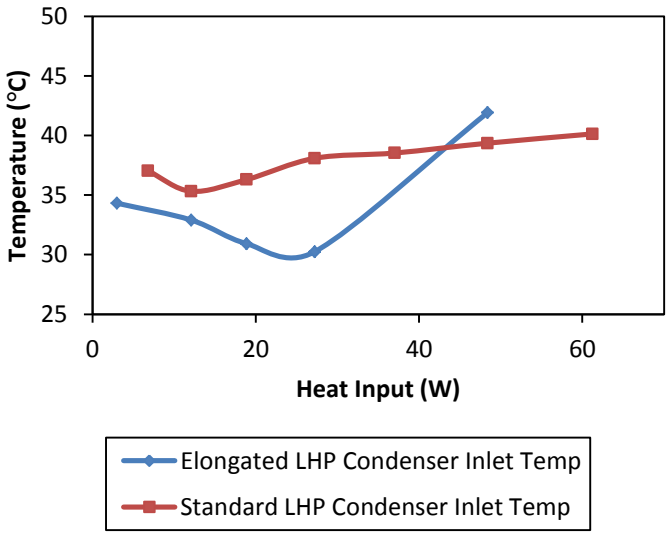

(b)

Fig.5-11. Temperature profiles of the elongated and standard LHP for the evaporator outlet (a) and condenser inlet (b)

In Figure 5-11, the transition between the variable conductance and constant conductance mode of operation is shown in more detail than in Figure 5-9. The elongated LHP transitions at a

lower temperature and at a higher heat load than the standard LHP. This is due to difficulties in the introduction of a comparable mass to both LHP layouts. The mass charge in the elongated LHP allows a larger void fraction to exist in the CC at low heat loads, which in turn allows the CC to flood at a larger heat load and at lower operating temperatures. If the standard LHP had been charged such that both layouts had the similar CC void fractions, the initial operating temperatures in Figure 5-4 would be lower and the transition point would occur at a higher heat input and a lower temperature.

In Figure 5-10, the temperatures of the heat source and evaporator wall for the standard LHP during low heat loads decrease past the temperatures of the elongated LHP. It is then understood that the longer the transport lines, the higher the operating temperatures during the variable and constant conductance mode of operation, although this cannot be shown conclusively.

Another difference between the standard and elongated LHP is the maximum heat load. Figure 5-11 shows that the increase in saturation temperature of the vapour for the elongated LHP is much sharper than the standard LHP which reduces the maximum safe operating heat load for the elongated LHP to only 50 W, while the standard LHP can safely operate up to 60 W. This could be even higher if less mass was present in the standard LHP. Thus the shorter the transport lines, the larger the possible operating heat load range.

One of the most significant differences between the standard LHP and the elongated LHP comes from analyzing the liquid line. Figure 5-12 shows the condenser outlet temperature, which indicates the degree of initial subcooling of the liquid, and the CC inlet temperature, which indicates how much subcooling has been lost and how much the CC fluid is being cooled. The temperatures of the condenser outlet for both layouts are comparable. However, because the liquid line is much longer in the elongated LHP than the standard LHP, the liquid undergoes a larger temperature increase. Consequently, the fluid which eventually enters the CC in the elongated LHP has a larger temperature than that of the standard LHP, which becomes increasingly pronounced as the heat load increases. This greatly influences the performance of the LHP as lower incoming liquid temperatures cool the CC fluid and reduce the operating temperatures. This explains the steep increase in heat source temperature in the elongated LHP compared to the standard LHP during constant conductance.

It can be concluded that increasing the transport lines of an LHP impedes its overall performance but the LHP does remain functional, albeit at higher temperatures and over a shorter heat input range. This can be overcome by designing the LHP with a greater CC volume, which would extend the variable conductance mode and thus increase the heat input range or shortening and insulating the liquid line to retain subcooling.

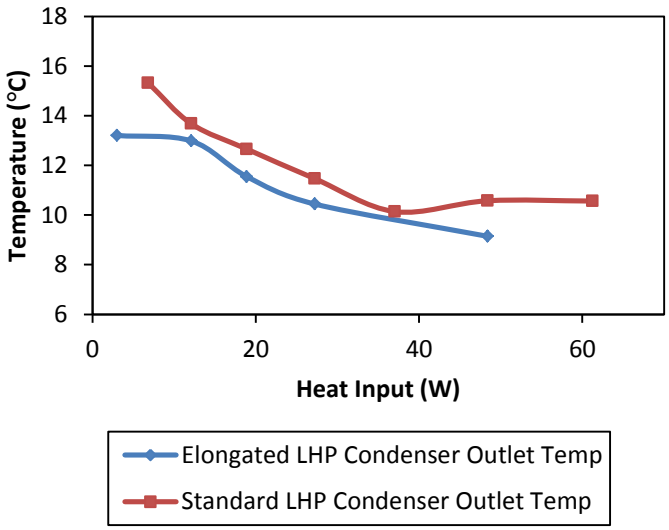

(a)

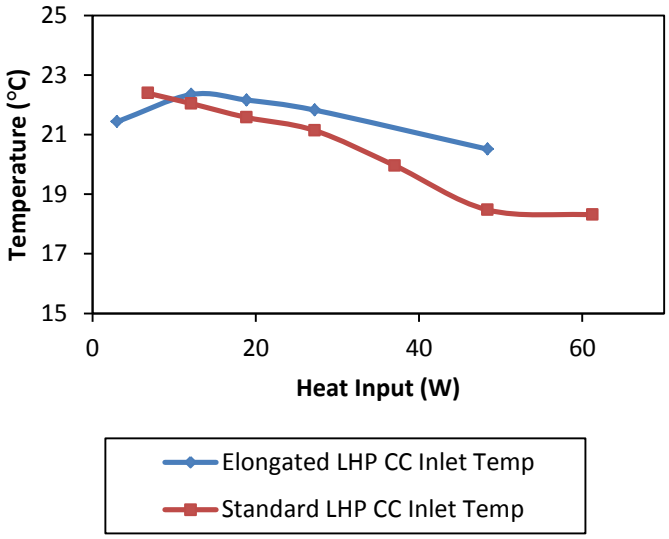

(b)

Fig.5-12. Temperature profiles of the elongated and standard LHP for the condenser outlet (a) and CC inlet (b)

5.6. Gravity-adverse and gravity-assisted operation

An advantage of LHPs is their ability to maintain operation against gravity. The performance of the standard LHP under two gravity-adverse regimes of 5° and 10° is compared to the normal, horizontal operation. It is understood that inclining the LHP such that gravity assists in its operation greatly improves its performance. Thus two gravity-assisted regimes of 5° and 10° are also compared to normal horizontal operation.

5.6.1. Gravity-adverse operation

The temperature profiles of the 5° and 10° gravitationally adverse LHP operations are shown in Figure 5-13 and Figure 5-14 respectively.

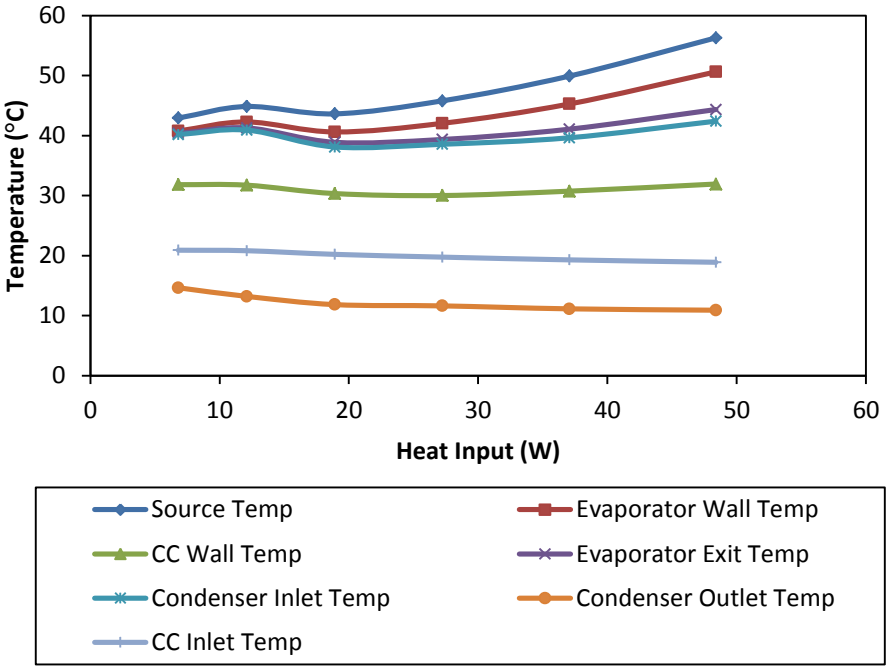

Fig.5-13. Temperature profile of 5° gravity-adverse elevation

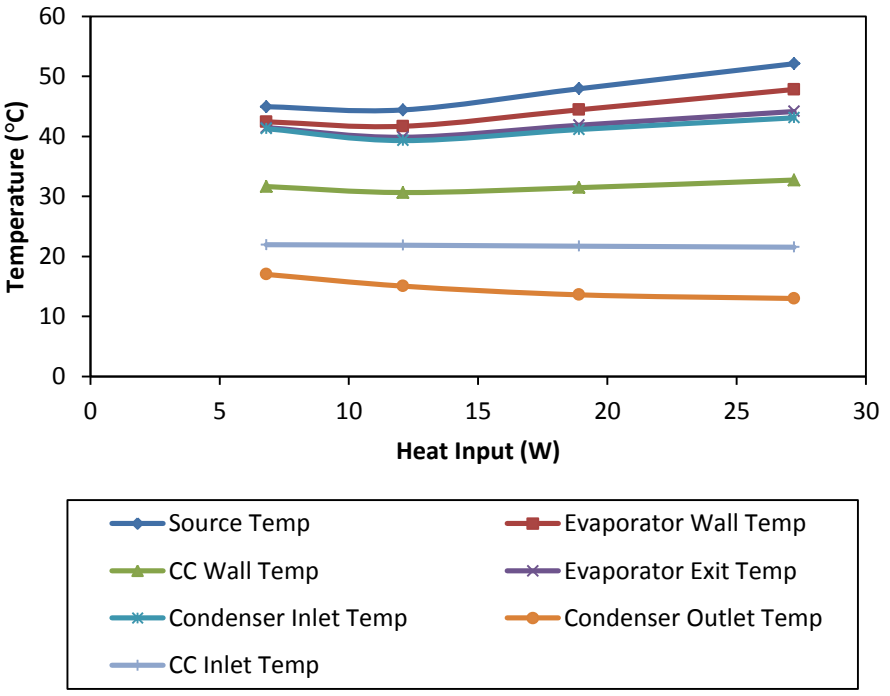

Fig.5-14. Temperature profile of 10° gravity-adverse elevation

The LHP functioned successfully despite the adverse elevations. The effect of the degree of elevation on the heat transport ability and overall thermal resistance of the LHP is found by comparing the temperature profiles of the various sections of the LHP, as shown in Figures 5-15 to 5-17.

The heat load range over which operation is possible is a significant difference between the gravity-adverse and horizontal configurations. The larger the elevation, the smaller the range of heat loads which can be safely transferred. This is particularly evident for the 10° adverse elevation which can only support a maximum heat load of 27 W, less than half that of the horizontal operation. The 5° elevation LHP performs better but only up to 56 W.

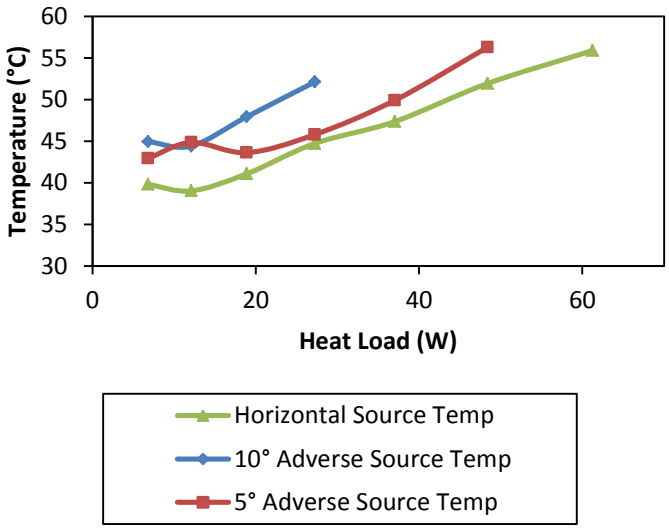

(a)

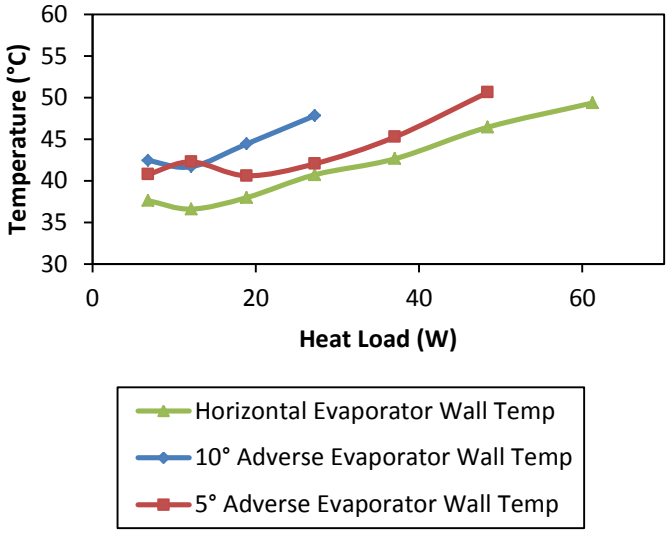

(b)

Fig.5-15. Temperature profiles of the horizontal, 5° and 10° gravity-adverse elevation of the LHP for the heat source (a) and evaporator wall (b)

For all elevations, the variable and constant conduction modes of operation are present and their transition point is around 12 W (Figure 5-15). It should be noted that there is an error in the readings for the 12 W load of the 5° elevation, probably due to the heat load being prematurely increased during testing before the temperatures could achieve their overshoot and decrease. These temperatures are expected to be much lower.

The operating temperatures during the variable conductance mode increase with elevation. This is expected as the increased pressure head required to overcome gravity produces a larger temperature difference between vapour in the evaporator and saturated fluid in the CC, according to the Clausius-Clapeyron relation. At low mass flow rates which leaves little subcooling in the CC inlet liquid, vapour temperatures increase with the elevation.

A temperature difference exists between each elevation during the constant conductance mode of operation, particularly between the horizontal and 10° elevation. For the 5° elevation this temperature difference is large for the variable conductance region but reduces as the LHP enters the constant conductance mode after 12 W. This is expected since the operating temperatures for any elevation converge as heat load increases. 10° elevation does not converge at all.

Figure 5-16 and Figure 5-17 confirm this behavior. The evaporator outlet and condenser inlet temperatures follow the same curves shown in Figure 5-15. The condenser outlet and CC inlet temperature profiles shown in Figure 15-17 show that these temperatures are similar for each elevation, with a maximum deviation of 1°C for the CC inlet.

The LHP was able to operate while adversely elevated. Due to the limited heat loads which could be safely applied to the LHP, the convergence of the operating temperatures during the constant conductance mode could not be conclusively reproduced. It can, however, be concluded that increasing elevation produced significantly larger operating temperatures, particularly during the variable conductance mode of operation, as expected.

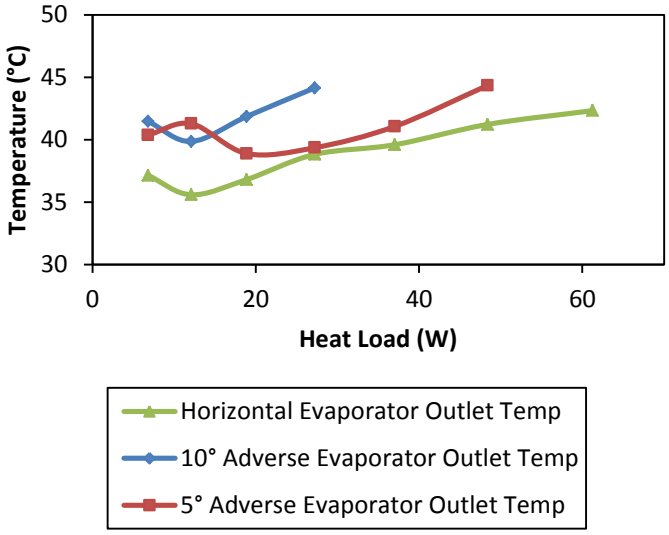

(a)

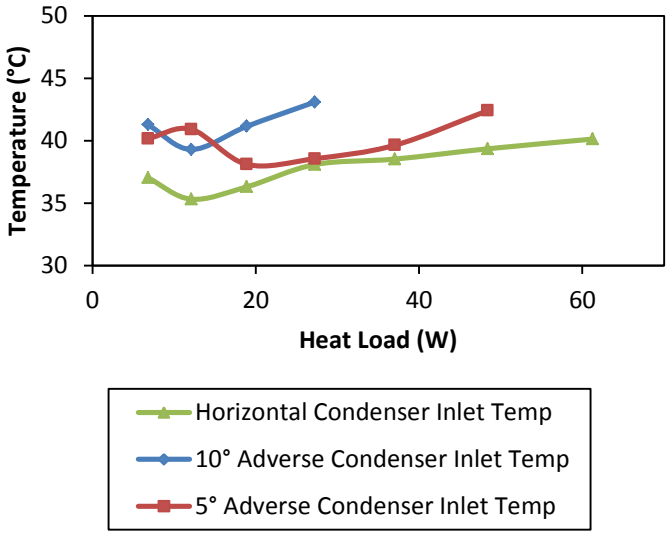

(b)

Fig.5-16. Temperature profiles of the horizontal, 5° and 10° gravity-adverse elevation of the LHP for the evaporator outlet (a) and condenser inlet (b)

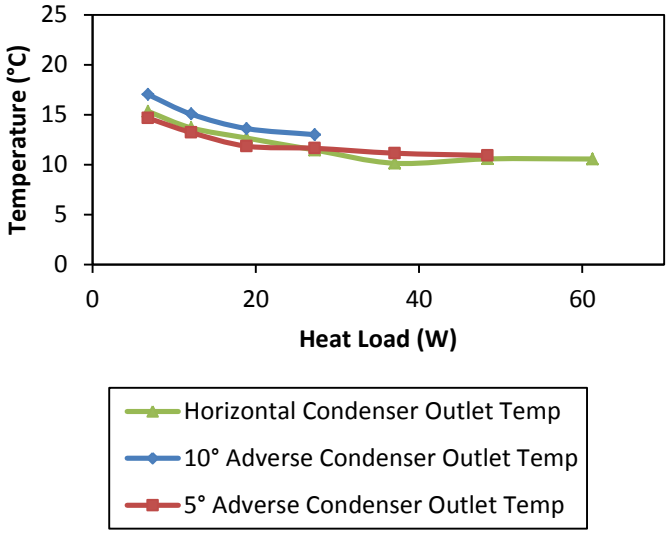

(a)

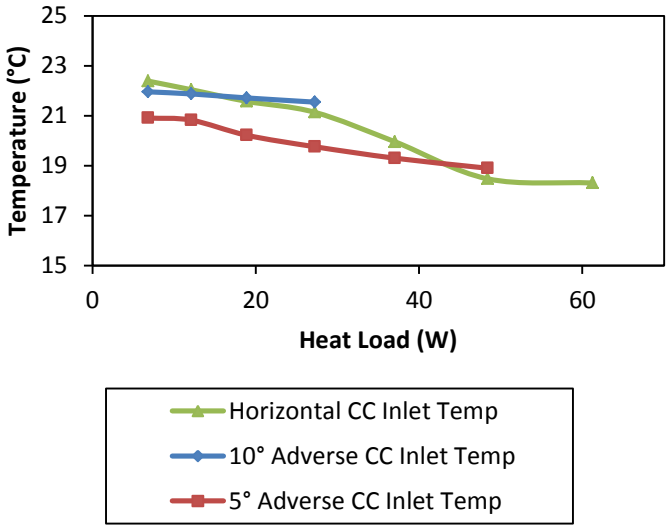

(b)

Fig.5-17. Temperature profiles of the horizontal, 5° and 10° gravity-adverse elevation of the LHP for the condenser outlet (a) and CC inlet (b)

5.6.2. Gravity-assisted operation

The temperature profiles of the 5° and 10° gravity-assisted operation of the standard LHP are shown in Figure 5-18 and Fig. 5-19.

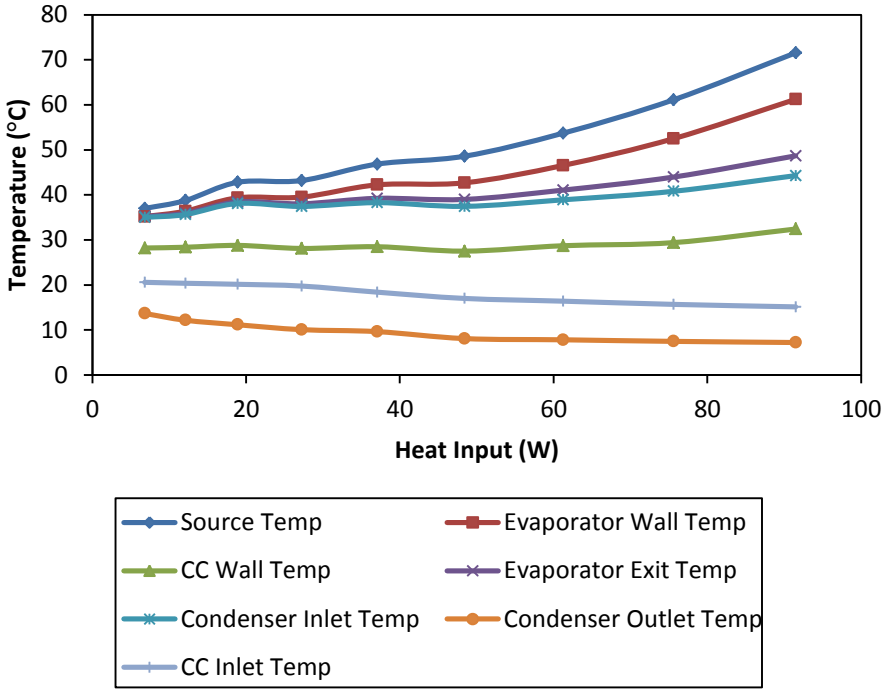

Fig.5-18. Temperature profile of 5° gravity-assisted elevation

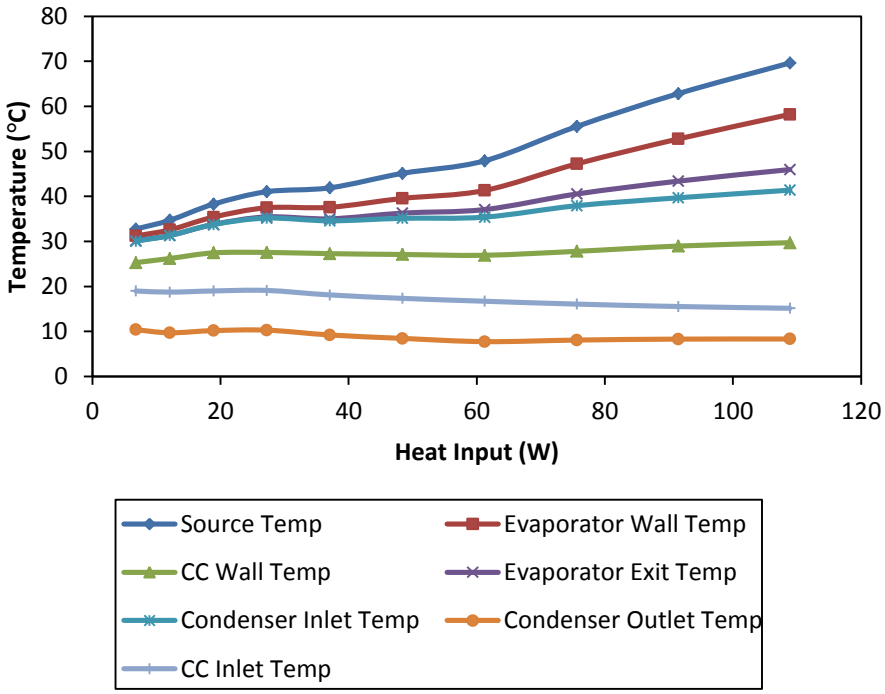

Fig.5-19. Temperature profile of 10° gravity-assisted elevation

As with the gravity-adverse operation, gravity-assisted operation is notable for the temperature difference between each elevation and for the range of heat loads at which the LHP can safely operate. With respect to the latter, increasing the elevation, even by 5°, was shown to increase

the safe heat load range from 61 W to 91 W. Increasing the elevation further to 10° increased the heat load range to 108 W. This is of interest as electronics heat management systems regularly demand heat load transferences of about 100 W while the heat source remained below 80°C. The LHP developed here, which can only transfer up to 61 W at horizontal, could be adapted into such a system as long as the condenser was positioned only a few millimetres above the evaporator.

Analysis of the temperature profiles was performed by comparing the temperature curves of each component separately. Figures 5-20 to 5-22 show these temperature curves.

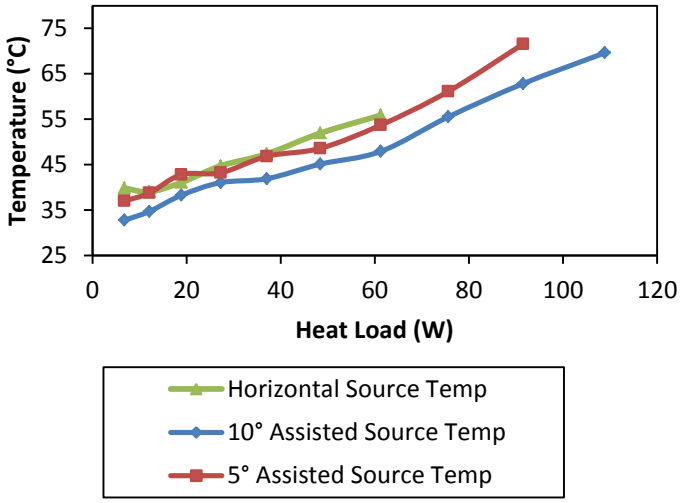

(a)

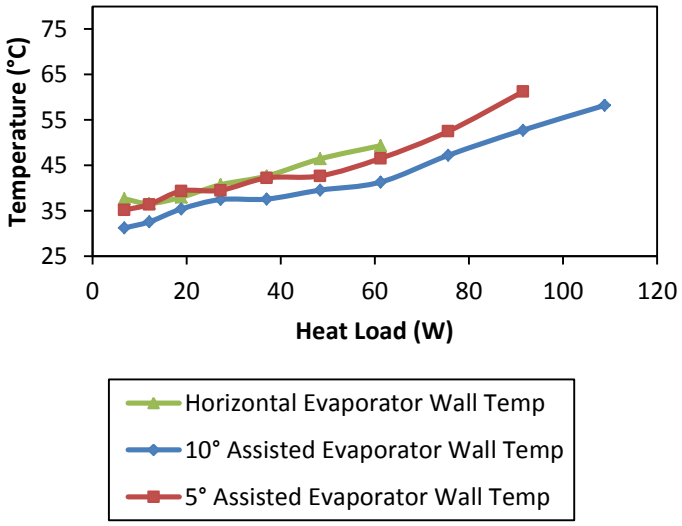

(b)

Fig.5-20. Temperature profiles of the horizontal, 5° and 10° gravity-assisted elevation of the LHP for the heat source (a) and evaporator wall (b)

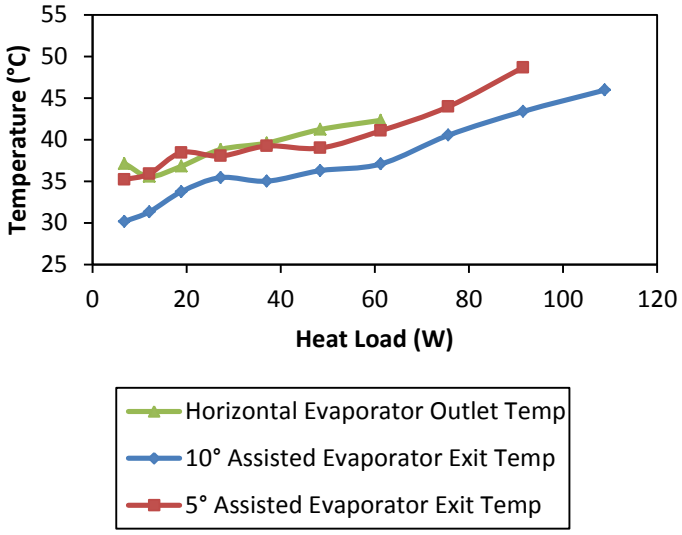

(a)

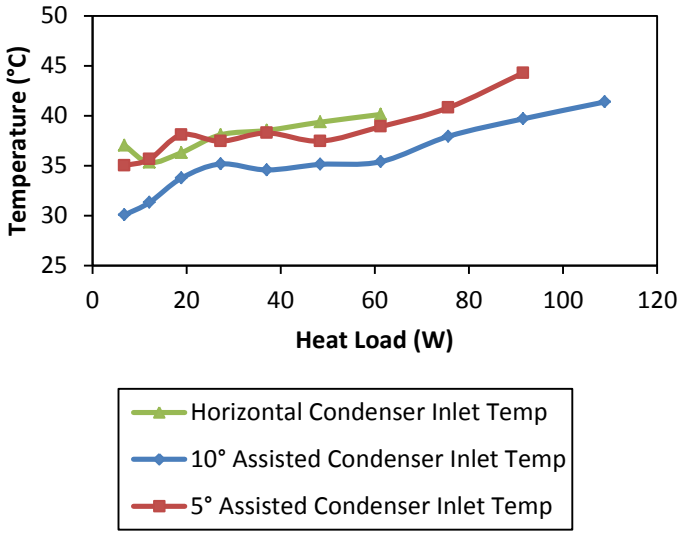

(b)

Fig.5-21. Temperature profiles of the horizontal, 5° and 10° gravity-assisted elevation of the LHP for the evaporator outlet (a) and condenser inlet (b)

A prominent feature of the gravity-assisted operation is the change in operating temperatures during the variable conductance mode of operation compared to the horizontal and gravity-adverse operations. As seen in Figures 5-18 to 5-21, the temperature curves for the heat source, evaporator wall, evaporator outlet and condenser inlet begin low and increase steadily with increasing heat load. This is because gravity dominates the operation at low heat loads before giving way to viscous forces as the mass flow increases with heat load. Unlike the adverse operation, where gravity must be overcome by creating a larger temperature difference across the wick, the flow is now assisted. A small temperature difference is required to maintain circulation, reducing the operating temperatures. The operating temperatures of the 10°

elevation are much lower than those of the horizontal and 5° elevation because the increased force of gravity reduces the temperature difference further.

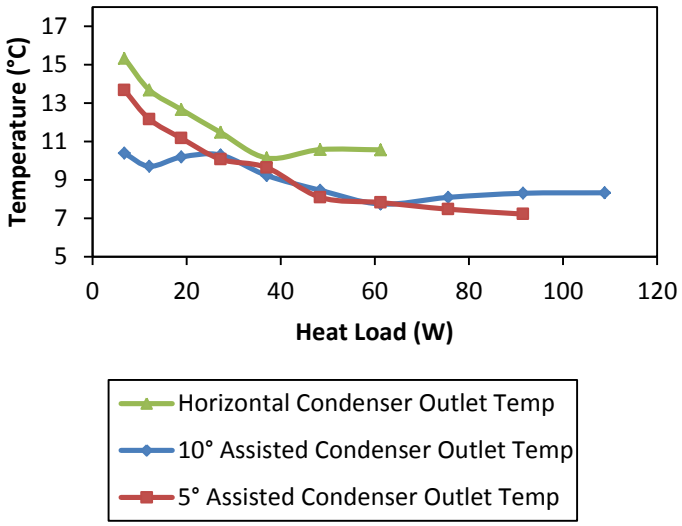

(a)

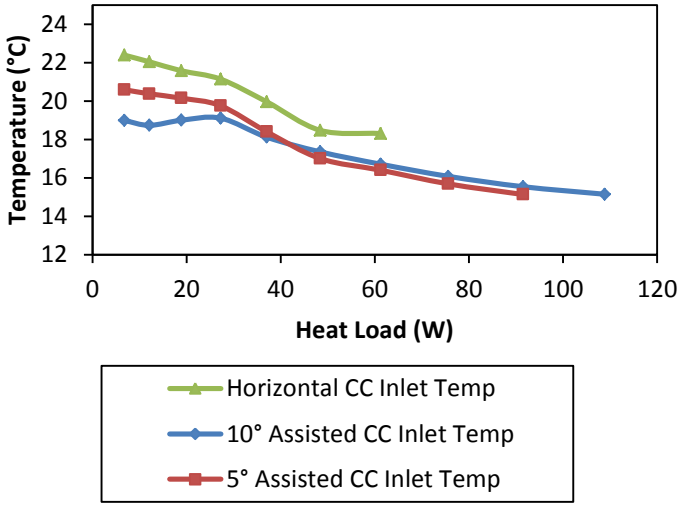

(b)

Fig.5-22. Temperature profiles of the horizontal, 5° and 10° gravity-assisted elevation of the LHP for the condenser outlet (a) and CC inlet (b)

The constant conductance mode of operation also shows a decrease in operating temperature with increasing gravity-assisted elevations. The effects of gravity on the LHP are expected to give way to increased viscous action at high heat loads and the temperature curves should converge. The curves do not, however, due to the increased subcooling of the fluid. As Figure 5-22 shows, the liquid in the liquid line, under the influence of gravity, retains a great deal of its subcooling and the temperatures at the CC inlet are very low compared to other operating

conditions. The degree of subcooling also increases with increasing heat loads, due to lower vapour temperatures. This not only lowers the operating temperatures of the 10° elevation, but also increases its heat load range.

The gravity-assisted operation of the LHP was a significant success. With a slight elevation of the condenser over the evaporator, the LHP was able to improve its performance considerably. This is due to the beneficial influence of gravity during both the variable and constant conductance modes, which reduces the temperature difference needed across the wick by simultaneously reducing the pressure difference required to maintain circulation and increasing the amount of subcooling entering the CC through the liquid line.

6. CONCLUSIONS

This study developed a steady-state, one-dimensional mathematical model and an experimental prototype of a loop heat pipe. The model was designed such that it required fewer empirical inputs than similar models and incorporated a void fraction correlation in the modeling of the condenser. The model was also constructed to be a generic LHP design tool through the use of the assumptions which relieved it of empirically determined values.

The porous wick, which is the primary component of the LHP, was successfully sintered and machined. It was established that the best temperature at which to sinter the wicks was 550°C to produce the highest porosity and permeability, with a two and half hour lead up time and a 10 minute dwell time. The resultant porosity is approximately 60% and the permeability is 6.77×10^{-13} m^2. Statistical analysis of SEM images of the wicks allowed the average pore radius to be determined but no correlation was found relating to the sintering temperature. All pore radii fell between 0.64 μm and 0.56 μm. To introduce a safety factor into the maximum capillary head, a much larger pore radius of 1 μm was assumed. The analysis of the vapour grooves and inner core showed that machining may in fact improve the quality of the surface.

A standard LHP was constructed, tested and shown to function in a manner consistent with other such devices described in the literature, albeit with a limited heat load range of 61 W and with larger operating temperatures than expected. The LHP has an acceptable thermal resistance of 0.7 W/K at 61 W and can potentially be used in a terrestrial heat management system. Performance of the experimental LHP was simulated using the mathematical model. Even though the model performed poorly during the variable conductance mode due to the lack of adequate two-phase heat leak modeling, it produced good agreement when the LHP operated in its constant conductance mode. The model was amended with data from the physical setup and required a tolerance on the mass charge of 1%. As a design tool, the assumptions made in the development of the model to reduce the need for empirical data in the evaporator were shown to be feasible. Neglecting superheat, maintaining a constant evaporator thermal conductance and varying the temperature of the CC wall to create a band of possible operating temperatures allows for acceptable simulated results. However, the experiment-based amendments made to the modeling of the condenser, liquid line and saddle meant that the model could not be used as a generic design tool in its present form.

The performance of the LHP was characterised under a number of experimental variations. Transport line variation showed that the heat load range decreases and operating temperatures increase as the transport line lengths are extended, and that the operating temperatures increase faster once the LHP enters into the constant conductance mode. The standard LHP is able to

operate under 5° and 10° gravity-adverse elevations but the acceptable heat load range decreases to 56 W and 27 W respectively and the operating temperatures are much higher. Finally, gravity-assisted elevations of 5° and 10° are shown to greatly improve the performance of the LHP, extending its heat load range up to 108 W at an elevation of 10° and lowering its operating temperatures significantly due to the influence of gravity. The gravity-assisted operation showed that the LHP can feasibly be employed in high-heat flux thermal management of electronics which typically require 100 W to be dissipated.

REFERENCES

[1] KU, J., 1999, Operating Characteristics of Loop Heat Pipes, *Proceeding of the 29th International Conference on Environmental System,* Denver, Colorado, USA, 12-15 July 1999, NASA Goddard Space Flight Center

[2] MAYDANIK, Y.F., 2005, Loop heat pipes, *Applied Thermal Engineering*, 25: 635–657

[3] AMBIRAJAN, A., ADONI, A.A., VAIDYA, J.S., RAJENDRAN, A.A., KUMAR, D., DUTTA, P., 2012, Loop Heat Pipes: A Review of Fundamentals, Operation and Design, *Heat Transfer Engineering,* 33 (4-5): 387-405

[4] ANDERSON, W.G., DUSSINGER, P.M., GARNER, S.D., HARTENSTINE, J.R., SARRAF, D.B., 2009, Loop Heat Pipe Design, Manufacture and Testing – An Industrial Perspective, *Proceedings of the ASME 2009 Heat Transfer Summer Conference,* San Francisco, California, USA, 19-23 July 2009

[5] DUSSINGER, P.M., SARRAF, D.B., ANDERSON, W.G., 2009, Loop Heat Pipe for TacSat-4, *Space, Propulsion and Energy Sciences International Forum, AIP Conference Proceedings,* 1103: 91-100

[6] LAUNAY, S., SARTRE, V., BONJOUR, J., 2007, Parametric analysis of loop heat pipe operation: a literature review, *International Journal of Thermal Sciences*, 46: 621–636

[7] GILMORE, D.G., (ed), 2002, *Spacecraft Thermal Control Handbook: Volume 1: Fundamental Technologies*, El Segundo, California: The Aerospace Press

[8] RIEHL, R.R., 2006, Extensive Development of the Loop Heat Pipe Technology, *Proceedings of International Conference on Environmental Systems,* Norfolk, Virginia, USA, 17 July 2006

[9] ZHANG, H.X., LIN, G.P., DING, T., YAO, W., SHAO, X.G., SUDAKOV, R.G., MAYDANIK, Y.F., 2005, Investigation of Startup Behaviors of a Loop Heat Pipe, *Journal of Thermophysics and Heat Transfer,* 19 (4): 509-518

[10] HARTENSTINE, J.R., ANDERSON, W.G., BONNER III, R., 2008, Titanium Loop Heat Pipes for Space Nuclear Power Systems, *Space, Propulsion and Energy Sciences International Forum, AIP Conference Proceedings,* 969: 44-52

[11] PASTUKHOV, V.G., MAYDANIK, Y.F., 2007, Low-noise cooling system for PC on the base of loop heat pipes, *Applied Thermal Engineering,* 27: 894-901

[12] PASTUKHOV, V.G., MAYDANIK, Y.F., VERSHININ, C.V., KORUKOV, M.A., 2003, Miniature loop heat pipes for electronic cooling, *Applied Thermal Engineering,* 23: 1125-1135

[13] MAYDANIK, Y.F., VERSHININ, S.V., 2009, Development and tests of ammonia Miniature Loop Heat Pipes with cylindrical evaporators, *Applied Thermal Engineering,* 29: 2297-2301

[14] CHEN, Y., GROLL, M., MERTZ, R., MAYDANIK, Y.F., VERSHININ, S.V., 2006, Steady-state and transient performance of a miniature loop heat pipe, *International Journal of Thermal Sciences,* 45: 1084-1090

[15] MAYDANIK, Y.F., VERSHININ, S.V., PASTUKHOV, V.G., FRIED, S., 2010, Loop Heat Pipes for Cooling Systems of Servers, *IEEE Transactions on Components and Packaging Technologies,* 33 (2): 416-423

[16] SINGH, R., AKBARZADEH, A., MOCHIZUKI, M., 2008, Operational characteristics of a miniature loop heat pipe with flat evaporator, *International Journal of Thermal Sciences,* 47: 1504-1515

[17] TANG, Y., XIANG, J., WAN, Z., ZHOU, W., WU, L., 2010, A Novel Miniaturized Loop Heat Pipe, *Applied Thermal Engineering,* 30 (10): 1152-1158

[18] KOBAYASHI, Y., OGUSHI, T., HAGA, S., OZAKI, E., FUJII, M., 2003, Heat Transfer Performance of a Flexible Looped Heat Pipe Using R134a as a Working Fluid: Proposal for a Method to Predict the Maximum Heat Transfer Rate of FLHP, *Heat Transfer-Asian Research,* 32 (4): 306-318

[19] VASILIEV, L., LOSSOUARN, D., ROMESTANT, C., ALEXANDRE, A., BERTIN, Y., PAITSIUSHYK, Y, ROMANENKOV, V., 2009, Loop heat pipe for cooling of high-power electronic components, *International Journal of Heat and Mass Transfer,* 52: 301-308

[20] LU, X.Y., HUA, T.C., LIU, M.J., CHENG, Y.X., 2009, Thermal analysis of loop heat pipe used for high-power LED, *Thermochimica Acta,* 493: 25-29

[21] KAYA, T., HOANG, T.T., KU, J., CHEUNG, M.K., 1999, Mathematical Modeling of Loop Heat Pipes, *Proceedings of 37th Aerospace Sciences Meeting and Exhibit*, Reno, USA, January 1999

[22] CAREY, V.P., 1992, *Liquid-Vapor Phase Change Phenomena: An Introduction to the Thermophysics of Vaporization and Condensation Processes in Heat Transfer Equipment,* USA, Hemisphere Publishing

[23] BAI, L., LIN, G., ZHANG H., WEN D., 2009, Mathematical modeling of steady-state operation of a loop heat pipe, *Applied Thermal Engineering*, 29: 2643–2654

[24] BAI, L., LIN, G., WEN, D., 2010, Modeling and analysis of startup of a loop heat pipe, *Applied Thermal Engineering*, 30: 2778-2787

[25] VLASSOV, V.V., RIEHL, R.R., 2008, Mathematical model of a loop heat pipe with cylindrical evaporator and integrated reservoir, *Applied Thermal Engineering,* 28: 942-954

[26] CHERNYSHEVA, M.A., MAYDANIK, Y.F., 2008, Numerical simulation of transient heat and mass transfer in a cylindrical evaporator of a loop heat pipe, *International Journal of Heat and Mass Transfer,* 51: 4204-4215

[27] KAYA, T., GOLDAK, J., 2006, Numerical analysis of heat and mass transfer in the capillary structure of a loop heat pipe, *International Journal of Heat and Mass Transfer,* 49: 3211-3220

[28] CULLIMORE, B., BAUMANN, J., 2000, Steady-state and Transient Loop Heat Pipe Modeling, *Proceedings of International Conference on Environmental Systems,* Toulouse, France, 10 July 2000

[29] XIN, G., CUI, K., ZOU, Y., CHENG, L., 2009, Development of sintered Ni-Cu wicks for loop heat pipes, *Science in China Series E: Technological Sciences*, 52 (6): 1607-1612

[30] SAMANTA, S. K., DAS, P., LOHAR, A. K., 2011, Development of Tubular Ni Wick used in LHP for Space Applications, *Proceedings of 10th International Heat Pipe Symposium*, Taipei, Taiwan, 6-9 November 2011

[31] REIMBRECHT, E. G., FREDEL, M.C., BAZZO, E., PEREIRA, F.M., 1999, Manufacturing and Microstructural Characterization of Sintered Nickel Wicks for Capillary Pumps, *Materials Research*, 2(3): 225-229

[32] YEH, C.C., LUI, B. H., CHEN, Y. M., 2008, A study of loop heat pipe with biporous wicks, *Heat Mass Transfer*, 44: 1537-1547

[33] ZAN, K.J., ZAN, C.J., CHEN, Y.M., WU, S.J., 2004, Analysis of the Parameters of the Sintered Loop Heat Pipe, *Heat Transfer-Asian Research,* 33 (8): 515-526

[34] CHU, C.I., WU, S.C., CHEN, P.L., CHEN, Y.M., 2004, Design of a Miniature Loop Heat Pipe, *Heat Transfer-Asian Research,* 33 (1): 42-52

[35] WU, S., HUANG, C. YANG, W., CHANG, J., KUNG, C., 2012, Effects of Sintering Temperature Curve in Wick Manufacturing for Loop Heat Pipe, *World Academy of Science, Engineering and Technology,* 62: 631-636

[36] HAMDAN, M., ELNAJJAR, E., 2009, Loop Heat Pipes: Simple Thermodynamic, *World Academy of Science, Engineering and Technology,* 52: 161-167

[37] SHUKLA, K.N., 2008, Thermo-fluid dynamics of Loop Heat Pipe operation, *International Communications in Heat and Mass Transfer,* 35: 916-920

[38] WALLIS, G. B., 1965, *One-Dimensional Two-Phase Flow,* New York, Wiley

[39] BOO, J.H., CHUNG, W.B., 2005, Experimental Study on the Thermal Performance of a Small-scale Loop Heat Pipe with Polypropylene Wick, *Journal of Mechanical Science and Technology*, 19 (4): 1052-1062

[40] SAMANTA, S. K., DAS, P., LOHAR, A. K., KUMAR, S., CHATTOPADHYAY, D.P., CHOWDHURY, A. K., 2011, Manufacturing of Nickel wick for loop heat pipe through MIM route, *PowderMet*, San Francisco, USA

[41] JONES, W.D., 1960, *Fundamental Principles of Powder Metallurgy*, London, Edward Arnold, 399-420

[42] Omega Engineering, *Revised Thermocouple Reference Tables Type-T.* [online] Available at: http://www.omega.com/temperature/z/pdf/z207.pdf [Accessed February 2013]

[43] National Instruments Technical Sales, 2010, *4-Channel, 14 S/s, 24-Bit, ±80 mV C Series Thermocouple Input Module NI 9211.* [online] Available at: http://sine.ni.com/ds/app/doc/p/id/ds-197/lang/en [Accessed February 2013]

[44] National Institute of Standards and Technology, 2011, *Thermophysical Properties of Fluid Systems.* [online] Available at: http://webbook.nist.gov/chemistry/fluid/ [Accessed April 2010]

[45] Colorado State University, 2008, *Ammonia Best Management Practices for Livestock Operations* [online] Available at: http://ammoniabmp.colostate.edu/link%20pages/impacts%20of%20ammonia.html [Accessed October 2012]